



POLITECNICO
MILANO 1863

School of Industrial and Information Engineering

Master of Science in Mechanical Engineering

**Effect of Tension Load and Laser Power on Functional
Properties of Thin Nitinol Wires during Straight Laser
Shape Setting**

Supervisor: Prof. Carlo Alberto BIFFI

Co-supervisor: Dr. Ausonio TUISSI

Master of Science Thesis of:
Lucrezia LIGARI
ID. 816017

Academic Year 2015 – 2016

Acknowledgements

First of all, I would like to thank my supervisor, Eng. Carlo Alberto BIFFI, which allows me to undertake this interesting thesis work, providing me with directions and advices during all this year. He was able to expertly and patiently guide me in all the activities, leaving me the possibility to extend my knowledge and grow my practical skills.

I am also thankful to my co-supervisor Dr. Ausonio TUISSI, for his constant assistance and encouragement.

I would like to express my sincere gratitude to all the members of the CNR IENI of Lecco, in particular Enrico BASSANI, Paola BASSANI, Giordano CARCANO, Marco PINI and Elena VILLA for their precious technical support. You made my thesis work possible and made the laboratory a really pleasure place to stay.

Furthermore, I would like to thank my thesis mates, Matteo and Stefano, and Riccardo; we spent together the happiest moments and share the worst moments of this challenging experience, always helping and motivating each other.

My most heartfelt gratefulness goes to my family, whom priceless support was a constant for all my life and university career.

Table of Contents

Acknowledgements	I
List of Figures	V
List of Tables	XIII
Abstract	XIV
Sommario	XV
Introduction	XVI
1 State of art: Shape memory alloys	1
1.1 Crystallography of martensitic transformation	1
1.2 Thermodynamic aspects of martensitic transformation	5
1.2.1 Thermally-induced martensitic transformation (TIM)	7
1.2.2 Stress-induced martensitic transformation (SIM)	9
1.3 Functional properties of SMAs	10
1.3.1 One way shape memory effect (OWSME)	10
1.3.2 Two way shape memory effect (TWSME)	12
1.3.3 Superelasticity	14
1.4 Nitinol	16
1.4.1 General properties	17
1.4.2 Influence of grain size	19
1.4.3 Influence of chemical composition	20
1.5 Applications	23
1.5.1 Medical applications	24
1.5.2 Engineering applications	29
1.5.3 Other applications	36
2 Heat treatment of SMAs	38
2.1 Conventional annealing	38
2.1.1 Cold work and annealing	38
2.1.2 Shape setting	43
2.1.3 Cycling	44

2.2 Unconventional annealing.....	47
2.2.1 Laser annealing.....	47
2.2.2 Electropulse treatment (EPT).....	53
2.2.3 Electroplastic deformation (EPD).....	56
3 Aims of the work.....	59
4 Definition of materials, equipment and processes	61
4.1 Materials.....	61
4.1.1 As drawn wire	62
4.1.2 Straight annealed wire.....	63
4.2 Conventional heat treatment	66
4.3 Unconventional heat treatment.....	68
4.3.1 Laser system	68
4.3.2 Calibration of the load cell.....	75
4.3.3 Laser shape setting.....	80
4.4 Methods of characterization.....	84
4.4.1 Calorimetric analysis.....	84
4.4.2 Mechanical analysis	88
4.4.3 Metallographic analysis.....	91
5 Analysis of results and discussion: furnace annealing	94
5.1 Calorimetric analysis.....	94
5.2 Mechanical analysis	104
5.3 Mechanical cycling	109
5.4 Metallographic analysis.....	113
6 Analysis of results and discussion: laser shape setting.....	121
6.1 Calorimetric analysis.....	122
6.2 Mechanical analysis	130
6.3 Mechanical cycling	134
6.4 Metallographic analysis.....	138
7 Conclusions	142
Bibliography	145

Appendix A	151
Appendix B	152
Appendix C.....	153
Appendix D	156
Appendix E.....	158
Appendix F.....	163

List of Figures

Figure 0.1 Nitinol medical devices examples: stent (a), blood filtering device (b) [Duerig, 1999], surgical instrument (c) [Stöckel, 2000] and orthodontic archwire (d) [Petrini, 2011].	XVII
Figure 1.1 Schematic representation of the transformation from austenite (a) to martensite (b) in two dimensions [Wayman, 1990].	2
Figure 1.2 Schematic representation of the two mechanisms of accommodating the shape change due to the atomic shear of a martensitic transformation: slip (a) and twinning (b) [Wayman, 1990].	3
Figure 1.3 Schematic view of a twin boundary [Wayman, 1990].	4
Figure 1.4 Schematic depiction of the lattice structures of austenite and martensite in NiTiInol [Maletta, 2012].	4
Figure 1.5 Hypothetical plot of property change vs. temperature for a martensitic transformation occurring in a shape memory alloy. The parent phase (austenite) is represented by the square lattice, which upon martensitic transformation is distorted into the rhombi [Wayman, 1990].	6
Figure 1.6 Typical stress-strain curve for a twinned martensitic material shows two distinct elastic regions and two distinct plasticity plateaus, due respectively to twin motion and slip [Wayman, 1990].	6
Figure 1.7 Differential scanning calorimetry thermogram of a NiTi alloy [Maletta, 2012].	7
Figure 1.8 Thermal hysteresis of a NiTi alloy describing the evolution of volume fraction of martensite [Maletta, 2012].	8
Figure 1.9 Stress-strain curve of an austenitic NiTi alloy with characteristic transformation stresses [Maletta, 2012].	9
Figure 1.10 Two dimensional scheme of shape memory process: austenite (a) is cooled to form twinned martensite (b) without undergoing a shape change, then it is deformed by moving twin boundaries (c) [Wayman, 1990].	10
Figure 1.11 Schematic depiction of phase transition mechanism (a) and stress-strain-temperature response (b) [Maletta, 2012].	11
Figure 1.12 Schematic depiction of the two-way shape memory effect: phase transition mechanisms (a) and strain-temperature hysteretic response (b) [Maletta, 2012].	13
Figure 1.13 Comparison of the one-way (upper) and two-way (lower) shape memory effects using a coil spring as an example [Wayman, 1990].	14
Figure 1.14 Schematic depiction of the pseudo elastic effect: stress-induced phase transition mechanisms (a) and stress-strain hysteretic response (b) [Maletta, 2012].	15

Figure 1.15 Evolution of the stress-strain response of a commercial pseudoelastic NiTi alloy during the first 25 mechanical cycles for a maximum applied deformation of 3.5% [Maletta, 2009].	16
Figure 1.16 The stress-strain curves of several natural biological materials are superimposed on Nitinol stress-strain curve [Duerig, 1999].	18
Figure 1.17 Ni-Ti phase diagram [Bram, 2002].	19
Figure 1.18 Grain size dependence of pseudoelasticity in Ti-50.5 at % Ni alloy [Otsuka, 1999].	20
Figure 1.19 Equilibrium phase diagram for Ti-Ni in the vicinity of TiNi [Bastin, 1974].	20
Figure 1.20 Dependence of the transformation temperature M_s on composition [Melton, 1990].	22
Figure 1.21 Enthalpy changes of forward and reverse martensitic transformation as a function of Ni atomic content in binary NiTi alloys [Khalil-Allafia, 2009].	22
Figure 1.22 Schematic of the effect of the Ni content of Nitinol on the alloy phase transformation temperature A_f . The shaded region represents the area covered by typical binary superelastic Nitinol alloys [Russell, 2000].	23
Figure 1.23 Model of stent laser cut from nitinol tubing [Morgan, 2004].	25
Figure 1.24 Simon vena cava filter (a) and device to close ventricular septal defects [Petrini, 2011].	26
Figure 1.25 Innovative endoscopic instruments that use nitinol rods to actuate tools (a) and nitinol tubing with an internal actuation wire that allows it to operate while tied in a knot (b) [Duerig, 1999].	27
Figure 1.26 Palatal arch (a) and orthodontic distracters (b) [Petrini, 2011].	28
Figure 1.27 NiTi plate for mandible fracture (a) and spinal vertebrae spacer (b) [Petrini, 2011].	28
Figure 1.28 (a) Scheme of a coupling, machined and expanded (top), after free recovery (middle) and installed on a tube (bottom) [Stockel, 2000]. (b) Aircraft hydraulic couplings [Duerig, 1989].	29
Figure 1.29 Application of shape-memory alloys to a thermostatic mixing valve: structure (a) and example of a commercially available valve (b) [Otsuka, 2002].	30
Figure 1.30 SMA robotic arm which resembles a human hand and can grasp a very delicate ball without damage (a) and basic scheme for the SMA undersea robot resembles a crab, with six legs, each with two joints (b) [Furuya, 1991].	32
Figure 1.31 Shape memory alloy adjustable camber (SMAAC) control surface internal actuator concept [Beauchamps, 1992].	33

Figure 1.32 Adaptive serrated nozzle (ASN) for Quiet Technology Demonstrator 2 project developed by Boeing, NASA, General Electric and Goodrich Corporation [Herkes, 2006].....	34
Figure 1.33 Schematic of the SMA isolation device for elevated highway bridges (a) and of the SMA isolation system for buildings (b) [Song, 2006].	35
Figure 1.34 Schematic of the setup of the SMA brace reinforced frame structure (a) of a SMA damper for a stay-cable bridge (b) and of SMA connector for steel structures (c) [Song, 2006].....	35
Figure 1.35 Superelastic Nitinol eyeglass frame [materialdesign.it].	36
Figure 1.36 Shape transforming lamp shade designed by Oki Sato [Brownell, 2008].	37
Figure 2.1 DSC cooling and heating curves of NiTi specimens showing the R-phase development and the variation of transformation temperatures for various levels of cold work and heat treatment during the austenitic to martensitic phase transformation [Miller, 2001].	39
Figure 2.2 Effect of (a) annealing temperature and (b) cold work on latent heat of transformation for NiTi specimens [Miller, 2001].	40
Figure 2.3 DSC curves for the material treated at different temperatures and in the cold worked condition (as-received) [Huang, 2001].	41
Figure 2.4 Transformation temperatures of the alloy as a function of the annealing temperature [Huang, 2001].	41
Figure 2.5 Load-deflection curves for the material treated at different temperatures and in the cold worked condition (control) [Myara, 2014].	42
Figure 2.6 A pin and plate shape-setting holding fixture (a) and a cylindrical mandrel to create helical springs (b) [Smith, 2014].	43
Figure 2.7 Transformation temperatures plotted against number of thermal cycles (a) and change in internal structure due to thermal cycling, where N indicates the number of thermal cycles (b) [Miyazaki, 1986].	45
Figure 2.8 Permanent strain as a function of the number of thermal cycles at different tensile stresses: 135, 270, 405 and 540 MPa [Zimmermann, 1997].	46
Figure 2.9 Influence of repeated thermal cycling with applied 200 MPa [Stachowiak, 1988].	46
Figure 2.10 Effect of cyclic deformation on stress-strain curves of a Ni-Ti alloy thermos-mechanically treated [Otsuka, 1999].	47
Figure 2.11 Crystallization behavior of NiTi films as a function of laser power density and scan speed based on optical (not shown) and TEM observations [Wang, 2005].	48
Figure 2.12 Temperature distribution, hardness profile and microstructural gradient through the thickness of laser annealed thin NiTi plate [Meng, 2012].	49

Figure 2.13 Schematic of the laser shape setting process on NiTi SMA wire [Biffi, 2016].	51
Figure 2.14 Thermo-mechanical response of the wires: straight annealed and laser shape setted [Biffi, 2014].	52
Figure 2.15 Stress-strain curves of SE NiTi wires at 25 °C: laser shape setting (a) commercial straight annealing (b) [Biffi, 2016].	52
Figure 2.16 (a) Thermomechanical recovery of each microgripper component and (b) the combined recovery of the laser-processed NiTi microgripper [Daly, 2012].	53
Figure 2.17 (a) Experimental set-up presentation. (b) Resulting material with local heat treatment [Delobelle, 2016].	54
Figure 2.18 (a) Elastic moduli in function of pulse duration. (b) Plateau stresses at loading, unloading and hysteresis in function of pulse duration [Delobelle, 2016].	55
Figure 2.19 Schema of the equipment used for the treatment of continuous thin NiTi filaments [Pilch, 2010].	56
Figure 2.20 Schematic view of electroplastic rolling process [Zhu, 2013].	57
Figure 2.21 Superelastic properties of TiNi strips: (a) EPRed, (b) annealed at 400 °C for 30 min, (c) annealed at 500 °C for 30 min and (d) annealed at 500 °C for 60 min [Zhu, 2013].	58
Figure 4.1 Commercially available wire spools from SAES Getters Group.	61
Figure 4.2 DSC curve of the 100 μm (a) and 200 μm (b) as drawn wire.	62
Figure 4.3 Stress-strain curve of the 100 μm (a) and 200 μm (b) as drawn wire.	63
Figure 4.4 DSC curve of the 100 μm (a) and 200 μm (b) straight annealed wire.	64
Figure 4.5 Stress-strain curve of the 100 μm (a) and 200 μm (b) straight annealed wire.	66
Figure 4.6 Muffle furnace used for the conventional heat treatment.	67
Figure 4.7 Laser source IPG Photonics YLR-300/3000-QCW-MM-AC-Y12.	69
Figure 4.8 Laser head model Fiber Mini from Laser Mech.	69
Figure 4.9 Caustic of the laser beam beyond the focalization lens; the depth of field is highlighted in orange.	70
Figure 4.10 Trend of the irradiance of the laser beam as a function of the distance from the focal position.	70
Figure 4.11 2D motion stage used for the control of the sample holder (Aerotech - PR0165LM).	72
Figure 4.12 Complete view of the sample holder mounted on the motion stage (a) and detail of the structure containing the load cell (b).	72
Figure 4.13 Load cell 8416-5020 (a) and amplifier 9235 (b).	73
Figure 4.14 View of the complete laser system utilized in this work.	75
Figure 4.15 System used for the calibration of the load cell.	76

Figure 4.16 Voltmeter and amplifier used for the cell calibration.....	77
Figure 4.17 Load cell with a test mass applied (a) and detail of the contact between screw tip and load cell (b).	78
Figure 4.18 Calibration curve of the load cell.....	79
Figure 4.19 Standard deviation calculated on the five calibration tests carried out on the load cell.	80
Figure 4.20 Detail of the sample holder with the Nitinol wire positioned and preloaded to perform the laser annealing	81
Figure 4.21 Schematic of the NiTi wire laser shape setting process: longitudinal (a) and transversal (b) view.....	82
Figure 4.22 Complete test matrix of the laser annealing campaign. The blue crosses represent the conditions investigated for the 100 μm diameter wire.	84
Figure 4.23 Scheme of the measuring chamber of the DSC (www.psrc.usm.edu).....	85
Figure 4.24 DSC curve for a generic Nitinol SMA, with visible phase transformations upon cooling and upon heating and corresponding characteristic temperatures and enthalpies indicated.....	86
Figure 4.25 DSC used in this work, model Q100 TA Instruments, (a) and detail of the measuring chamber (b).	87
Figure 4.26 General schematic of a DMA instrument. [en.wikipedia.org] ...	88
Figure 4.27 Typical stress-strain curve for a generic superelastic Nitinol SMA at room temperature.	89
Figure 4.28 DMA used in this work, model Q800 TA Instruments, (a) and detail of the clamps with the wire inserted (b).	90
Figure 4.29 Optical microscope utilized in this work (Leica, mod. Aristomet).	92
Figure 4.30 3D printed support for samples (a), section of a 100 μm wire seen by the light microscope (b) and lapping machine used for the sample preparation (c).....	93
Figure 5.1 Evolution of the calorimetric response of the 100 μm wire, starting from the cold worked condition (top) to the furnace annealed material, treated at 300, 400, 450, 500, 550, 600, 650, 700 and 800 $^{\circ}\text{C}$ (bottom).....	95
Figure 5.2 Evolution of the calorimetric response of the 200 μm wire, starting from the cold worked condition (top) to the furnace annealed material, treated at 300, 400, 450, 500, 550, 600, 650, 700 and 800 $^{\circ}\text{C}$ (bottom).....	96
Figure 5.3 Evolution of the peak width of the martensite and R-phase transformations upon cooling and austenite and R-phase transformations upon heating for the 100 μm wire as a function of the furnace annealing temperature.....	98

Figure 5.4 Martensite characteristic temperatures upon cooling: martensite start (left) and martensite finish (right). The straight lines are the corresponding characteristic temperatures for the straight annealed wires.	99
Figure 5.5 R-phase characteristic temperatures upon cooling: R-phase start (left) and R-phase finish (right). The straight lines are the corresponding characteristic temperatures for the straight annealed wires.	100
Figure 5.6 Austenite characteristic temperatures upon heating: austenite start (left) and austenite finish (right). The straight lines are the corresponding characteristic temperatures for the straight annealed wires.	100
Figure 5.7 R-phase characteristic temperatures upon heating: R-phase start (left) and R-phase finish (right). The straight lines are the corresponding characteristic temperatures for the straight annealed wires.	101
Figure 5.8 Comparison between the shapes of the martensitic transformation peak for the 600°C furnace annealed sample (a) and the 800°C furnace annealed sample (b).	102
Figure 5.9 Transformation enthalpies of R-phase and martensite upon cooling (left) and R-phase and austenite upon heating (right).	103
Figure 5.10 Comparison between DSC curves of the 100 μm 450 °C furnace annealed wire and the 100 μm straight annealed wire.	104
Figure 5.11 Evolution of the stress-strain response of the 100μm wire, starting from the cold worked condition (top) to the furnace annealed material, treated at 300, 400, 450, 500, 550, 600, 650, 700 and 800°C (bottom).	105
Figure 5.12 Evolution of the stress-strain response of the 200μm wire, starting from the cold worked condition (top) to the furnace annealed material, treated at 300, 400, 450, 500, 550, 600, 650, 700 and 800°C (bottom).	106
Figure 5.13 Length of the superelastic plateau upon loading phase (left) and residual strain after the first loading/unloading cycle (right). The straight lines correspond to the strains measured for the 100μm straight annealed wire (data for the 200μm wire are not available).	107
Figure 5.14 Stress value of the superelastic plateau upon loading phase (left) and mechanical hysteresis of the first loading/unloading cycle (right) measured at 3% strain. The straight lines correspond to the stresses measured for the 100μm straight annealed wire (data for the 200μm wire are not available).	108
Figure 5.15 Comparison between stress-strain curves of the 100 μm 450 °C furnace annealed wire and the 100 μm straight annealed wire.	108

Figure 5.16 Stress-strain curves acquired at cycle 1, 10, 20, 30, 40 and 50 for the wire treated at 400 (a), 450 (b), 550 (c) and 650°C (d) and for the SA wire (e) loaded up to 4% strain.....	111
Figure 5.17 Evolution of the mechanical hysteresis measured at 3 % strain as a function of the number of cycles for the furnace annealed wires. The dashed line represents the corresponding trend for the straight annealed wire.....	112
Figure 5.18 Evolution of the recoverable strain as a function of the number of cycles for the furnace annealed wires. The dashed line represents the corresponding trend for the straight annealed wire.....	112
Figure 5.19 Microstructural evolution for the 200 μm wire annealed in furnace at 400, 550, 650 and 800°C.....	114
Figure 5.20 Optical micrographs of 100 μm and 200 μm wires in the cold worked and straight annealed conditions.....	115
Figure 5.21 Optical micrographs of 100 μm and 200 μm wires annealed in furnace at 300 °C (a), 400 °C (b) and 450 °C (c).....	117
Figure 5.22 Optical micrographs of 100 μm and 200 μm wires annealed in furnace at 500 °C (a), 550 °C (b) and 600 °C (c).....	118
Figure 5.23 Optical micrographs of 100 μm and 200 μm wires annealed in furnace at 650 °C (a), 700 °C (b) and 800 °C (c).....	119
Figure 6.1 Evolution of the DSC response for the laser annealing with load 5 MPa (a) and 50 MPa (b), starting from the cold worked condition to the laser annealed material, treated with incident power 65 , 75 and 85 W....	123
Figure 6.2 Evolution of the DSC response for the laser annealing with load 150 MPa (a) and 300 MPa (b), starting from the cold worked condition to the laser annealed material, treated with incident power 65 , 75 and 85 W.	124
Figure 6.3 Martensite characteristic temperatures upon cooling: martensite start (left) and martensite finish (right). The dashed lines are the corresponding characteristic temperatures for the straight annealed wire.	126
Figure 6.4 R-phase characteristic temperatures upon cooling: R-phase start (left) and R-phase finish (right). The dashed lines are the corresponding characteristic temperatures for the straight annealed wire. The R-phase transformation is not present for the LA 85 W wire.	126
Figure 6.5 Austenite characteristic temperatures upon heating: austenite start (left) and austenite finish (right). The dashed lines are the corresponding characteristic temperatures for the straight annealed wire.	127
Figure 6.6 Evolution of the peak width of the martensite and R-phase transformations upon cooling and austenite transformation upon heating	

as a function of the laser annealing power for the annealing with minimum level of applied load (5 MPa).	128
Figure 6.7 Transformation enthalpies of R-phase and martensite upon cooling (left) and austenite upon heating (right) for the three levels of incident power analyzed.	128
Figure 6.8 Evolution of the stress-strain response for the laser annealing with load 5 MPa (a) and 50 MPa (b), starting from the cold worked condition to the laser annealed material, treated with incident power 65, 75 and 85 W.	131
Figure 6.9 Evolution of the stress-strain response for the laser annealing with load 150 MPa (a) and 300 MPa (b), starting from the cold worked condition to the laser annealed material, treated with incident power 65, 75 and 85 W.	132
Figure 6.10 Length of the superelastic plateau upon loading phase (left) and residual strain after the first loading/unloading cycle (right). The dashed lines correspond to the strains measured for the 100 μm straight annealed wire.	133
Figure 6.11 Stress value of the superelastic plateau upon loading phase (left) and mechanical hysteresis of the first loading/unloading cycle (right) measured at 3% strain. The dashed lines correspond to the stresses measured for the straight annealed wire.	134
Figure 6.12 Stress-strain curves acquired at cycle 1, 10, 20, 30, 40 and 50 for the SA wire (a) and the laser annealed wires treated at power 65 W and load 5 MPa (b), power 75 W and load 5 MPa (c), power 85 W and load 5 MPa (d) loaded up to 4% strain.	135
Figure 6.13 Evolution of the mechanical hysteresis measured at 3% strain as a function of the number of cycles for the samples laser annealed at 65 W and 75 W with different levels of load. The dashed line represents the corresponding trend for the straight annealed wire.	136
Figure 6.14 Evolution of the recoverable strain as a function of the number of cycles for the samples laser annealed at 65 W, 75 W and 85 W with different levels of applied load. The dashed line represents the corresponding trend for the straight annealed wire.	137
Figure 6.15 Optical micrographs of 100 μm wires laser annealed at power 65 W for the different levels of applied load analyzed.	139
Figure 6.16 Optical micrographs of 100 μm wires laser annealed at power 75 W for the different levels of applied load analyzed.	140
Figure 6.17 Optical micrographs of 100 μm wires laser annealed at power 85 W for the different levels of applied load analyzed.	141

List of Tables

Table 1.1 Main properties of binary Ni-Ti shape memory alloy [Melton, 1990].	17
Table 4.1 Phase transformation temperatures and enthalpy value for the straight annealed wires upon cooling.	64
Table 4.2 Phase transformation temperatures and enthalpy value for the straight annealed wires upon heating.	65
Table 4.3 Characteristic stress and strain values for the 100 μm straight annealed wire.	66
Table 4.4 Test conditions for the furnace treatment.	68
Table 4.5 Main characteristics of the laser system.	71
Table 4.6 Technical specifications of the load cell.	74
Table 4.7 Technical specifications of the amplifier.	74
Table 4.8 Main characteristics of the calibration system.	77
Table 4.9 Laser annealing fixed and variable parameters used in this work.	83
Table 4.10 Main characteristics of the DSC system used in the analysis.	87
Table 4.11 Main characteristics of the DMA system used in the analysis.	90

Abstract

The aim of this thesis work is the study of an innovative approach for the straight shape setting of superelastic NiTiNol thin wires by using an Ytterbium active fiber laser source.

The effect of process parameters on the functional properties of the wires has been investigated through calorimetric, mechanical and metallographic characterization. In particular, efforts were focused on studying the influence of the incident laser power and of the tensional load applied to the wire. The collected results were then compared to the performances obtained with the conventional treatments carried out in furnace on the same material, as well as to the commercially available wires, which show optimized properties. All treatments, through laser beam and furnace, were performed on cold worked Nitinol thin wires.

Results show that the optimal properties can be achieved by selecting the laser power, while the variation of the applied stress did not affect the material behavior. In conclusion, it was possible to confirm the potentiality of the laser technology for the straight shape setting of thin superelastic Nitinol wires as a valid alternative to conventional techniques, detecting in some cases even better performances than the one observed in furnace annealed samples.

Key words: Nitinol, shape memory alloys, superelasticity, shape setting, laser thermal treatment, fiber laser, mechanical characterization, differential scanning calorimetry, mechanical cycling, metallographic analysis, biomedical applications.

Sommario

Lo scopo di questo lavoro di tesi è lo studio sistematico di un metodo innovativo per effettuare il trattamento di shape setting su fili sottili in lega Nitinol superelastica attraverso l'utilizzo di una sorgente laser a fibra attiva ad Itterbio.

L'effetto dei principali parametri di processo sulle proprietà funzionali dei fili sono stati analizzati attraverso caratterizzazioni di tipo calorimetrico, meccanico e metallografico. In particolare, l'attenzione è stata posta sull'influenza della potenza incidente del fascio laser e del carico applicato al filo durante il trattamento. I risultati ottenuti sono stati poi confrontati con le prestazioni ottenute sul medesimo materiale con il trattamento convenzionale, eseguito in forno, e con il filo superelastico disponibile a livello commerciale, dotato di proprietà ottimizzate. Tutti i trattamenti sono stati effettuati su fili sottili in lega Nitinol in stato incrudito.

I risultati mostrano che le proprietà ottimali possono essere ottenute attraverso la selezione della potenza laser, mentre la variazione del carico applicato non ha influenzato il comportamento del materiale. In conclusione, è stato possibile confermare le potenzialità della tecnologia laser per il trattamento di shape setting di fili sottili in lega Nitinol superelastica come valida alternativa alle tecniche di shape setting convenzionali, ottenendo in alcuni casi prestazioni addirittura migliori di quelle osservate nei campioni trattati in forno.

Parole chiave: Nitinol, leghe a memoria di forma, superelasticità, trattamento termico laser, shape setting, laser in fibra, caratterizzazione meccanica, calorimetria differenziale a scansione, ciclaggio meccanico, analisi metallografica, applicazioni biomedicali.

Introduction

Shape memory alloys (SMAs) are functional materials able to offer a unique mix of thermo-mechanical properties, such as the shape memory effect and the superelasticity [Wayman, 1990]. In order to fix their principal properties and shape, these alloys require a specific annealing treatment, which is usually carried out by using furnace [Petrini, 2011]. Among this class of materials, Nitinol SMAs attract considerable attention between researchers, due to their particularly excellent thermomechanical properties [Hodgson, 1990; Melton, 1990]. In fact, these functional materials are very suitable for their use in different engineering fields and for increasing a large variety of different applications. In particular, thanks to their good mechanical properties, corrosion resistance and biocompatibility [Duerig, 1999], the most important applications of NiTi alloys are in the medical field, where superelasticity is mainly exploited for the realization of several components. Common examples of medical applications of Nitinol SMAs are stents, blood filtering devices [Duerig, 1999], surgical instruments [Stöckel, 2000], orthodontic archwires [Petrini, 2011], guidewires and catheters [Morgan, 2004] (see Figure 0.1).

Since their discovering, Nitinol SMAs arouse a great commercial interest, and this sudden popularity push through a detailed study of all the processes and phenomena that hide below the shape memory effect. At the same time, the development of the researches constantly opens new problems and aspects to be better understand and deepen by metallurgists. Moreover, the interest towards these alloys has been kept alive by continuous attempts to improve the material properties by means of different chemical compositions [Khalil-Allafia, 2009; Khol, 2004; Russell, 2000], variation of treatment parameters [Huang, 2001; Miller, 2001; Myara, 2014] and post-annealing processing [Miyazaki, 1986; Otsuka, 1999; Stachowiak, 1988; Zimmermann, 1997], in order to make them optimized for various applications. Nowadays, attention has turned towards superelasticity and medical applications, causing a further growth of demand for these products and the need of innovative technologies able

to provide new outlets and improvements, thus providing an attractive alternative to the conventional furnace annealing.

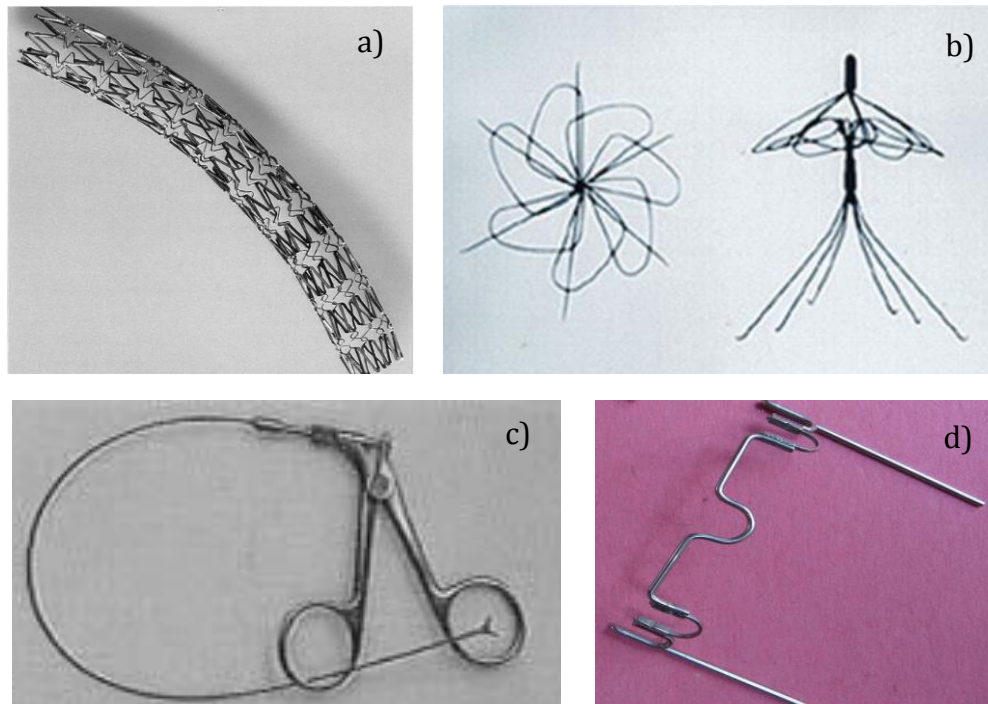


Figure 0.1 Nitinol medical devices examples: stent (a), blood filtering device (b) [Duerig, 1999], surgical instrument (c) [Stöckel, 2000] and orthodontic archwire (d) [Petrini, 2011].

Among the recently investigated unconventional techniques used for the treatment of the SMAs, the one investigated in this research is the laser shape setting. The use of laser technology offers great advantages with respect to the conventional one due to the unique property to transfer energy to the material precisely where the laser beam hits the material. This peculiarity allow for surface and localized thermal treatment of the component, to induce different physical properties on the same part, and thus produce a single component able to perform multiple functions [Bellouard, 2001]. In addition, there are also remarkable advantages at an industrial point of view, such as the considerable higher process speed and the easiness of automation of the process itself.

Although the high potential of laser technology applied to the annealing of SMAs, much systematic and intensive research work is still needed to assess the actual applicability of this process and provide the knowledge required to allow a correct tuning of process parameters. The increasing interest towards unconventional techniques applied to Nitinol superelastic SMAs, combined with the poor availability in literature of studies and results about this issue, are the main reasons that led to the realization of this thesis work about the characterization of laser annealed superelastic Nitinol wires. The whole study has been conducted at the CNR IENI (*Consiglio Nazionale delle Ricerche – Istituto per l'Energetica e le Interfasi, Lecco Unit*) laboratory and the annealing treatments has been performed using an Ytterbium active fiber laser source for making the shape setting on thin Nitinol wires.

In general, to perform the straight annealing of wires, a relatively small constant tensile force is required to constrain the sample geometry during the heat treatment [Pilch, 2009]; furthermore, in the case of laser annealing the load is mostly important to guarantee the correct positioning of the wire under the laser beam. This aspect is fundamental in order to preserve the uniformity of the alloy functional properties after the treatment. Although this stress is an important technological parameter of the NiTi superelastic wire production process, little is known about its effects on the resulting thermomechanical behavior of the wire [Malard, 2011]. More in detail, this research is focused on the investigation of the effects of different levels of tensile load in the range 5-300 MPa applied at different levels of incident power during the shape setting treatment on the functional properties of 100 μm diameter superelastic Nitinol wires. This objective implied in the first place the modification of the laser system equipment design and configuration to allow the execution of treatments of the wire under constant uniaxial load. This step required the addition of a load cell to the sample holder structure to allow the measurement and the control of the tension load applied to the wire, the investigation of the resulting system characteristics and the definition of a proper experimental campaign through preliminary tests. Then, laser treatments have been carried out varying the assigned parameters. By means of differential scanning calorimetry, mechanical analysis and metallographic characterization, the correlation between the process parameters and the

wire characteristics has been obtained. At the same time, the evolution of the effects of temperature variation on the conventional treatment has been studied for the same material as a reference. A further comparison has been performed with the commercially available straight annealed material, considered as optimized outcome from conventional treatment under uniaxial tensile load. In this way it was possible to achieve a deep understanding of the phenomena leading the superelastic behavior and to gain a good comparison between the two technologies in terms of process conditions and consequent material functional properties, so to demonstrate advantages and strengths of the laser technology applied to the annealing of superelastic Nitinol wires.

The first two chapters of this thesis work constitute the state of the art. Chapter 1 contains a general introduction about Shape Memory Alloys, describing briefly their main features, the physical processes that led their functioning and the most attractive current applications. In Chapter 2, an overview of existing literature about conventional and unconventional annealing techniques is reported, highlighting the most meaningful results. In Chapter 3, the statement of the main goals of this work is given. Chapter 4 starts with the definition of the materials used, including their calorimetric and mechanical characterization. Then, a description of the available equipment and of the modifications of the system is provided. Moreover, in this section the explanation of the preliminary operations, the design of experiments and the identification of the variables measured in this activity of research is carried out. The results of calorimetric, mechanical and metallographic characterization held on conventionally and unconventionally treated superelastic Nitinol wires are reported in Chapter 5 and 6 respectively, as well as results discussion and comparison between different conditions. Finally, in Chapter 7, the main conclusions of this work are traced and some future developments are proposed.

CHAPTER 1:

1 State of art: Shape memory alloys

The term shape memory alloys is referred to that group of metallic materials that demonstrate the ability to remember and recover a geometrical shape, even after severe deformations. In particular, these alloys are able to develop the peculiar properties of Shape Memory Effect (SME) and Superelasticity (SE) [Wayman, 1990].

Shape memory alloys exhibit these unique thermomechanical properties due to a reversible solid state phase transformation between a high temperature parent phase, austenite, and a low temperature product phase, martensite. This transformation is called Thermoelastic Martensitic Transformation (TMT). In particular, TMT can be activated by a temperature variation in the case of Thermally Induced Martensite (TIM) or by the application of an external mechanical load in the case of Stress Induced Martensite (SIM), and it allows the crystal lattice structure to accommodate to the minimum energy state for a given temperature and/or stress [Maletta, 2012].

This phenomenon give the SMA unique mechanical and functional features, reasons why they have attracted considerable attention in the past decades.

1.1 Crystallography of martensitic transformation

Martensitic transformations are displacive types of transformations, i. e. no changes in the chemical composition of the matrix occur, and are formed upon cooling from a higher temperature phase called the parent phase, or austenite. The volume fraction of martensite during temperature reduction is independent of time and it inherits the composition and atomic order of the parent phase.

Crystallographically, the transformation from austenite to martensite can be divided in two parts: the *Bain strain* and the *lattice-invariant shear*.

The Bain strain, or lattice deformation, consists of all the atomic movements needed to produce the new structure from the old. Figure 1.1 shows schematically in two dimensions the austenitic structure (see Figure 1.1(a)) and the progression to a fully martensitic structure (see Figure 1.1(d)). The intermediate passages show the evolution of the martensitic interface and the very small relative displacement of the atoms for every atomic layer transformed.

The second part of a martensitic transformation, the lattice invariant shear, is an accommodation step, which involves shape changes to adapt to the surrounding austenite. There are two general mechanisms by which this can happen: *slip* (Figure 1.2(a)) and *twinning* (Figure 1.2(b)). In both cases, each individual cell has the new martensitic structure, but the overall shape is that of the original austenite. Slip is a permanent process and is a common accommodation mechanism in many martensites, while twinning can accommodate shape changes in a reversible way. The latter, twinning, is the mechanism required to be dominant for shape memory effect to take place.

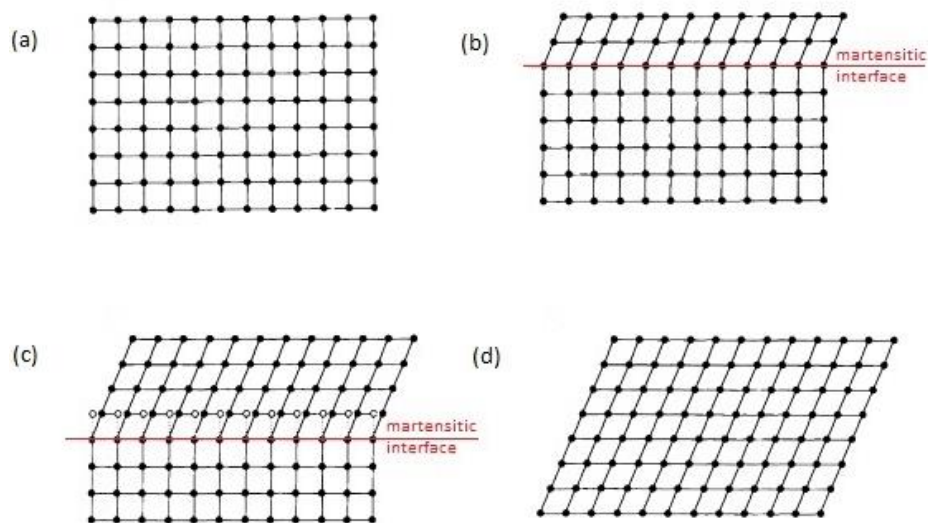


Figure 1.1 Schematic representation of the transformation from austenite (a) to martensite (b) in two dimensions [Wayman, 1990].

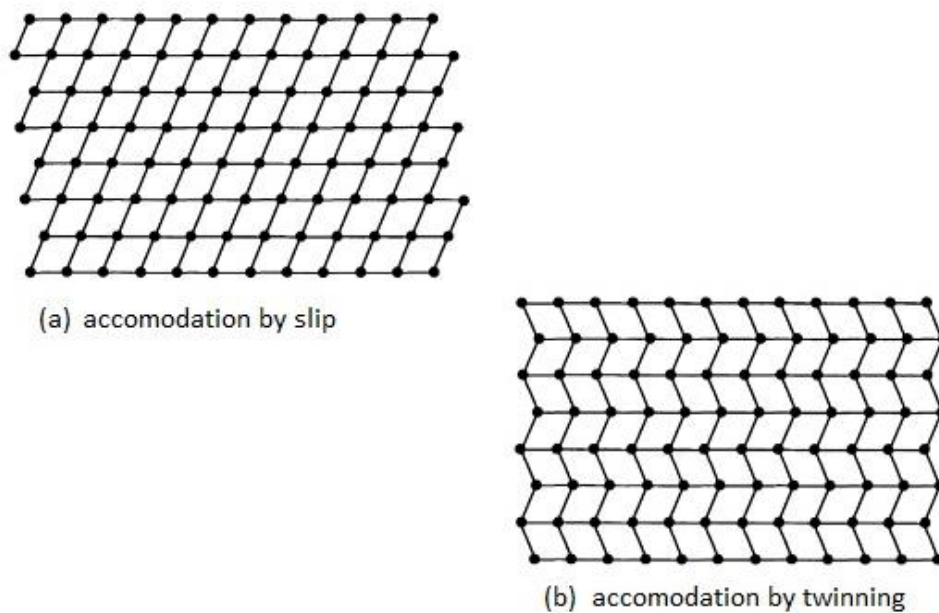


Figure 1.2 Schematic representation of the two mechanisms of accommodating the shape change due to the atomic shear of a martensitic transformation: slip (a) and twinning (b) [Wayman, 1990].

In the twinning process, the twin boundary (see Figure 1.3) is a mirror plane: when positioned on the boundary, the view in one direction is a mirror of the other. Atoms situated on that boundary see the same number and types of bonds in both directions. Key properties of twin boundaries are to be of very low energy and to be quite mobile, thus the relative stability of a martensitic phase is not strongly affected by the number or location of these boundaries.

As it can be seen from Figure 1.2 (b), in the twinned accommodation atomic bonds are not broken, so if a stress is applied to the structure, the twin boundary will easily move, producing a shape which better accommodates the applied stress. In the ideal case, a single variant of martensite can be produced by straining a sufficient amount. This process is called *detwinning*. Thus far we have only considered the twins within individual martensite plates, but crystallographic analysis has also shown that the boundaries between martensite plates also behave as twin boundaries.

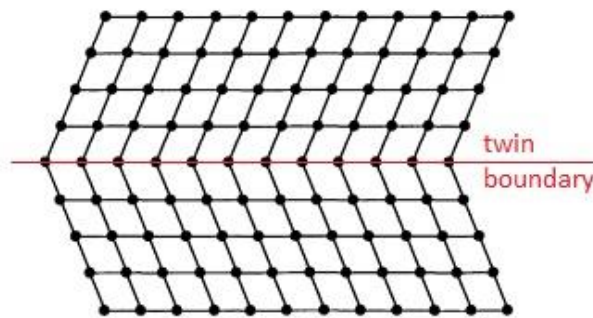


Figure 1.3 Schematic view of a twin boundary [Wayman, 1990].

In the previous part of the discussion, atom types are not distinguished, but in an alloy several types of atoms are present. Concerning distribution in the lattice sites, in shape memory alloys atoms are generally ordered, meaning that they are placed in very specific sites. During a martensitic transformation, the martensite takes on the same ordering of the austenite. This is called *inherited ordering* [Wayman, 1990].

NiTi-based shape memory alloys thermomechanical properties are due to the Thermoelastic Martensitic Transformation (TMT) between a high temperature parent phase (B2 - austenite) and a low temperature product phase (B19' - martensite). Figure 1.4 schematically shows the crystal structures of the two phases.

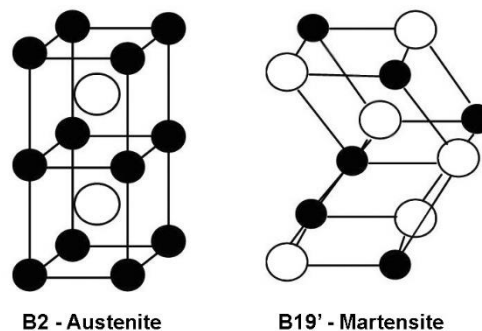


Figure 1.4 Schematic depiction of the lattice structures of austenite and martensite in NiTiInol [Maletta, 2012].

The austenitic phase is characterized by a Body Centered Cubic structure (BCC), with a nickel atom at the center of the crystallographic cube and titanium atoms at the cube's corners, while the lattice structure of the martensitic phase is monoclinic and consists of a rhombus alignment with an atom at each of the rhombus corners [Maletta, 2012].

1.2 Thermodynamic aspects of martensitic transformation

On the macroscopic scale nearly all physical properties of austenite and martensite are different, and thus as one passes through the transformation point, a variety of significant property changes occur. As a consequence, the transition between the two phases gives the possibility to obtain variable and/or tunable properties, i.e. NiTi alloys are able to change and or/adapt their response as a function of external stimuli [Maletta, 2012].

This is well illustrated in Figure 1.5. The temperatures M_s , M_f , A_s and A_f are indicated in the graph and refer to the temperatures at which the transformation to martensite starts and finishes, and the temperature at which the reversion to austenite starts and finishes. It can be noticed that there is a *hysteresis* associated with martensitic transformation; in other words, the transformation temperatures differ upon heating and cooling. The magnitude of the hysteresis depends on the alloy, but values of 20-40°C are typical for shape memory alloy systems. Microscopically, hysteresis can be thought of as the friction associated with the movement of twin-related martensite boundaries.

One property that changes in a most significant way is the yield strength. The martensitic structure can deform by moving twin boundaries, which are quite mobile. Thus the yield strength of the martensite is extremely low compared to that of the austenite which must deform by dislocation generation and movement. Only a certain amount of martensitic deformation can be accommodated by this twin movement process and once this is exceeded, the material will again deform elastically and eventually yield a second time, this time by irreversible process (dislocation

movement). The resulting unusual tensile behavior is exemplified in Figure 1.6. Note that the *plateau stress* is related to thermal hysteresis, in that both are controlled by the frictional stress of the twin boundaries.

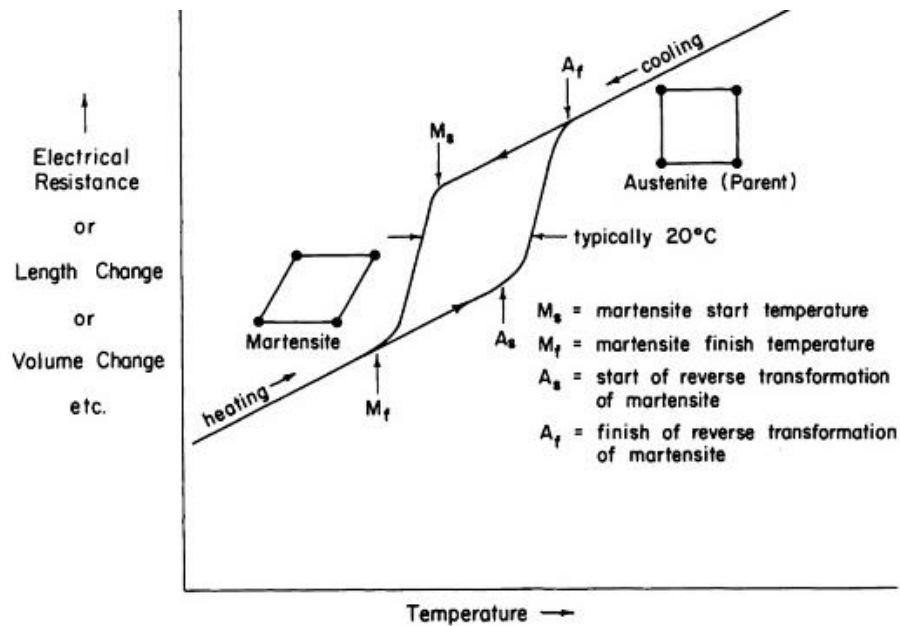


Figure 1.5 Hypothetical plot of property change vs. temperature for a martensitic transformation occurring in a shape memory alloy. The parent phase (austenite) is represented by the square lattice, which upon martensitic transformation is distorted into the rhombi [Wayman, 1990].

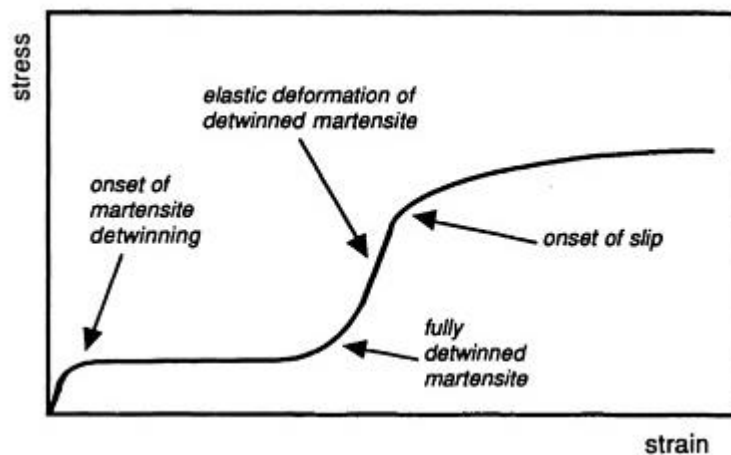


Figure 1.6 Typical stress-strain curve for a twinned martensitic material shows two distinct elastic regions and two distinct plasticity plateaus, due respectively to twin motion and slip [Wayman, 1990].

The ratio of resistances to reversible and irreversible deformation (twin movement to slip) is thus characterized by the yield strength ratio of martensite to austenite. In general one wants to maximize this ratio in a shape memory alloy, so that all deformation can be recovered upon heating [Wayman, 1990].

1.2.1 Thermally-induced martensitic transformation (TIM)

When cooling the austenitic structure a thermally-induced martensitic transformation ($B2 \rightarrow B19'$) occurs in the temperature range between martensite start temperature (M_s), and martensite finish temperature (M_f). When the martensitic structure is heated the reverse transformation between martensite and austenite ($B19' \rightarrow B2$) occurs in the range between austenite start temperature (A_s) and austenite finish temperature (A_f). These characteristic temperatures, the so called phase transition temperatures, can be regarded as material parameters, which depend on the alloy composition and on the thermomechanical processing conditions, and can be easily detected by Differential Scanning Calorimetry (DSC) investigation, as schematically shown in Figure 1.7.

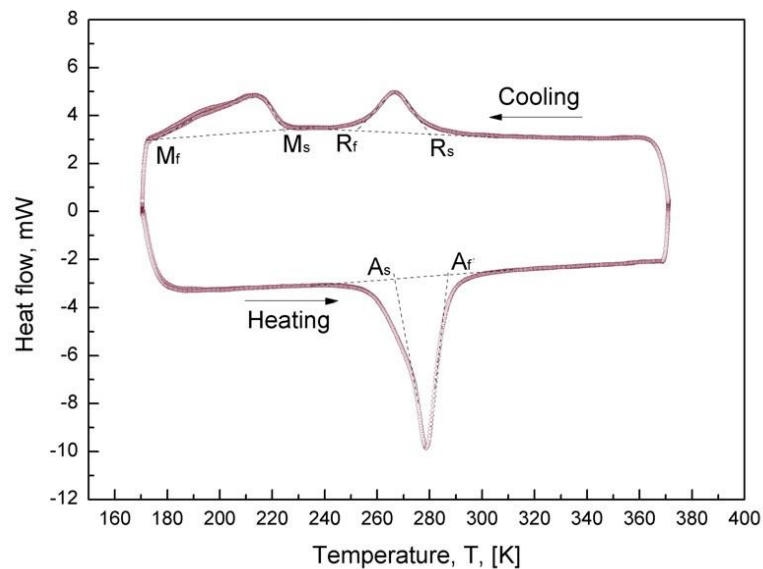


Figure 1.7 Differential scanning calorimetry thermogram of a NiTi alloy [Maletta, 2012].

Transformation from B2 cubic austenite into monoclinic B19' martensite could occur either directly or via an intermediate rhombohedral phase (R-phase), as shown in Figure 1.8. In particular, the R-phase transformation (B2→R) can be observed during cooling from Af to Ms prior to martensitic transformation, resulting in a sequential transformation B2→R→B19'. However, it is worth noting, that the B2→R transformation is observed only under specific processing conditions of the alloy. In addition, marked differences are normally observed between direct and reverse transformation temperatures as a direct consequence of the thermal hysteretic behavior of the alloy, as illustrated in Figure 1.8. In particular, this figure shows the thermal hysteresis describing the evolution of the volume fraction of martensite together with the characteristic transformation temperatures [Maletta, 2012].

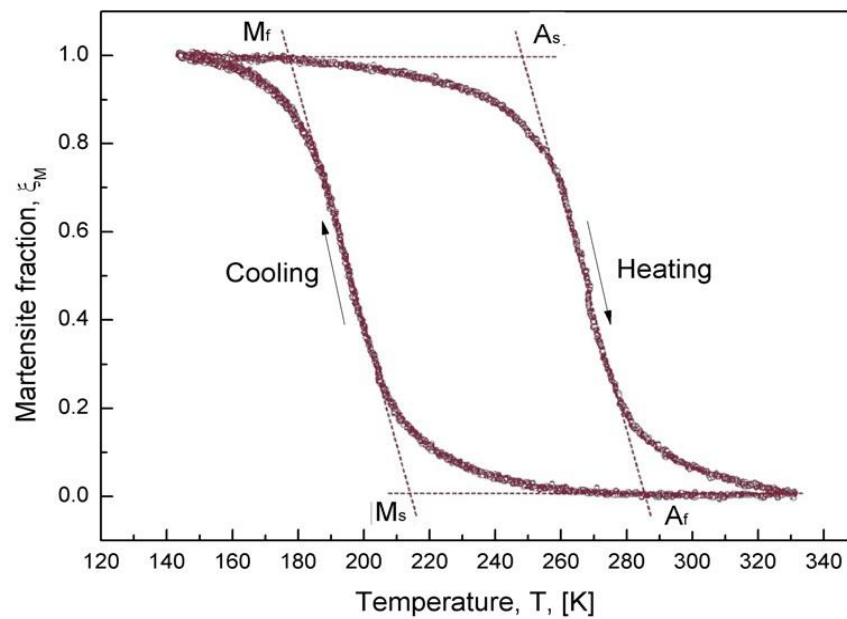


Figure 1.8 Thermal hysteresis of a NiTi alloy describing the evolution of volume fraction of martensite [Maletta, 2012].

1.2.2 Stress-induced martensitic transformation (SIM)

When a mechanical load is applied to the austenitic structure the stress-induced $B2 \rightarrow B19'$ transformation occurs, corresponding to a plateau in the stress-strain curve of the alloy. If the mechanical load is removed the reverse $B19' \rightarrow B2$ transformation occurs which is related to another stress plateau and allows an almost complete strain recovery. Figure 1.9 illustrates an example of stress-strain curve of a NiTi alloy exhibiting stress-induced phase transformation mechanisms, together with the characteristic transformation stresses of the alloy, i.e. the stresses for direct $B2 \rightarrow B19'$ transformation (σ_s^{AM} , σ_f^{AM}) and the stresses for reverse $B19' \rightarrow B2$ transformation (σ_s^{MA} , σ_f^{MA}).

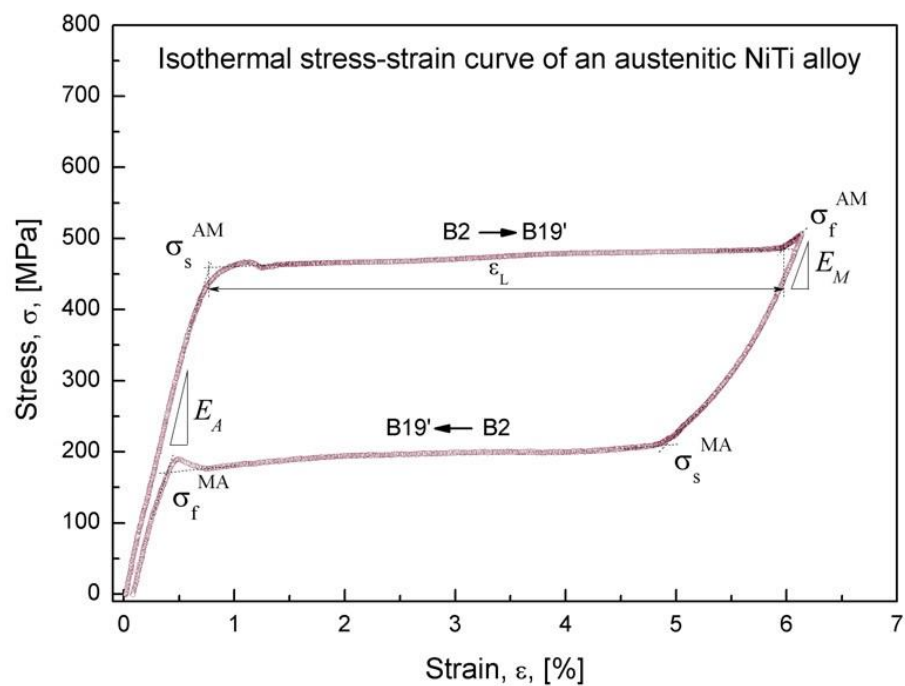


Figure 1.9 Stress-strain curve of an austenitic NiTi alloy with characteristic transformation stresses [Maletta, 2012].

1.3 Functional properties of SMAs

1.3.1 One way shape memory effect (OWSME)

Shape Memory Effect (SME) is the ability of a SMA to remember a predetermined shape once deformed at low temperature and spontaneously return to the original, pre-deformation shape. The basis for the memory effect is that the materials can easily transform to and from martensite. In NiTi alloys, this property can be attributed to the combination of two microstructural changes: detwinning of martensitic variants and thermally induced phase transformation [Maletta, 2012].

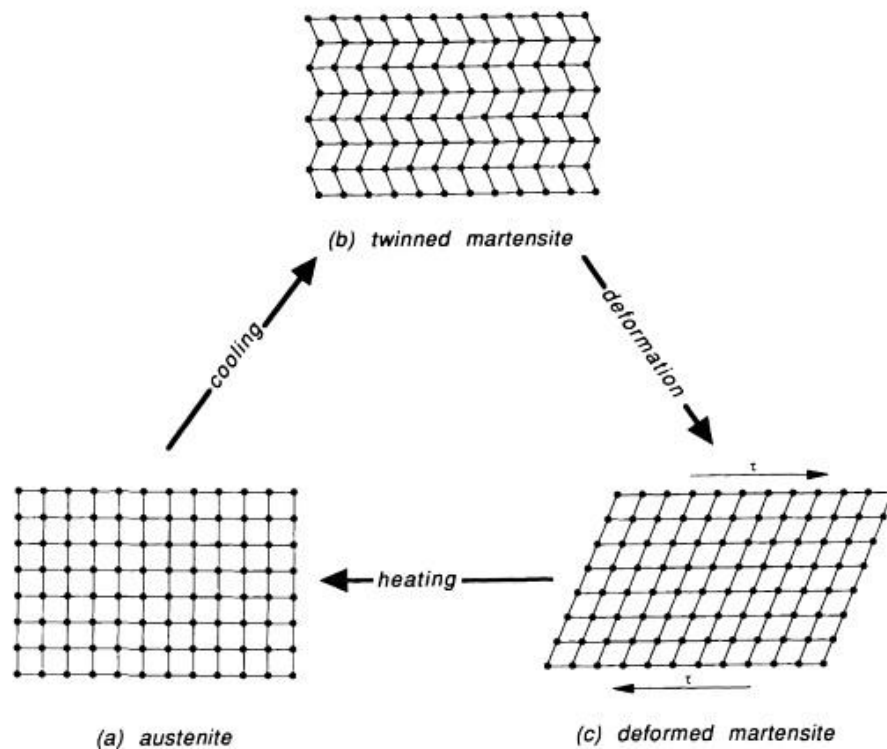


Figure 1.10 Two dimensional scheme of shape memory process: austenite (a) is cooled to form twinned martensite (b) without undergoing a shape change, then it is deformed by moving twin boundaries (c) [Wayman, 1990].

Martensite is generally a lower symmetry phase than is the austenite, so there are several ways in which martensite can form from austenite, but

there is only one possible route which will return the austenitic structure. Looking at the example in Figure 1.10, there are two possible variants of martensite: the self accommodating variant obtained upon cooling from austenite (b) and the deformed one (c). Heating either state will return to the same austenitic structure and shape (a).

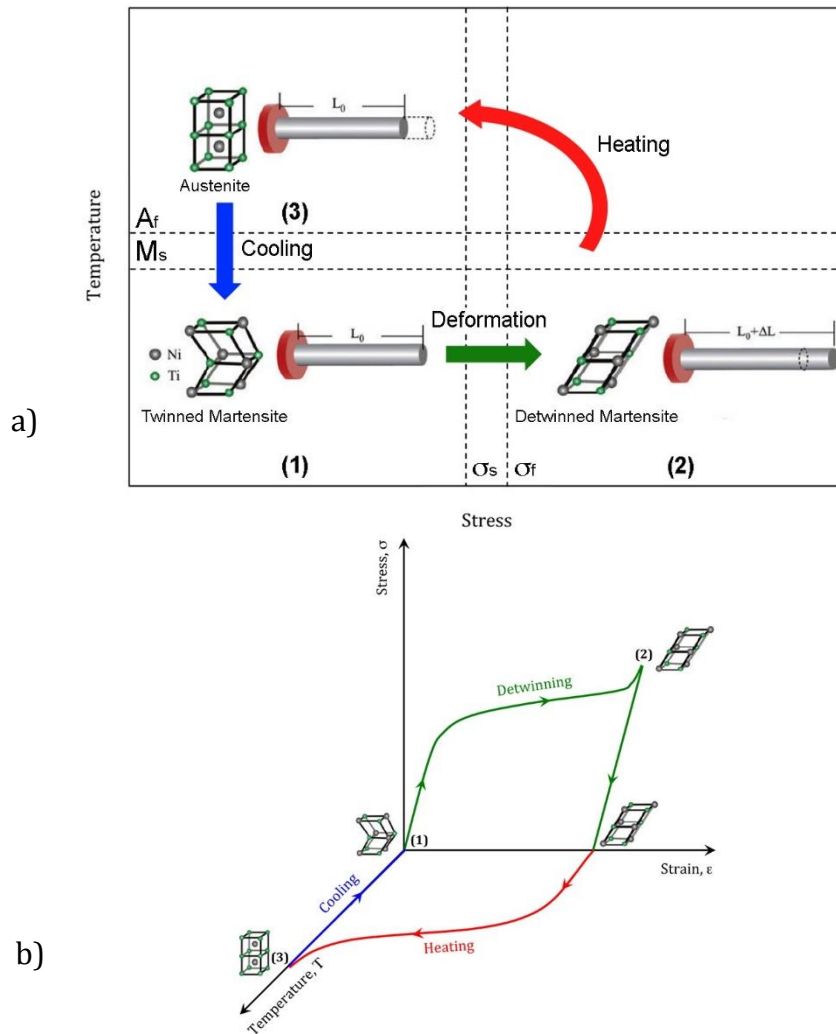


Figure 1.11 Schematic depiction of phase transition mechanism (a) and stress-strain-temperature response (b) [Maletta, 2012].

The shape memory effect can be described with reference to the phase transition mechanism described in Figure 1.11. There is no change in the shape of a specimen cooled from above A_f to below M_f . When the specimen is deformed below M_f it remains so deformed until it is heated. The shape recovery begins at A_s and is completed at A_f . At the inflection point between A_s and A_f , about 50% of the original shape is recovered. Once the shape has recovered at A_f there is no change in shape when the specimen is cooled to below M_f and the shape memory can only be reactivated by deforming the martensitic specimen once again [Wayman, 1990]. Materials that exhibit shape memory only upon heating are referred to as having a *one-way shape memory* (OWSM) [Hodgson, 1990].

1.3.2 Two way shape memory effect (TWSME)

With respect to *one-way shape memory*, some alloys also undergo a change in shape upon recooling. These materials have a *two-way shape memory* (TWSM) [Hodgson, 1990]. Two-way shape memory alloys are able to remember a cold shape, linked to the martensitic structure, and a hot shape, linked to the austenite. As a consequence, during repeated heating and cooling, the material changes its shape in a reversible way, through a hysteresis loop, as schematically illustrated in Figure 1.12 [Maletta, 2012].

This effect can be easily understood through an example in Figure 1.13. In the upper part of the figure, a collapsed SMA spring is deformed by extension below M_f . The original spring shape (contracted) is recovered following heating to above A_f . The contracted shape remains when the specimen is again cooled to below M_f . This is the OWSM behavior. In contrast, the TWSM is depicted in the lower half of the figure, in which case a contracted spring extends when heated to above A_f , but then spontaneously contracts when again cooled below M_f [Wayman, 1990].

To induce the two-way behavior, proper thermomechanical treatments are required, called *training*, which usually involve repeated deformations and transformations between austenite and martensite. This thermomechanical process produces a dislocation structure and, consequently, creates an anisotropic stress field that benefits the formation of preferentially

oriented martensite variants, resulting in a macroscopic shape change between the phase transition temperatures [Hamilton, 2004].

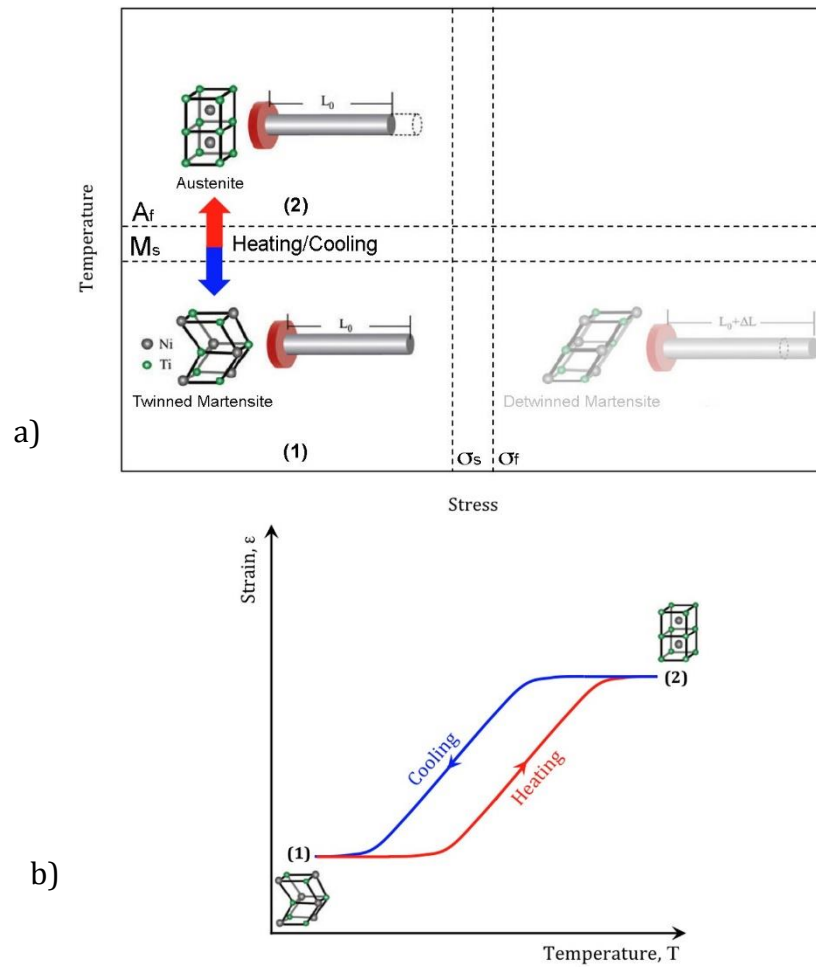


Figure 1.12 Schematic depiction of the two-way shape memory effect: phase transition mechanisms (a) and strain-temperature hysteretic response (b) [Maletta, 2012].

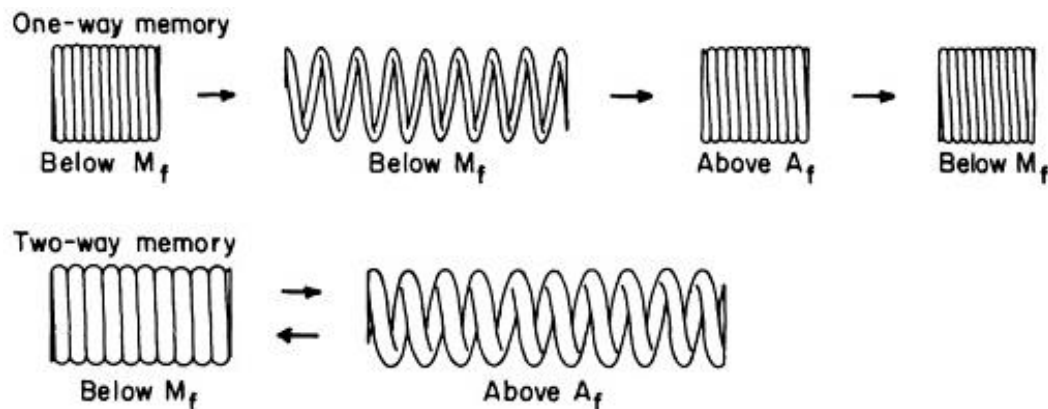


Figure 1.13 Comparison of the one-way (upper) and two-way (lower) shape memory effects using a coil spring as an example [Wayman, 1990].

1.3.3 Superelasticity

We now consider another type of shape memory which is temperature independent: Superelasticity (SE) or Pseudoelasticity (PE). The formation of martensite is a thermoelastic process, meaning that an incremental decrease in temperature between M_s and M_f results in a slight growth of existing martensite plates and the nucleation of new ones, but when the temperature is incrementally raised, the newly nucleated plates disappear and those which grew slightly on incremental cooling correspondingly shrink back a little. In other words, there is an equivalence between temperature and stress: a decrease in temperature is equivalent to an increase in stress, both stabilizing martensite. Normally on cooling, the martensite forms at M_s under no stress. But in the same material, martensite can form above M_s if a stress is applied, and the martensite so formed is termed stress-induced martensite (SIM). The driving force for the transformation is now mechanical, as opposed to thermal [Wayman, 1990].

The pseudoelastic (PE) effect in NiTi alloys consists in the high strain recovery capability (up to 10%) observed during isothermal loading/unloading cycles carried out at temperature $T > A_f$, i.e. when the alloy is in austenitic conditions. This functional property can be directly attributed to the reversible stress-induced martensitic transformations. In particular, Figure 1.14 illustrates that if a mechanical load is applied to

austenitic structure, the $B2 \rightarrow B19'$ transformation occurs and, on the macroscopic scale, large mechanical deformation are achieved through a stress-strain transformation plateau.

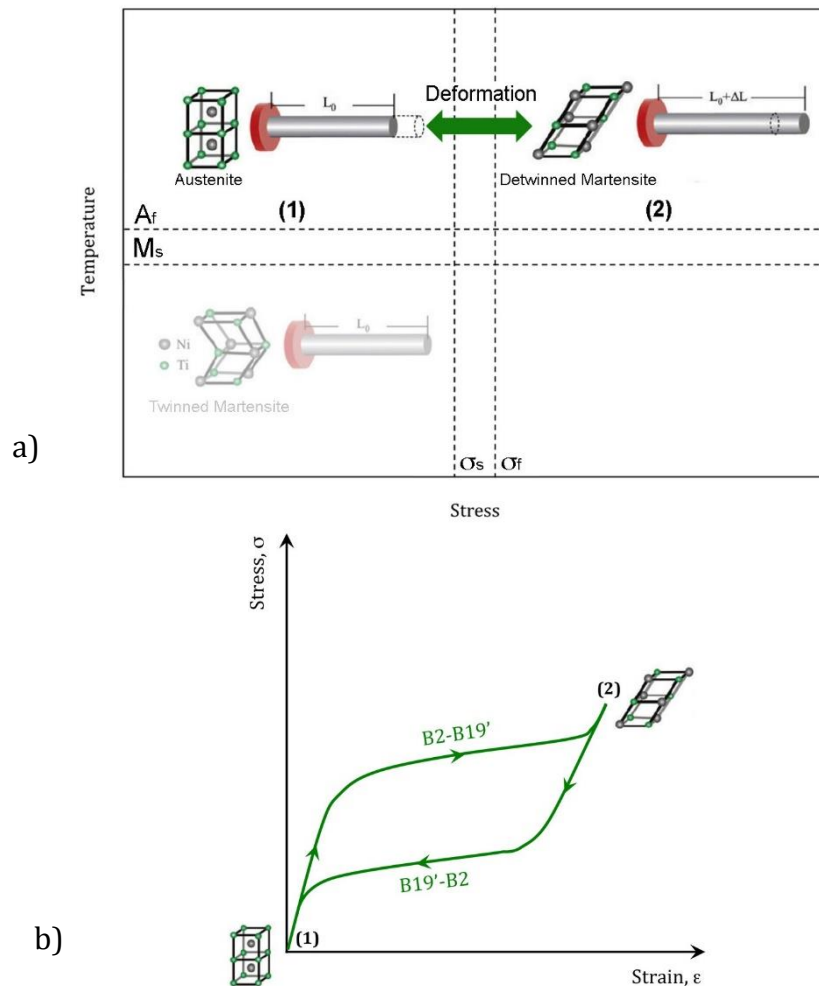


Figure 1.14 Schematic depiction of the pseudo elastic effect: stress-induced phase transition mechanisms (a) and stress-strain hysteresis response (b) [Maletta, 2012].

However, if the mechanical load is removed the reverse $B19' \rightarrow B2$ transformation occurs and, consequently, the material is able to recover its original shape through an unloading plateau in the stress strain curve.

However, the reverse transformation occurs at lower stress values resulting in a marked stress-strain hysteretic behavior [Maletta, 2012].

Figure 1.15 illustrates the the stress-strain hysteretic behavior of a commercial pseudoelastic NiTi alloy in the first 25 mechanical cycles for a fixed value of total strain. These materials exhibit a marked evolution of the stress-strain hysteretic behavior in the first mechanical cycles, up to a stable response, due to the formation of stabilized martensite, which causes a reduction of the pseudoelastic recovery of the SMA. It can be seen that the stress-strain loops becomes more stable after 20 cycles [Maletta, 2009].

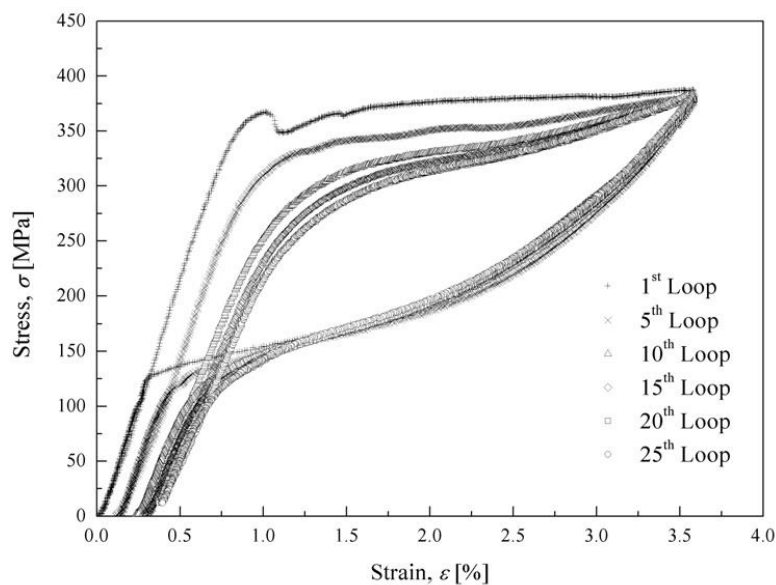


Figure 1.15 Evolution of the stress-strain response of a commercial pseudoelastic NiTi alloy during the first 25 mechanical cycles for a maximum applied deformation of 3.5% [Maletta, 2009].

1.4 Nitinol

Although in the last decades a relatively wide variety of alloys were discovered to exhibit the shape memory effect, only few kinds of SMA are of commercial interest. To date, this has been mainly the nickel-titanium alloys and copper-base alloys. Among these alloys the near equiatomic NiTi binary system shows the most exploitable characteristics due to the high stress and strain recovery capabilities associated with their functional

properties, namely pseudoelastic effect (PE) and shape memory effect (SME). Ni-Ti based SMA are usually called Nitinol, due to their composition and their place of discovery, the *Naval Ordnance Laboratory (NOL)*, in the 1960's [Hodgson, 1990].

1.4.1 General properties

Shape memory alloys based on nickel and titanium have to date provided the best combination of material properties for most commercial applications [Pelton, 1990].

Nickel-Titanium alloys are extraordinary compounds because they have a moderate solubility range for excess nickel or titanium and they also exhibit a ductility comparable to most ordinary alloys. This solubility allows alloying with many of the elements to modify both the mechanical properties and the transformation properties of the system. Excess nickel, in amounts up to about 1%, is the most common alloying addition. It strongly depresses the transformation temperature and increases the yield strength of the austenite. Other frequently used elements are iron and chromium, while common contaminants such as oxygen and carbon have to be minimized (shift transformation temperature and degrade the mechanical properties). The major physical properties of the basic binary Ni-Ti system and some of the mechanical properties of the alloy in the annealed condition are shown in Table 1.1 for an equiatomic alloy.

Melting temperature	1300 °C
Density	6.45 g/cm ³
Young's modulus (austenite)	75GPa
Young's modulus (martensite)	28 GPa
Yield strenght (austenite)	195-690 MPa
Yield strenght (martensite)	70-140 MPa
Ultimate tensile strenght	750-960 MPa
Transformation temperatures	From -200 to 110 °C

Table 1.1 Main properties of binary Ni-Ti shape memory alloy [Melton, 1990].

One of the most exploited properties of Nitinol is the high biomechanical compatibility: the extraordinary compliance of nitinol with biological materials (see Figure 1.16) clearly makes it the metal most suitable for applications in the biomedical field, leading to more rapid healing times and less trauma to surrounding tissue [Duerig, 1999].

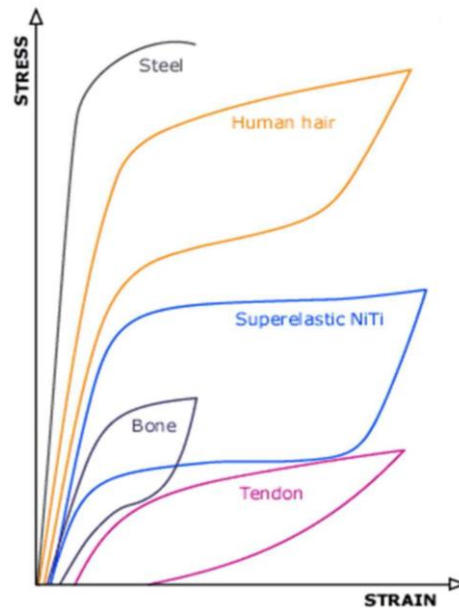


Figure 1.16 The stress–strain curves of several natural biological materials are superimposed on Nitinol stress-strain curve [Duerig, 1999].

On a metallurgical point of view, Ni-Ti SMA are ordered intermetallic compounds based on the equiatomic composition. From the phase diagram (see Figure 1.17), this compound exists as the stable phase down to room temperature. However, despite the increasing interest and the efforts of many researchers to better understand these unusual mechanisms, the use of NiTi alloys is currently limited to high-value applications, such as medical devices. This is mainly due to the high cost of the raw material as well as to the complex component manufacturing; in fact, machining by turning or milling is very difficult and requires special tools and practices. Also welding, brazing or soldering of these alloys is generally difficult [Hodgson, 1990]. In addition, an accurate control of the processing parameters must be carried out as the functional and mechanical properties of NiTi alloys are

significantly affected by the thermo-mechanical loading history experienced during manufacturing [Maletta, 2012].

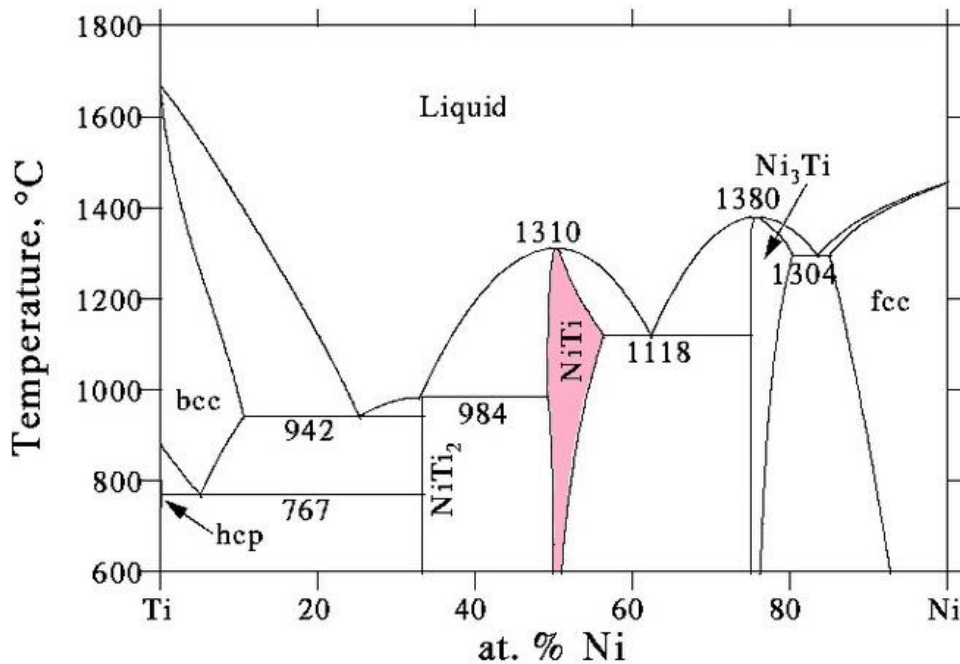


Figure 1.17 Ni-Ti phase diagram [Bram, 2002].

1.4.2 Influence of grain size

While single crystal specimens of near-equiatomic Ti-Ni alloy show incomplete pseudoelasticity at temperatures above A_f , polycrystal specimens of the same alloy show a complete pseudoelasticity at temperature above A_f . Figure 1.18 illustrates the grain size dependence of recoverability of a Ti-50,5 at % Ni alloy which was annealed at 800 °C for 3,6 ks and quenched. The stress-strain curves in the figure were obtained by tensile-testing the specimen with three different grain sizes: (a) 50 μm , (b) 1 mm and (c) single crystal. The tests were made at 40 °C, which is 10 °C above A_f . It is clearly seen that the reduction of grain size is very effective for improving the pseudoelasticity [Otsuka,1999].

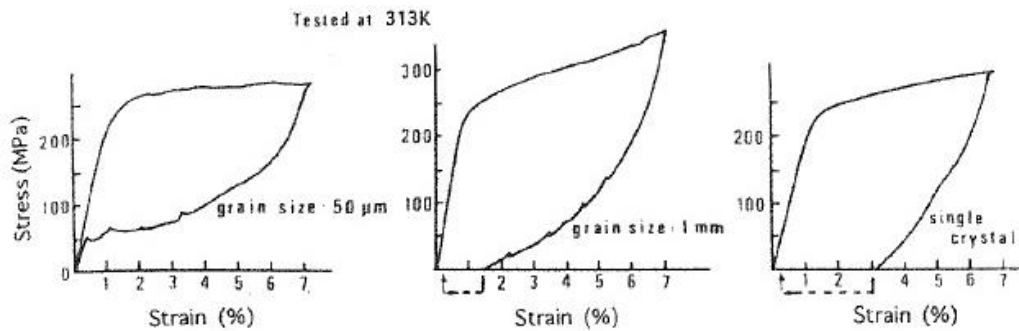


Figure 1.18 Grain size dependence of pseudoelasticity in Ti-50.5 at % Ni alloy [Otsuka, 1999].

1.4.3 Influence of chemical composition

NiTi is an ordered intermetallic compound which exists as a stable phase down to room temperature. However, the stoichiometric range is rather narrow at low temperatures. The conventional compositions of NiTi alloys is near-equiatomic, which conventionally refers to alloys that have 50–50.5 at.% Ni. In Figure 1.19, the equilibrium Ti-Ni phase diagram in the vicinity of TiNi is shown [Bastin, 1974].

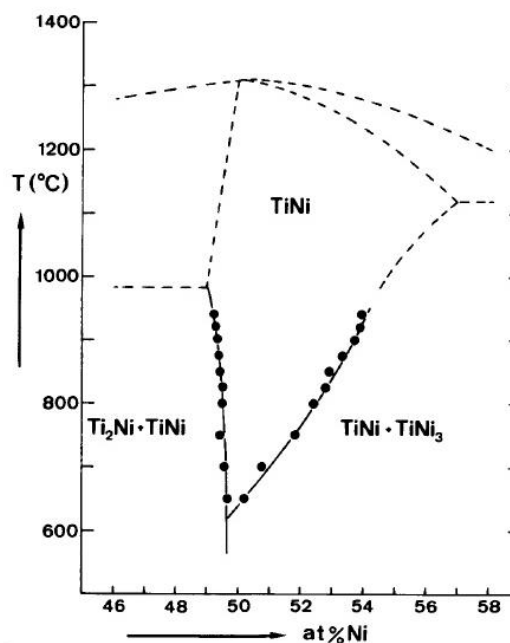


Figure 1.19 Equilibrium phase diagram for Ti-Ni in the vicinity of TiNi [Bastin, 1974].

It is well known that Ni content has main influence on SMA final characteristics, so many studies with regard to the influence of the chemical composition in binary NiTi alloys have been conducted. Even a very small change in alloy composition can have a very large effect on the transformation temperatures, in particular it was established a decrease in temperatures resulting from an increase in Ni concentration.

As shown in the equilibrium phase diagram, Ni-rich and Ti-rich alloys contain precipitates of a second intermetallic phase such as TiNi_3 or Ti_2Ni , so they have characteristic differences. In particular, Ni-rich alloys exhibit a strong dependence of the M_s temperature on the chemical composition, which is lower for Ti-rich alloys. The M_s temperature of Ni-rich alloys is below room temperature, while maximum M_s temperature between 90 and 100 °C are reached at a Ni content below 49.5 at.% [Kohl, 2004].

The transformation temperatures variation due to changes in the chemical composition are plotted in the graph of temperature M_s as a function of the nickel atomic content reported in the study of Melton et al (see Figure 1.20). A practical consequence of this phenomenon is that a precise composition control is required when melting the alloy [Pelton, 1990].

In the study of Khalil-Allafia et al., the influence of Ni atomic content on characteristic temperatures and entropy changes in martensitic transformation of NiTi alloys have been investigated. In this work, the binary NiTi alloys with different compositions in the range of 50.3–51 at.% Ni were annealed at 850 °C for 15 min and then quenched in water. In order to determine the characteristic temperatures and enthalpy changes of the forward and the reverse martensitic transformation, DSC experiments were performed. The enthalpy changes of forward and reverse martensitic transformation as a function of Ni atomic composition are shown in Figure 1.21. It is possible to observe that in binary NiTi alloys, the enthalpy changes of forward and reverse martensitic transformation decrease with increase of Ni atomic content [Khalil-Allafia, 2009].

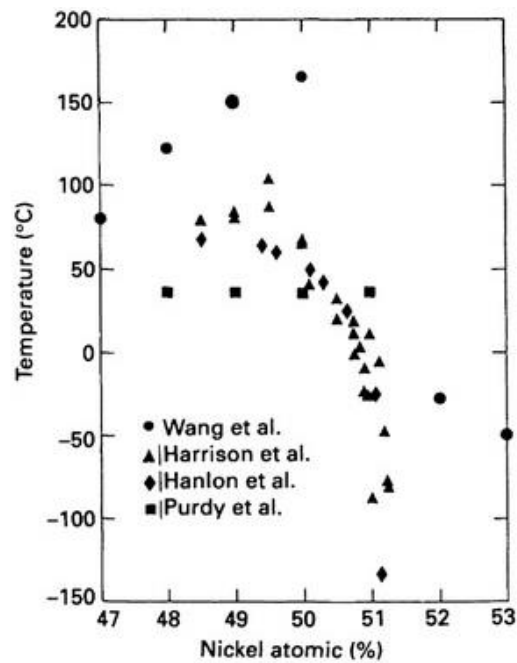


Figure 1.20 Dependence of the transformation temperature M_s on composition [Melton, 1990].

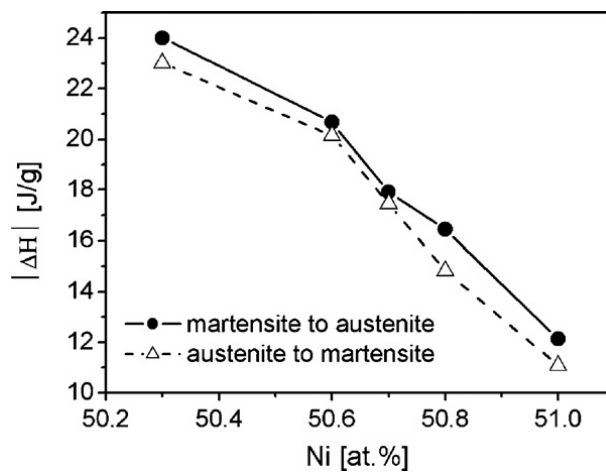


Figure 1.21 Enthalpy changes of forward and reverse martensitic transformation as a function of Ni atomic content in binary NiTi alloys [Khalil-Allafia, 2009].

Russell investigates the correlation between the chemical composition of Nitinol and the austenite finish temperature (A_f), which represents the completion of the phase transformation upon heating. This is considered

one of the most important material properties since it dictates the transition between shape memory and superelastic properties. As mentioned before, the alloy transformation temperatures are determined by the ratio of nickel and titanium in the alloy and are extremely sensitive to very small changes in alloy composition. As shown in Figure 1.22, a 1% shift in the amount of either nickel or titanium in the alloy will result in a 100°C change in alloy transformation temperature. So, starting from the chemical composition of the alloy, we are able to predict if the material behavior will be superelastic or shape memory. Furthermore, many applications require the alloy transformation temperatures to be controlled to within $\pm 5^\circ\text{C}$, meaning that the alloy composition must be controlled to within $\pm 0.05\%$ [Russell, 2000].

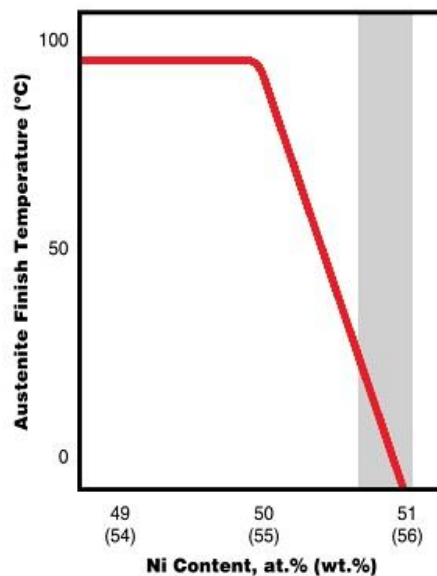


Figure 1.22 Schematic of the effect of the Ni content of Nitinol on the alloy phase transformation temperature A_f . The shaded region represents the area covered by typical binary superelastic Nitinol alloys [Russell, 2000].

1.5 Applications

Because of their unique mechanical properties, SMAs are already being used and have the potential to be used for a wide variety of purposes. The shape memory effect can be used to generate motion and/or force, while

superelasticity allows energy storage [Stockel, 2000]. Due to these features NiTi alloys are currently used in an increasing number of applications in many fields of engineering, for the realization of smart sensors and actuators, joining devices, hydraulic and pneumatic valves, release/separation systems, consumer applications and commercial gadgets [Maletta, 2012]. Above all, the properties of the Ni-Ti alloys indicate their greater use in the medical field [Hodgson, 1990].

A brief selection of current applications is presented in the following sections, highlighting the improvements offered by the use of Nitinol components.

1.5.1 Medical applications

As mentioned above, the properties of Ni-Ti alloys make them extremely suitable for biomedical applications. In fact, the material is extremely corrosion resistant, demonstrates excellent biocompatibility, can be fabricated into the very small sizes, and has properties of elasticity and force delivery that highly suggest this kind of implementation [Hodgson, 1990].

1.5.1.1 Stents

One of the most celebrated superelastic medical devices is the self-expanding stent. This term is reserved for devices used to scaffold or brace the inside circumference of tubular passages or lumens, such as the esophagus, biliary duct, and most importantly, a host of blood vessels including coronary, carotid, iliac, aorta and femoral arteries. Stenting in the cardiovascular system is most often used as a follow-up to balloon angioplasty, a procedure in which a balloon is placed in the diseased vessel and expanded in order to reopen a clogged lumen (called a stenosis) [Duerig, 1999].

The stent is shape set into the open condition and then compressed and inserted into the delivery catheter. When the distal end of the catheter is in the correct position the stent can be pushed out and will self-expand against the vessel wall. The catheter may then be withdrawn leaving the

stent permanently in place. The majority of stents are made from laser cut tubing (see Figure 1.23). The expanded diameter of a nitinol stent laser cut from tubing is typically 2–6 times greater than the tube it was cut from. The superelasticity of nitinol is the predominant property of interest for using it in stent applications [Morgan, 2004].

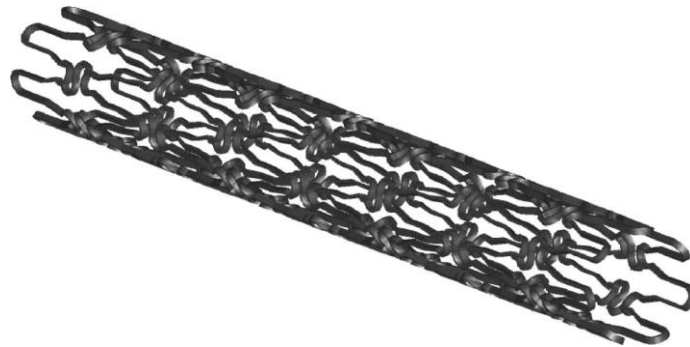


Figure 1.23 Model of stent laser cut from nitinol tubing [Morgan, 2004].

1.5.1.2 Nitinol guidewires

Nitinol have found extensive use in angiography as guidewires, devices inserted through an artery to help the passage of the catheters which contain the contrast medium used to locate blockages in circulation. The guidewire acts as a rail for the catheter to travel along until it reaches the distal location. In most cases, the route through which the guidewire must pass may be very long and tortuous, involving very small vessels with tight radii and branching points. The strains imposed on the guidewires may result in permanent deformation and kinking of the wire. The mechanical aspects of nitinol behaviour make it an ideal choice for this type of application [Morgan, 2004].

1.5.1.3 Inferior vena cava filters

This devices, also known as *Simon filters*, are employed to prevent pulmonary embolism in patients affected for which anticoagulant drugs are ineffective or not tolerated. The idea of the Simon filter is that it traps the embolisms in its 'frame' where over time they will gradually dissolve. The device exploit the Nitinol shape memory effect [Duerig, 1999]. It is collapsed in the martensitic phase and flushed with chilled saline solution

during insertion into the patient. When the deployment site is reached the circulating saline is switched off and the comparatively warm blood causes the filter to open out to its 'heat set' shape, shown in Figure 1.24 (a) [Morgan, 2004].

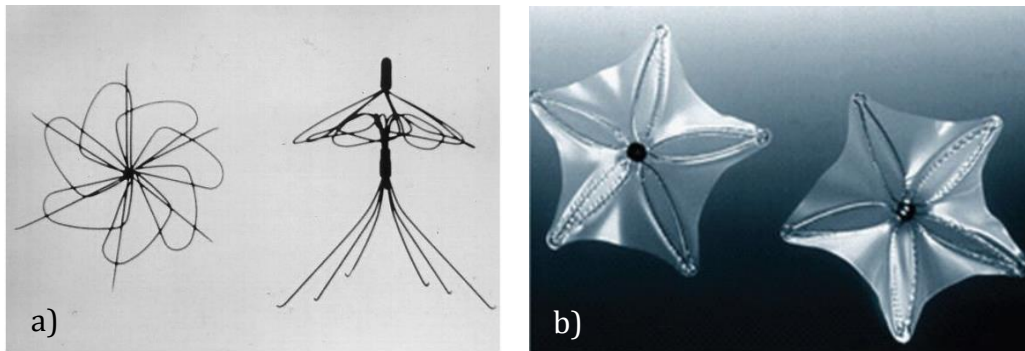


Figure 1.24 Simon vena cava filter (a) and device to close ventricular septal defects [Petrini, 2011].

1.5.1.4 Atrial septal occlusion devices

Other common devices are those used to close ventricular septal defects, which are characterized by the presence of an atrial hole in the surface between the two low pressure chambers of the heart. They constitute an appealing alternative to the surgical method, highly invasive and hazardous. The device is made of SMA wires and of an impermeable polyurethane membrane (see Figure 1.24 (b)). The insertion procedure consists of three steps: positioning of the catheter with the crimped device through the superior vena cava, positioning of the catheter tip in the left atrium and release of half of the device, and completion of procedure via release of the remaining part of the device in the right atrium. According to the device typology, both shape memory and pseudoelastic effects are utilized [Petrini, 2011].

1.5.1.5 Surgical instruments

The ability of SMA to remember highly deformed shapes and the presence of the plateau in the stress-strain curve, which assures a limitation in the force transmitted by the device thereby avoiding excessive damage of the tissues, has allowed the production of effective, mini-invasive surgical

instruments, which are useful in many interventional and endoscopic procedures (see Figure 1.25) [Petrini, 2011].

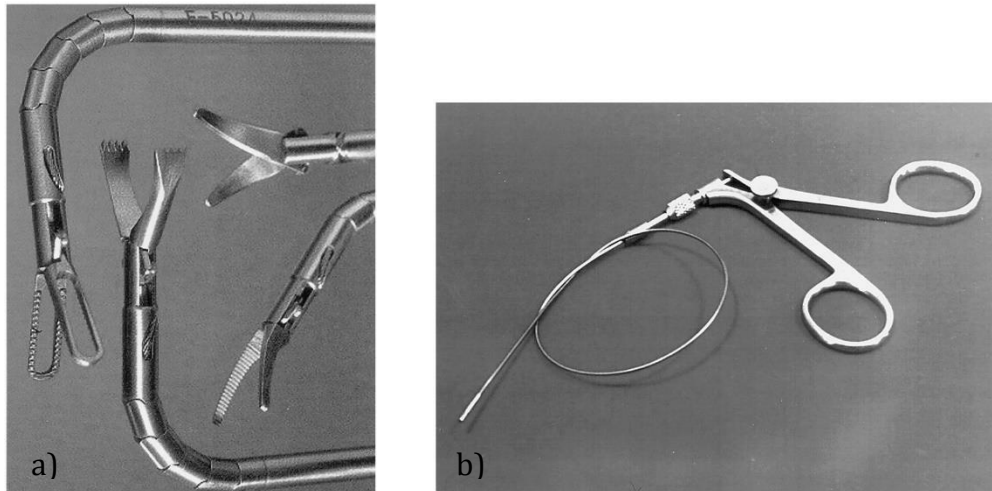


Figure 1.25 Innovative endoscopic instruments that use nitinol rods to actuate tools (a) and nitinol tubing with an internal actuation wire that allows it to operate while tied in a knot (b) [Duerig, 1999].

These include: biopsy forceps, tissue ablaters, hingeless graspers and retrieval baskets for laparoscopy [Morgan, 2004].

1.5.1.6 Orthodontic archs and distracters

An important feature of superelastic materials is that they exhibit constant unloading stresses over large strains, so the force applied by a superelastic device is determined by temperature and not by strain. The palatal arch (see Figure 1.26 (a)) was the first product to use this property: due to the constancy of the body temperature, it applies a constant stress over a wide range of shapes [Duerig, 1999]. During the insertion phase, the physician deforms the wire; once positioned, the material tries to go back to austenite phase (stable at the buccal cavity temperature) and hence tries to recover the original shape. Pseudoelastic behavior is also exploited for producing orthodontic distracters (see Figure 1.26(b)), which are used for solving the problem of teeth overcrowding in the mandible district. Also in this case the use of SMA assures tensile forces nearer to the physiological values and constant in time. These forces create stress conditions that improve the

tissue growth and hence teeth movement into the correct position [Petrini, 2011].

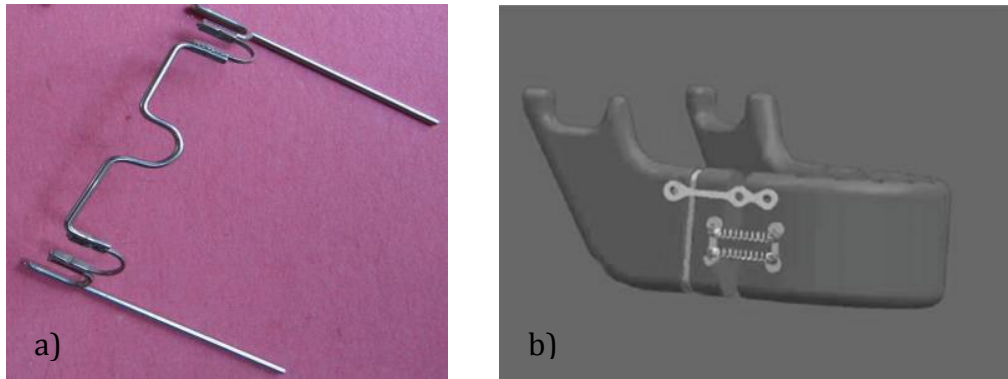


Figure 1.26 Palatal arch (a) and orthodontic distracters (b) [Petrini, 2011].

1.5.1.7 Orthopedic devices

The stress generated by SMA when the shape recovery is constrained is exploited for fracture treatment by using orthopedic staples or plates (see Figure 1.27 (a)). The device is deformed in the martensitic phase and hence inserted where the fracture is present. The body temperature induces the shape memory effect; because of the constrained recovery, the plates induce a constant stress, consequently joining the two fractured pieces. It has also been proposed to exploit the shape memory effect for designing a spinal vertebrae spacer with a rounded shape to be used on behalf of the damaged intervertebral disc (see Figure 1.27 (b)).

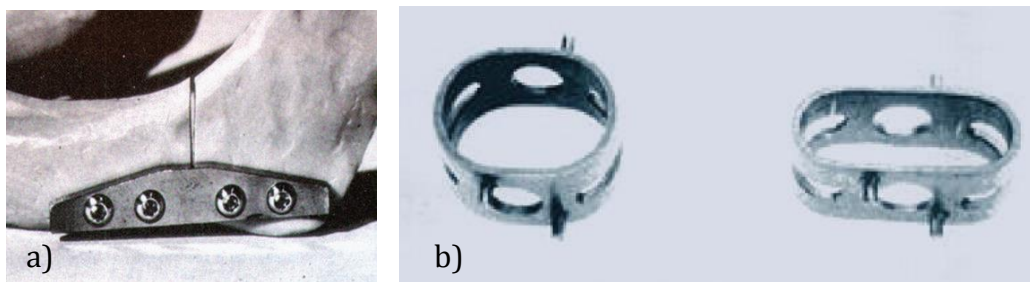


Figure 1.27 NiTi plate for mandible fracture (a) and spinal vertebrae spacer (b) [Petrini, 2011].

Because of material's high deformability in martensitic phase, it is possible to modify the device shape for facilitating the insertion between the

vertebrae, where the device recovers to its original shape. Another interesting application of SMA in the orthopedic field refers to the development of gloves for promoting the movements of hands by positioning SMA wires in correspondence of the fingers. In this application the two-way shape memory effect is employed; heating or cooling, the wires contractor stretch and accordingly the hand is closed or opened [Petrini, 2011].

1.5.2 Engineering applications

The unique behaviour of NiTi SMAs have spawn innovative applications in the aerospace, automotive, automation and control, appliance, energy, chemical processing, heating and ventilation, safety and security, and electronics (MEMS devices) industries [Jani, 2014].

1.5.2.1 Fasteners and tube couplings

This is one of the first successful application of SMAs for engineering purposes. In this application, a coupling made of Ti-Ni is machined with an I.D. smaller than the diameter of the tubing it is designed to join. It is then radially expanded in the martensitic state, making it large enough to slip over two tube ends. After tubes are inserted, the coupling is heated to a temperature above A_f [Stockel, 2000]. The coupling shrinks, owing to the shape memory effect, and the joint is thus secured (see Figure 1.28 (a)).

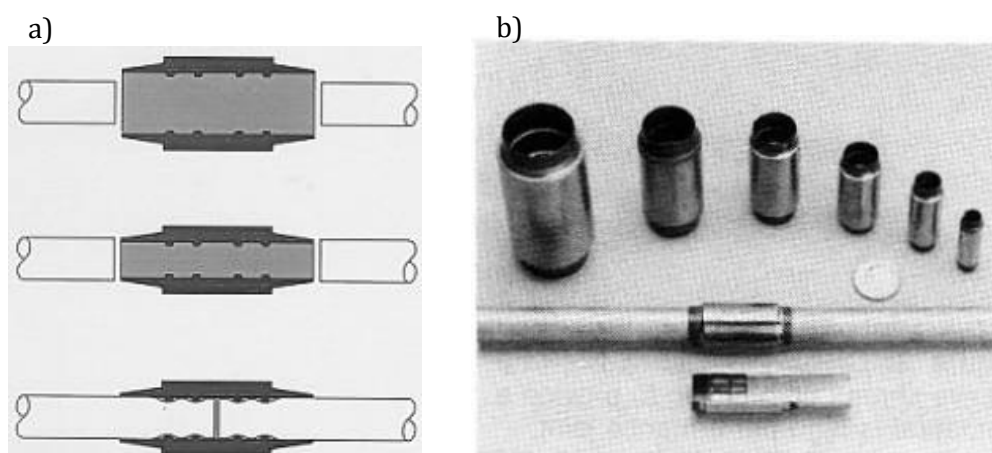


Figure 1.28 (a) Scheme of a coupling, machined and expanded (top), after free recovery (middle) and installed on a tube (bottom) [Stockel, 2000]. (b) Aircraft hydraulic couplings [Duerig, 1989].

Examples of aircraft hydraulic couplings are reported in Figure 1.28 (b). There were two reasons for their success: the coupling was reliable, and cost was not a serious concern, since it was for military use. However, for commercial use, cost is an important factor [Otsuka, 2002].

1.5.2.2 Thermal actuators

Recent research work has shown that SMA actuators provide an excellent technological opportunity to replace conventional actuators due to their unique characteristics and ability to react directly to environmental stimuli; thus promoting the development of more advanced and cheaper actuators with a significant reduction in mechanical complexity and size [Jani, 2014]. In these cases the SMA actuator is both sensor and actuator. The temperature of the environment creates the triggering action and the dynamics of the actuator. Since thermal energy is directly converted into mechanical energy, the shape memory element can be classified as a thermal actuator [Humbeeck, 1999]. Thermal actuators are mostly employed as a part of electric appliances and automobile engineering: flaps in air conditioners, which change the direction of airflow depending upon the temperature of the air; drain systems for steam heaters in trains; outer vent control systems to avoid fuel evaporation in automobiles; and devices to open parallel hydraulic channels in automatic transmissions. Figure 1.29 shows the example of a thermostatic mixing valve, useful to understand how a thermal actuator works.

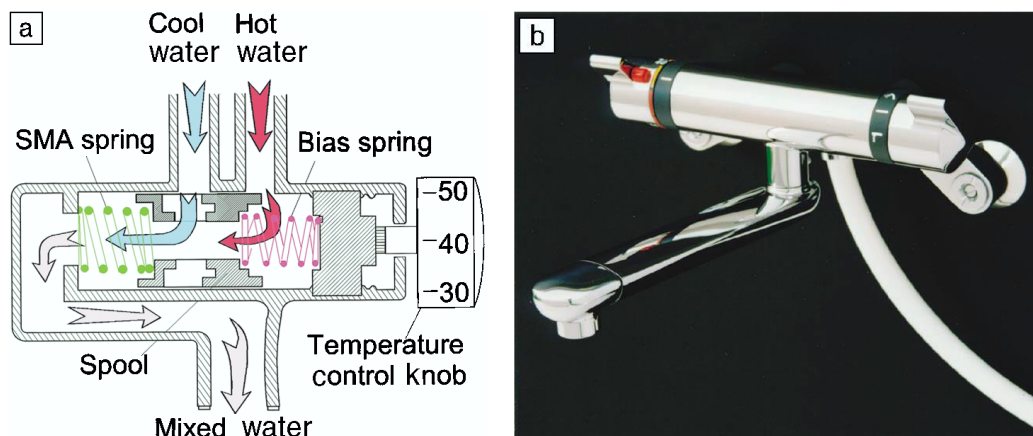


Figure 1.29 Application of shape-memory alloys to a thermostatic mixing valve: structure (a) and example of a commercially available valve (b) [Otsuka, 2002].

It has two basic components, a temperature-sensitive SMA spring and a temperature-insensitive bias spring, both of which are set in series and thus resist each other. Usually the SMA spring is harder than the bias spring in the parent phase (at higher temperatures) and softer than the bias spring in the martensitic state (at lower temperatures). Thus, when the temperature is too high, the SMA spring is stronger than the bias one, and the opening for hot water becomes smaller than that for cold water. When the temperature is too low, the opposite effect occurs [Otsuka, 2002].

1.5.2.3 Microactuators driven by electric current

In this application SMA components are purposely heated by means of electric current, and their sensing function is not used. Designers have shown a special interest in this type of applications, namely for robotic applications [Humbeeck, 1999]. One of the early applications in this area was a robot hand driven by SMA wires, similar in size to a human hand, with 13 degrees of freedom, visible in Figure 1.30 (a) [Hosoda, 1983].

Although there were several advantages offered by this application, the large current required to drive it and the difficulty of quickly cooling the SMA wires were serious drawbacks. More in general, SMAs are used to provide compact designs, light weight, soft and smooth motion, and three-dimensional movement. These characteristics should provide particular advantages in harsh environments, such as ocean water, space, nuclear and medical. One example is the 'walking' SMA robot capable of examining the seabed shown in Figure 1.30 (b). Externally, it is designed to imitate a crab, which appears to be the ideal configuration for movement on land and the sea floor. The use of SMA actuators in the robotic crab enables each of the joints to move as a real crab would. The 'muscles' of the robotic crab thus consist of SMA actuators heated electrically and cooled by the surrounding water itself [Furuya, 1991]. Other important applications are robotic medical equipment, such as the "active endoscope" with multiple degrees of freedom, which is driven by a SMA servo actuator.

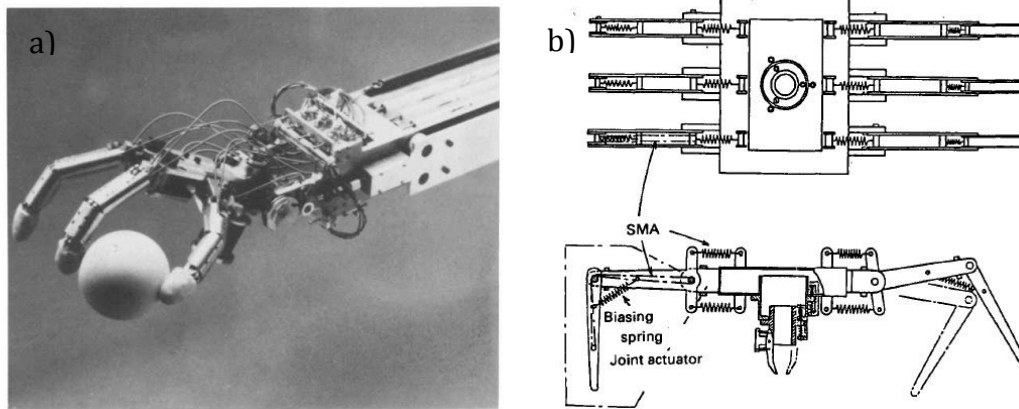


Figure 1.30 SMA robotic arm which resembles a human hand and can grasp a very delicate ball without damage (a) and basic scheme for the SMA undersea robot resembles a crab, with six legs, each with two joints (b) [Furuya, 1991].

This application generated several new research areas in micromachines, such as an active catheter and an inspection device for pipe systems. In such applications, SMA actuators have many advantages over other types of actuators such as wax actuators, magnetic solenoids, and bimetal actuators, including a large force-output/weight ratio, longer stroke and sharper shape recovery than actuators using bimetals, large flexibility in design, and environmental benefits. Among these, the first advantage is especially true when the mass is small, reason why SMA thin films are attracting attention [Otsuka, 2002].

1.5.2.4 Smart materials

One of the recent trends in materials science is research on smart materials. In this respect, SMAs are typical smart materials, since they involve three simultaneous functions: sensing, actuator and control [Humbeeck, 1999]. An important application in this respect is the development of hybrid composites, which include for example CFRPs (carbon-fiber-reinforced plastics) and Ti-Ni wires (or films). In these composites, Ti-Ni wires are expected to avoid the problems of fracture in CFRPs or debonding and transverse cracks between the CFRP. The research in this direction is focused on improving the reliability of aircraft and decreasing maintenance costs. Vibration control using a smart composite is another important target, since the elastic constant can be changed continuously through the

transformation temperature range [Otsuka, 2002]. Another envisaged application is the smart wing for aeroplanes. For similar reasons as in the helicopter rotor blades, the shape of the wing should be adaptive, depending for example on the actual speed of the plane, at the same time improving efficiency and noise reduction. An example of such a wing is shown in Figure 1.31 [Beauchamps, 1992].

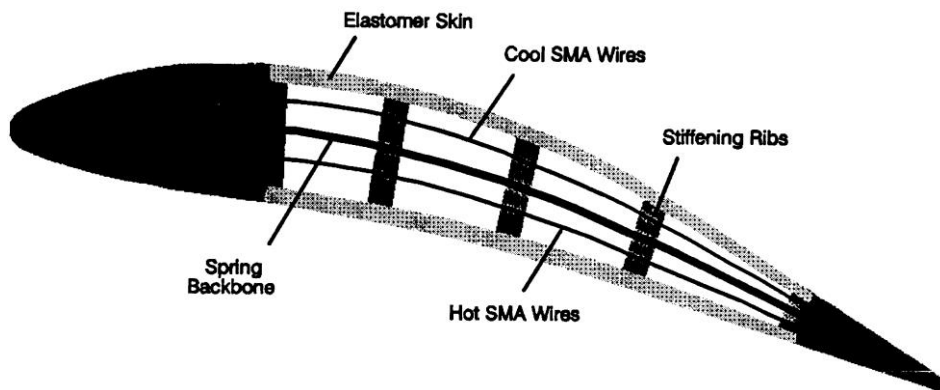


Figure 1.31 Shape memory alloy adjustable camber (SMAAC) control surface internal actuator concept [Beauchamps, 1992].

Again in the aerospace field, the adaptive serrated nozzle (ASN) is one of the most promising concepts to help reduce the noise level generated by aero-engines (Figure 1.32). The serrated nozzle is designed to protrude into the air stream causing mixing between the hot air stream and ambient air at the nozzle exit reducing the noise level. Adaptive control system using shape memory alloy (SMA) actuators deploy the protrusion only when noise abatement is required required in order to maximise fuel efficiency [Herkes, 2006].



Figure 1.32 Adaptive serrated nozzle (ASN) for Quiet Technology Demonstrator 2 project developed by Boeing, NASA, General Electric and Goodrich Corporation [Herkes, 2006].

1.5.2.5 Dampers for structures control

SMAs are also important as high-damping materials, since twin boundary movements in martensites contribute greatly to internal friction [Otsuka, 2002]. Smart systems for civil structures are described as systems that can automatically adjust structural characteristics in response to external disturbances and/or unexpected severe loading toward structural safety, extension of the structure's life time, and serviceability. When integrated with civil structures, SMAs can be mainly passive or semi-active components to reduce damage caused by environmental impacts or earthquakes. In the passive control system, no external power source is required and the impact forces are developed in response to the motion of the structures [Song, 2006]. An important application exploiting passive control are SMA ground isolation devices, such as base isolation system with superelastic SMA bars for elevated highway bridges [Wilde, 2000] and the Nitinol-wire-based isolation system for vibration isolation of buildings [Dolce, 2001], schematically shown in Figure 1.33 (a) and (b) respectively. SMA isolators provide variable stiffness to the structure according to the

excitation levels, in addition to energy dissipation and restoration after unloading, therefore, superelastic SMAs are appropriate.

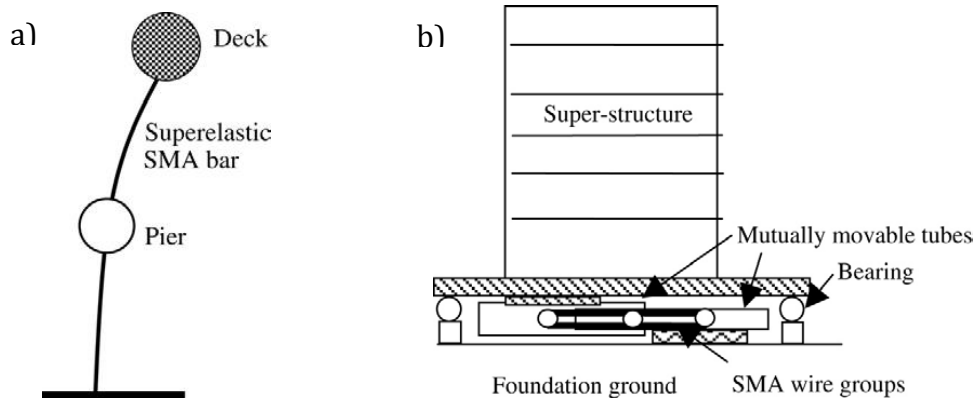


Figure 1.33 Schematic of the SMA isolation device for elevated highway bridges (a) and of the SMA isolation system for buildings (b) [Song, 2006].

The energy dissipation is another mechanism based on the damping capacity of SMA and is used for system which use SMA elements integrated into structures to absorb vibration energy. SMA energy dissipation devices have been seen in the forms of braces for framed structures (see Figure 1.34 (a)), dampers for cable-stayed bridges (see Figure 1.34 (b)) or simply supported bridges, connection elements for columns and retrofitting devices for historic buildings (see Figure 1.34 (c)) [Song, 2006].

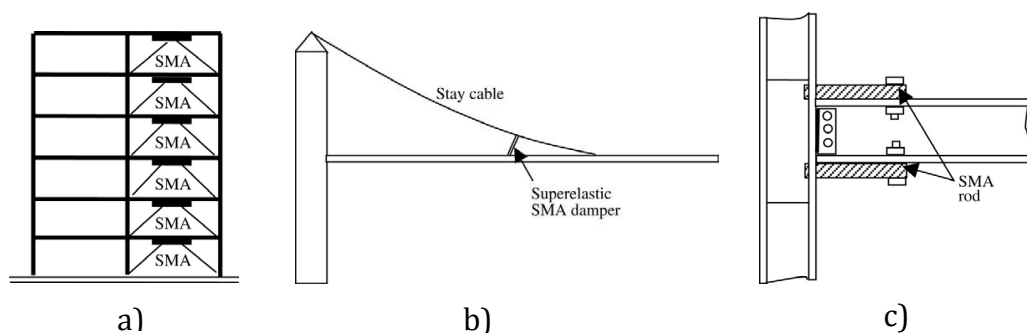


Figure 1.34 Schematic of the setup of the SMA brace reinforced frame structure (a) of a SMA damper for a stay-cable bridge (b) and of SMA connector for steel structures (c) [Song, 2006].

There is also a large military interest for shock wave absorption in armor material but also in other bullet proof materials, since the high strain amplitude in combination with a single impact allows the optimal conditions of SMA for high damping properties [Humbeeck, 1999].

1.5.3 Other applications

Some of the most successful applications, especially concerning the amount of sold single products, were created in the area of Fashion, decoration and gadgets. Examples are eyeglass frames (see Figure 1.35) and antennas for portable cellular telephones, parts which are regularly subjected to involuntary impacts, also of great entity.

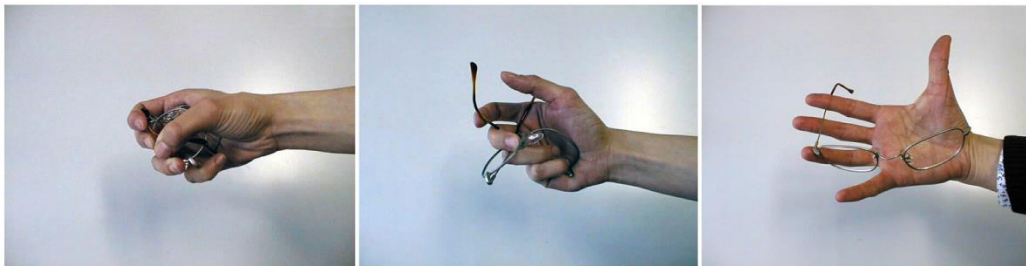


Figure 1.35 Superelastic Nitinol eyeglass frame [materialdesign.it].

These items realize their goals and comfort by using the pseudo-elastic behaviour. The important combination of stiffness and super-elasticity was the key to success. Ni-Ti SMA are also applied in clothing parts, as the use of a super-elastic wire as the core wire of a wedding dress petticoat, which can be folded into a compact size for storage and transport, and the application of shape memory and super-elasticity in shoes. Those shoes accommodate SMA inserts along the mouth and near the counter: when heated above the shape recovery temperature, the insert promptly relieves deformations that have taken place in the use of the shoes [Humbeeck, 1999]. An elegant application is the lamp reported in Figure 1.36, where a shape memory spring heated by an electric light opens the lamp shade. This simple mechanism creates a transformation of the lamp shade shape depending on whether the light is on or off [Brownell, 2008].

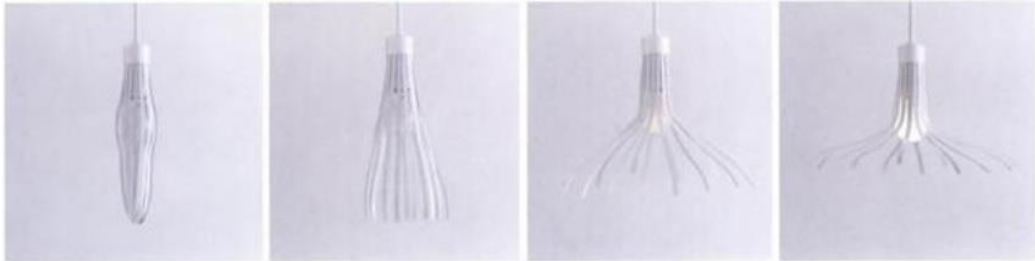


Figure 1.36 Shape transforming lamp shade designed by Oki Sato [Brownell, 2008].

SMAs that change shape near body temperature are being used to make shape-changing jewelry that transforms throughout the day [Otsuka, 2002]. Moreover, Nitinol components can be employed for everyday applications, such as coffeemakers, rice cookers, headphones and golf clubs. The SME is also utilized in shower faucet designs where a SMA spring automatically adjust the flow of hot and cold water to maintain a preset water temperature [Kumar, 2008]. Finally, it is interesting to notice that also artists see SMA as an original tool in dynamic sculptures. Indeed, several sculptures have been designed and exposed in public or private domains. Apart from those few examples, many other types of ‘gadgets’ have appeared, but generally with a limited time on the market [Humbbeck, 1999].

CHAPTER 2:

2 Heat treatment of SMAs

By changing composition, mechanical working, and applying heat treatment the technical properties of NiTi shape memory alloys can be modified to a great extent to suit the specific application. One of the biggest challenges in using this family of alloys is in developing the proper processing procedures to yield the properties desired [Hodgson, 1990]. The main technologies used up to now to the annealing treatment of Nitinol SMAs are presented in this section, starting from the conventional furnace annealing, more common and well examined, to some newest and less tested techniques.

2.1 Conventional annealing

2.1.1 Cold work and annealing

Traditionally, the annealing treatment needed to impose the properties of shape memory and superelasticity to the alloy, is conducted in furnace on the previously cold worked material. Varying the initial conditions of strain hardening of the material and the heat treatment parameters, such as temperature, time and cooling medium, it is possible to tailor the characteristic parameters that describe the behavior of the SMA alloys so to make them suitable for the specific application [Petrini, 2011]. Researchers have conducted several studies which investigate the effect of the material plastic deformation and the subsequent heat treatment on the final properties of the material, including the maximum recovering strain, the characteristic temperatures relative to the martensitic transformation, the hysteresis properties and the fatigue life.

Miller e Lagoudas studied the influence of the cold work percentage imposed to the material and of the heat treatment temperature on the shape memory effect and on the plastic strain development of equiatomic

NiTi SMA. Samples of fully annealed SMA wires were subjected to a cold rolling process with different percentages of thickness reduction and subsequently furnace annealed at various temperature levels from 300 to 500°C for a fixed time of 15 minutes.

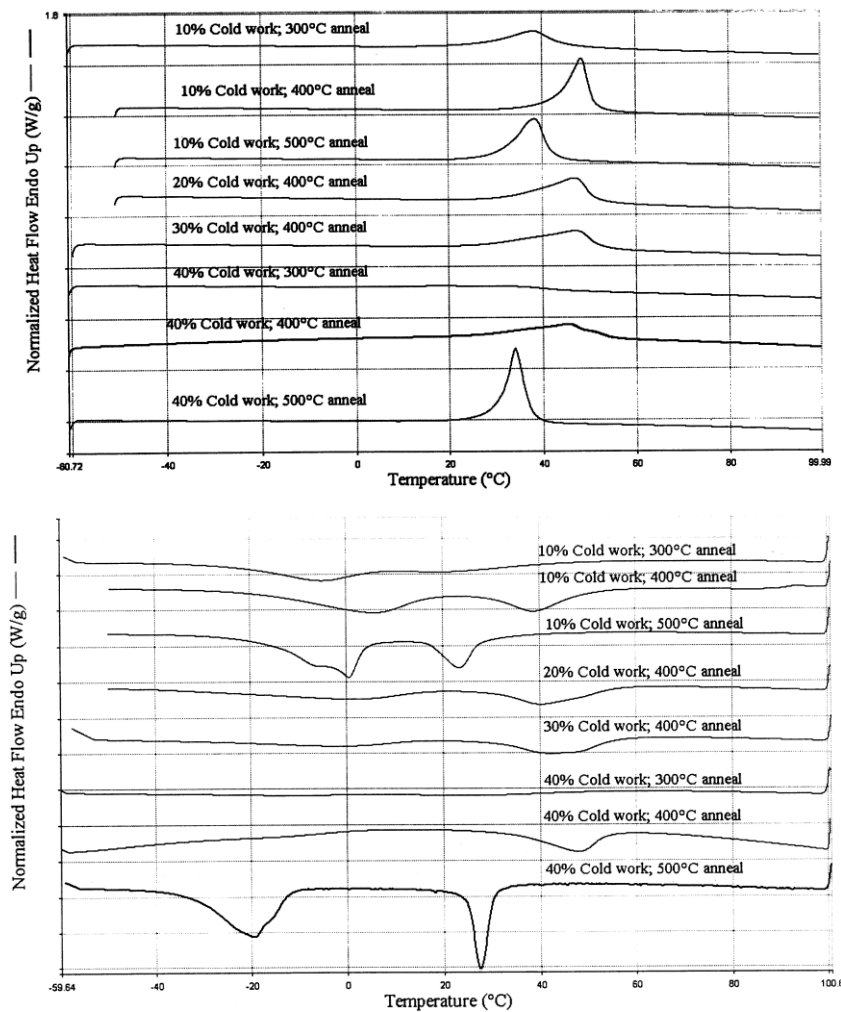


Figure 2.1 DSC cooling and heating curves of NiTi specimens showing the R-phase development and the variation of transformation temperatures for various levels of cold work and heat treatment during the austenitic to martensitic phase transformation [Miller, 2001].

The materials obtained in the analyzed process conditions were characterized in terms of thermally-induced phase transformation through subsequent thermal cycles at different levels of constant stress. The strong

sensitivity of the calorimetric response of the material to the annealing time and temperature is well visible in Figure 2.1, while in Figure 2.2 the latent heat of transformation is presented for every condition. It is easy to observe that the heat of transformation increases with the increase of the annealing temperature and with a decrease of the cold working percentage. Results show also that the maximum transformation strain is not dependent on the cold work percentage and on the annealing temperature, while an increase of strain hardening, being equal the annealing temperature, cause an increment in the stress level for the onset of plastic strain and a decrease of the additional plastic strain development. In addition, a decrease in the annealing temperature, being equal the cold work percentage, increases the stress level for the onset of plastic strain and decreases the additional development of plastic strain [Miller, 2001].

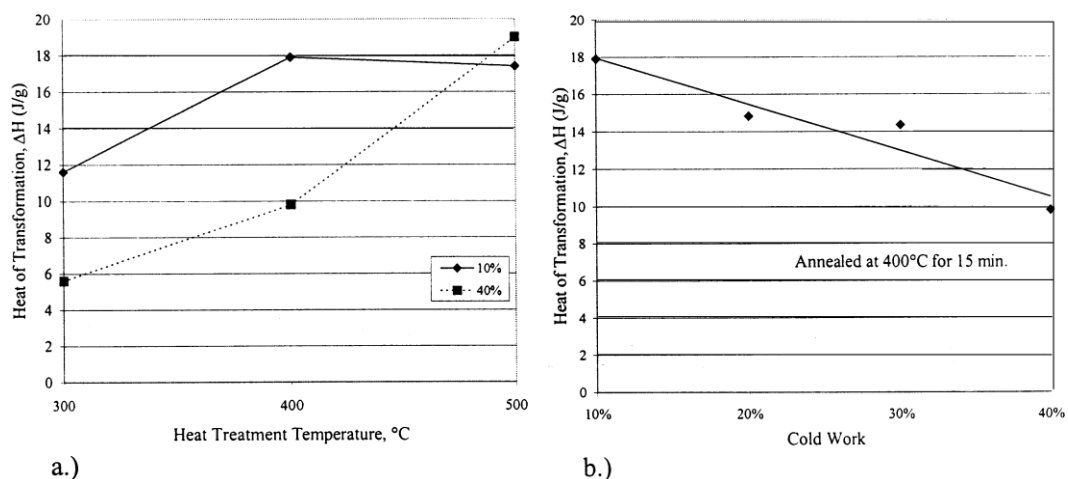


Figure 2.2 Effect of (a) annealing temperature and (b) cold work on latent heat of transformation for NiTi specimens [Miller, 2001].

Huang and Liu have performed heat treatments on NiTi wires at various temperatures in the range between 300 and 700°C for 30 minutes. In this case, the cooling was obtained in air at ambient temperature. From the DSC curves for every temperature level of the treatment (see Figure 2.3) an increase of M_s and A_f temperatures for the samples treated at the intermediate temperatures can be noticed. In Figure 2.4, the evolution of

the characteristic temperatures for the examined conditions is shown [Huang, 2001].

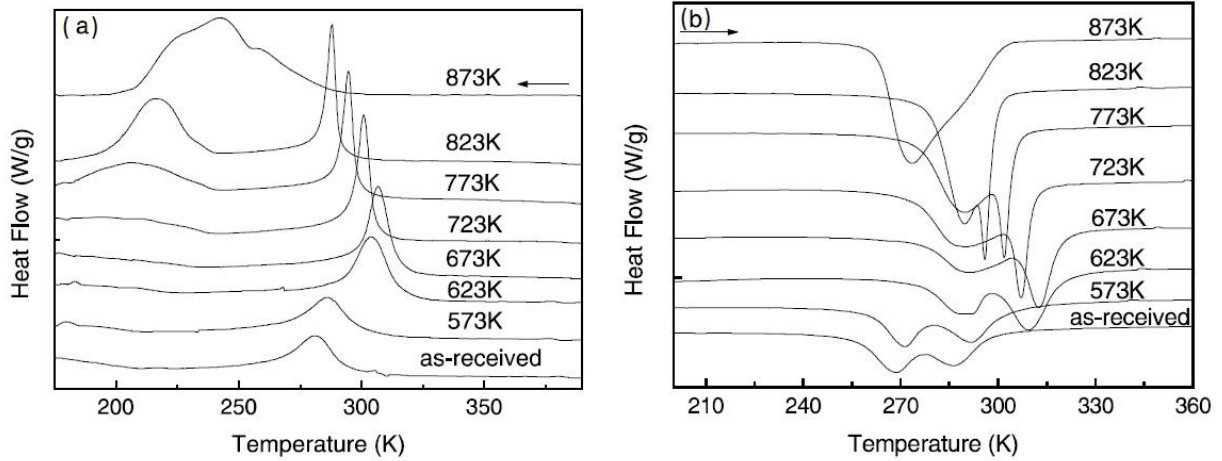


Figure 2.3 DSC curves for the material treated at different temperatures and in the cold worked condition (as-received) [Huang, 2001].

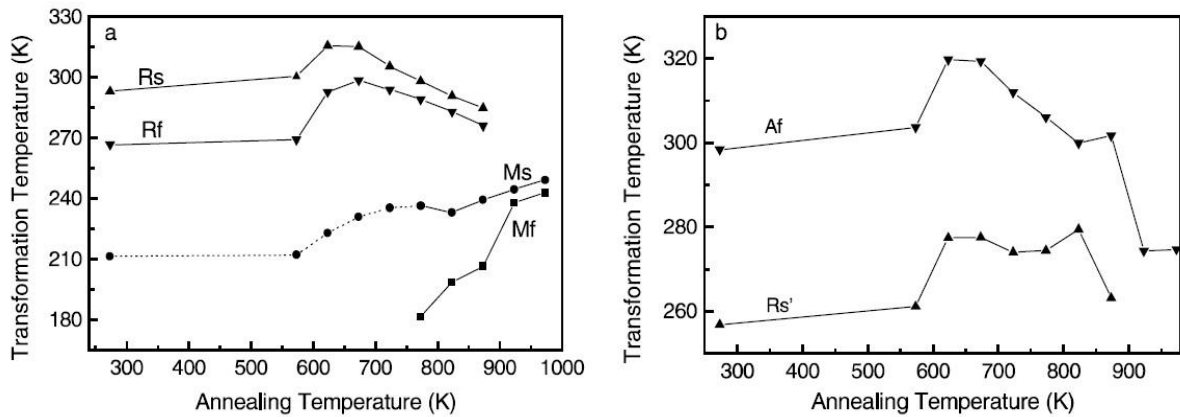


Figure 2.4 Transformation temperatures of the alloy as a function of the annealing temperature [Huang, 2001].

Myara et al. studied more in detail the influence of the annealing temperature on the mechanical properties of Ni-Ti alloys used for the fabrication of endodontic instruments. Again, samples were heated for a fixed time at different temperatures, but in this case quenched in iced

water. The characterization was carried out through calorimetric analysis, bending tests and fatigue tests. The results of the calorimetric analysis show trends for the transformation temperatures and peaks variation in accordance with the results found by Huang et al. [Huang, 2001]. In Figure 2.5 the curves load-deflection are presented for the analyzed conditions. The ratio between load and deflection in the first elastic part of the curve, which is the elastic modulus of the material, is lower for the intermediate temperatures because of the phases present in the material at the test temperature. At the maximum annealing temperature the recrystallization of the material takes place, so a small residual deformation is found after the unloading phase. For what concerns the fatigue behavior, it was observed a higher number of cycles to fracture for the specimens treated at the intermediate temperatures with respect to the others. This result introduces the possibility of a proportional relation between the material flexibility and the fatigue properties [Myara, 2014].

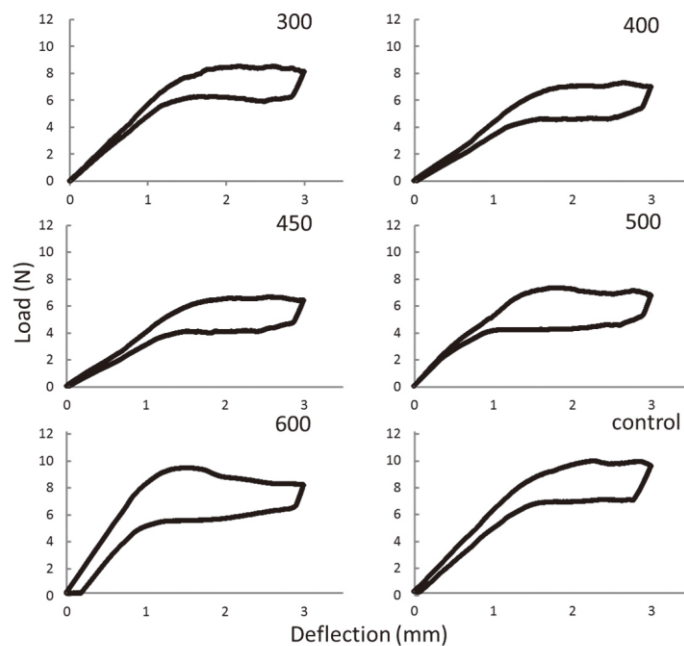


Figure 2.5 Load-deflection curves for the material treated at different temperatures and in the cold worked condition (control) [Myara, 2014].

2.1.2 Shape setting

One of the most critical aspects of Nitinol component manufacturing is the *shape setting* phase. The use of superelastic or shape memory NiTi elements for a specific application usually requires the setting of a custom shape in a piece of Nitinol. The *shape setting* is attained constraining the Nitinol element around a metallic mandrel or fixing the element in the desired shape and carried out a suitable heat treatment, similar for both cases of Nitinol shape memory or superelastic. The most common and exploited shape of Nitinol is straight, obtained through a straight annealing treatment, but a wide variety of geometries can be created [Smith, 2014]. Tooling fixtures examples for the shape setting of wires are shown in Figure 2.6. In the case of pin and plate fixture the wire is clamped at one end and subsequently wrapped around the pegs to create the desired geometry.

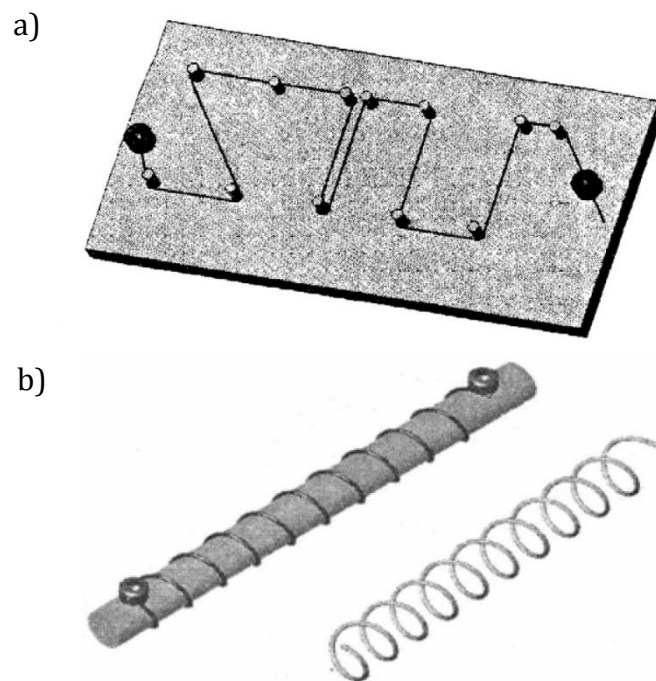


Figure 2.6 A pin and plate shape-setting holding fixture (a) and a cylindrical mandrel to create helical springs (b) [Smith, 2014].

The end is then clamped off to hold the wire in place during heat treatment. The tooling is often made of stainless steel to facilitate repeated use without significant oxide build up [Morgan, 2004]. Also in the case of mandrels, the wire is fixed and wrapped around a cylinder of the desired diameter to provide the final shape of the element [Smith, 2014].

For the shape setting a thermo-mechanical treatment is performed after the cold working: it means to apply a stress to the alloy during the annealing imposing a certain shape. The SMA performances are consequently modified. In this case the heat treatment parameters are chosen to set both the shape and the properties of the part, and usually need to be determined experimentally for each desired part's requirements. Generally, rapid cooling of the form is preferred, via a water quench or rapid air cool for small parts with small fixtures.

2.1.3 Cycling

Eventually, a last step of thermal or deformation cycling is added to further investigate the material behavior and stabilize its properties. As shown in Figure 2.7 (a) from the research of Miyazaki et al. [Miyazaki, 1986], with thermal cycling under no load, M_s and M_f temperatures decrease with increasing number of cycles (N), while R_s is not affected. Also M_s and M_f stabilize after a certain amount of cycles. In this study it is concluded that the shift of the transformation temperatures with thermal cycling is due to the introduction of dislocations. Transmission electron microscopy (see Figure 2.7 (b)) revealed that dislocations were introduced by thermal cycling in the solution-treated specimens and their density increased with increasing number of thermal cycles.

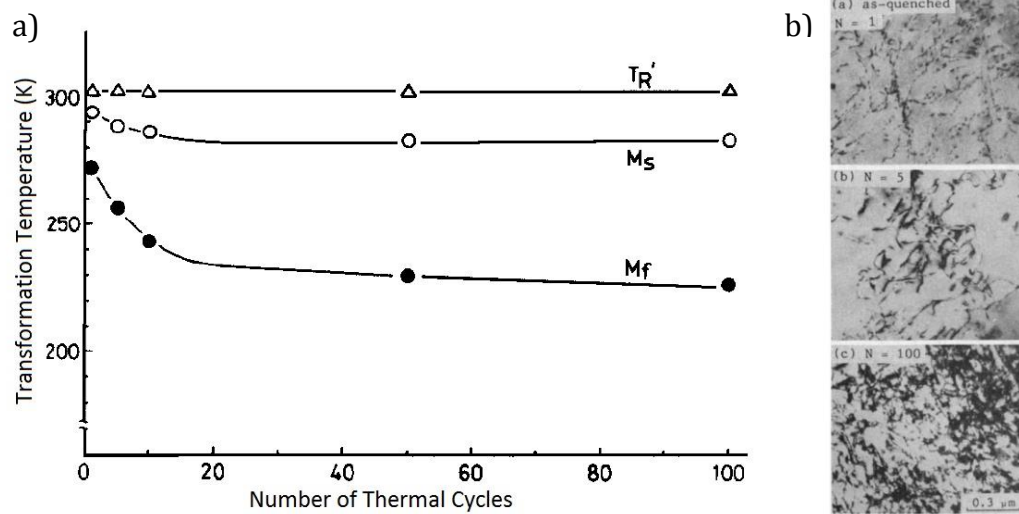


Figure 2.7 Transformation temperatures plotted against number of thermal cycles (a) and change in internal structure due to thermal cycling, where N indicates the number of thermal cycles (b) [Miyazaki, 1986].

Another fundamental aspect that can restrict the alloy applicability is the amount of increasing permanent deformation after repeated phase transformations. Therefore, thermal cycling tests under constant load were carried out by Zimmermann et al [Zimmermann, 1997] and the irreversible strain is measured as a function of the number of cycles and of the tensile stress. Figure 2.8 shows the permanent strain as a function of the number of thermal cycles at different tensile stresses. At the higher stresses, the highest strain per cycle was found after the first cycle, while at lower stresses there was no permanent strain measured after the first two cycles. After more than 20 cycles the permanent strain at all stress levels increased nearly linearly with the number of cycles. The trends found in this investigation are consistent with experimental results published in previous researches of Stachowiak and McCormick, shown in Figure 2.9 [Stachowiak, 1988].

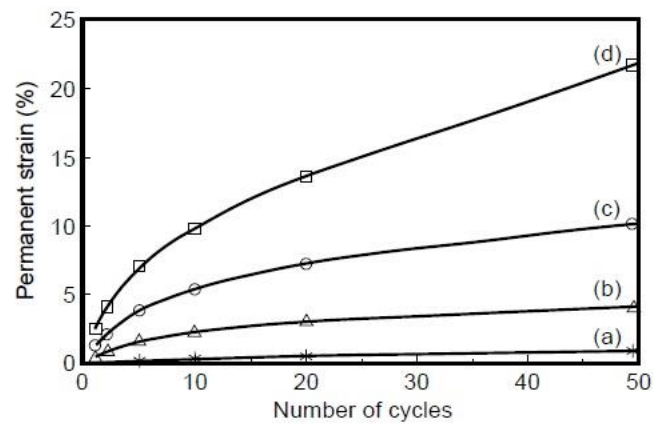


Figure 2.8 Permanent strain as a function of the number of thermal cycles at different tensile stresses: 135, 270, 405 and 540 MPa [Zimmermann, 1997].

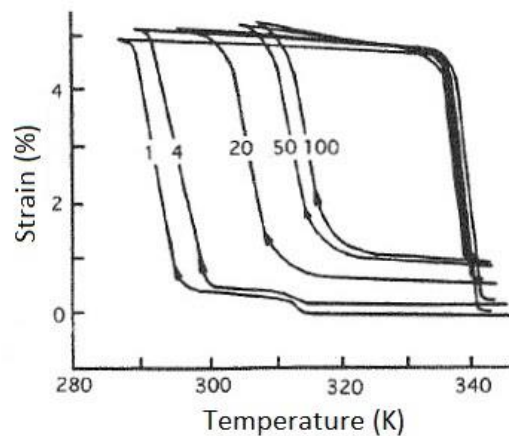


Figure 2.9 Influence of repeated thermal cycling with applied 200 MPa [Stachowiak, 1988].

Deformation cycling above A_f changes gradually the shape of the pseudoelasticity loop in the stress-strain curve, as seen in Figure 2.10. This change is significant in early cycles, but it becomes very little after 100 cycles, so it is suggested to train the material prior to actual service for stabilizing the pseudoelasticity [Otsuka, 1999].

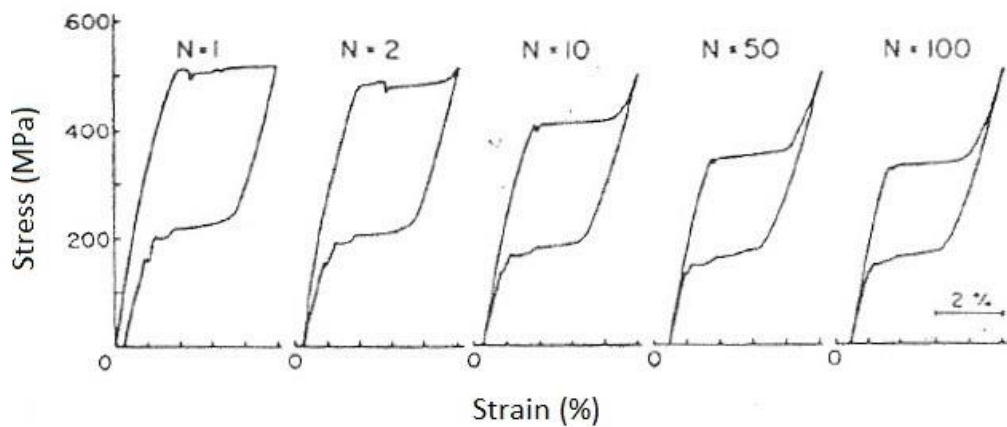


Figure 2.10 Effect of cyclic deformation on stress-strain curves of a Ni-Ti alloy thermos-mechanically treated [Otsuka, 1999].

2.2 Unconventional annealing

The annealing treatment, conventionally performed in furnace, can be conducted also with non-conventional techniques, such as laser annealing. The treatment takes place on cold worked materials and the process parameters, as long as the resulting properties, can be slightly different from the conventional ones.

Also the sequential or simultaneous action of plastic deformation and electric current in different alloys, including shape memory TiNi alloys, leads to a number of interesting phenomena. In the first case, the conventional post-deformation annealing for stress relaxation or recrystallization is substituted by electro-pulse treatment (EPT), while in the second case the cold working process is conducted in an innovative way by the use of electric current with electro-plastic deformation (EPD), showing improved characteristics of the alloy.

2.2.1 Laser annealing

First experimentation of laser annealing can be found in the researches of Bellouard et al., which use laser technology to locally crystallise amorphous thin film and re-crystallise cold-worked sheet of SMA material. The basic

idea is to integrate different mechanical behaviors within one single piece of material, allow the fabrication of monolithic micro-devices [Bellouard, 2001].

Similar studies on amorphous films are conducted by Wang et al., focusing on microstructural observations of the annealing area as a function of the laser beam power density and the scan speed (Figure 2.11). After crystallization, the annealed area undergo homogeneous nucleation with random crystallographic textures leading to a uniform microstructure [Wang, 2005].

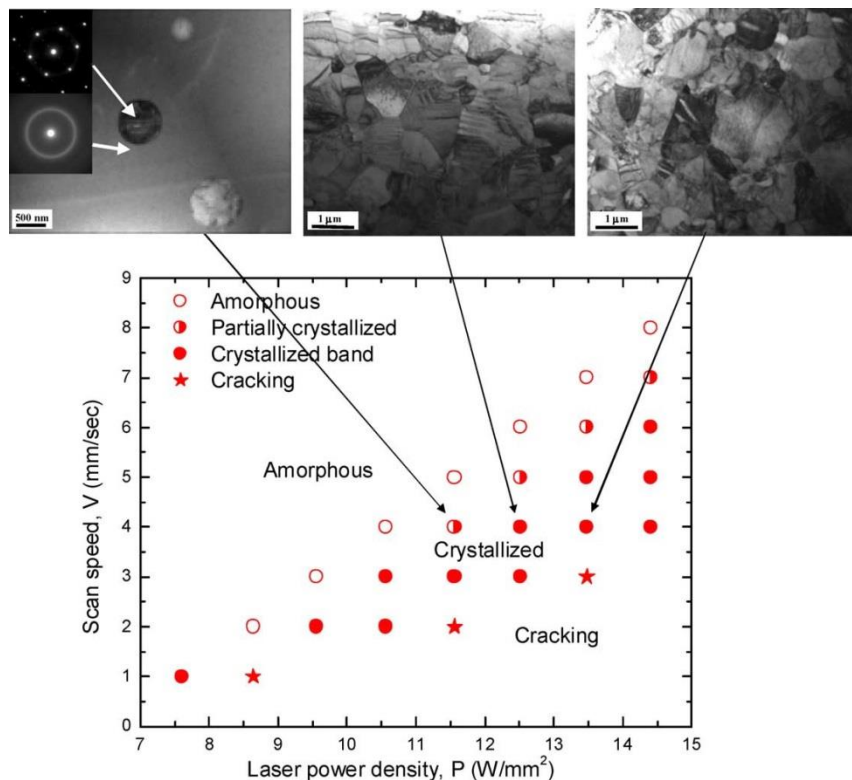


Figure 2.11 Crystallization behavior of NiTi films as a function of laser power density and scan speed based on optical (not shown) and TEM observations [Wang, 2005].

Meng et al. investigate how a two-dimensional gradient of different functional properties can be realized inducing the fusion on the top surface of Nitinol plates by means of laser surface annealing. Owing to the natural degradation of heat penetrating into the material, a temperature gradient

within the thickness is created by laser surface interaction and heat conduction. In this way, a gradient of functional properties is obtained from the surface, where a thin layer of material is melted, down to the core of the alloy, where the material does experience the heating with decreasing temperatures. The plates exhibit a progressive shape recovery through their thickness, resulting in a “stingray-like” motion when activated by heating after a uniaxial tensile deformation. The activating temperature interval and the corresponding activated curvature interval may be customized by controlling the processing parameters, including the level of cold work, the thickness of the plate and the laser power [Meng, 2011]. The microstructural variation through the thickness was characterized by hardness measurement and layered differential scanning calorimetry analysis. The microstructural gradient led to a unique shape memory effect, involving shape change in two opposite directions upon one heating, analogous to stingray motion. The expected temperature profile and the measured hardness through the thickness of the NiTi plate are shown in Figure 2.12 [Meng, 2012].

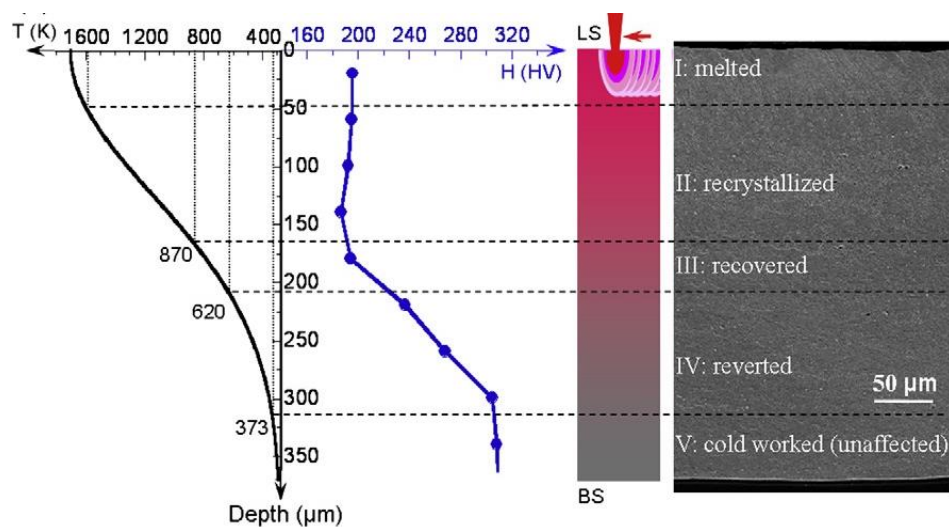


Figure 2.12 Temperature distribution, hardness profile and microstructural gradient through the thickness of laser annealed thin NiTi plate [Meng, 2012].

Previous investigators regarded continuous-wave (CW) laser treatment of the Nitinol samples, while less information is available in the literature

about pulsed-wave (PW) laser treatment of NiTi. Sadrnezhaad et al. investigation is devoted to the pulsed-laser heat treatment as an alternative method for creation of local shape-memory crystals embedded in amorphous NiTi thin layers. Scanning electron microscopy, X-ray diffraction and atomic force microscopy were performed to characterize the microstructure and surface morphology of the spot patterns. In spite of the nearly same spot diameter, the ablation effect of the laser beam increases with the heat input at high laser power. Some spots are also darker than others due to greater oxidation at higher temperature, which occurs at the higher power densities of the laser beam and can cause a deviation from equi-atomic composition with the formation of a Ni-rich layer underneath the titanium oxide film. This technique finds application in the development of micro-electro-mechanical (MEMs) devices and may reduce both the undesirable surface oxidation and the time of operation, inducing a faster actuation response [Sadrnezhaad, 2009]. Similar experiments are conducted by means of a nanosecond laser, highlighting that increasing beam intensity and laser pulse-number promoted amorphous to *R*-phase transition, while lowering duration of the pulse incidence reduced local film oxidation and film/substrate interference. This paper shows that the nanosecond pulse laser annealing of amorphous NiTi films result in the stabilization of the rhombohedral structure, which gives desirable functional behavior to the alloy, as well as a further reduction of treatment time [Sadrnezhaad, 2012].

Concerning laser annealing on Nitinol wires, Biffi et al. adopted a fiber laser for imposing a thermal cycle to a quasi-equiatomically NiTi SMA thin wire for promoting the SME. As depicted in the schematic of Figure 2.13, a scanning of the laser beam, emitted in CW and defocused on the top surface of the wire, is used to induce the MT, which is directly correlated to the SME. The wire is constrained along a line to guarantee both constant beam size incident. The process is realized by a single laser scan on cold worked material. The effect of the incident laser power was studied on the evolution of the functional properties of the wire. It is found that a fast shape setting, performed by using a laser beam, can induce uniform and promising performances of the wires, comparable to the ones of the commercial wire. The calorimetric properties of the wire can be changed by means of the power variation; furthermore, the thermo-mechanical

response of the laser treated wire shows a strain rate upon temperature changing higher than the one of the conventionally treated wire (see Figure 2.14). Possible explanation of this capabilities could be associated to the rapidity of the laser thermal cycle with respect to time required to induce the MT in a furnace indicated by the literature. In this case, the grain growth at high temperature can be significantly limited, because of the high velocity of the beam during the treatment [Biffi, 2014].

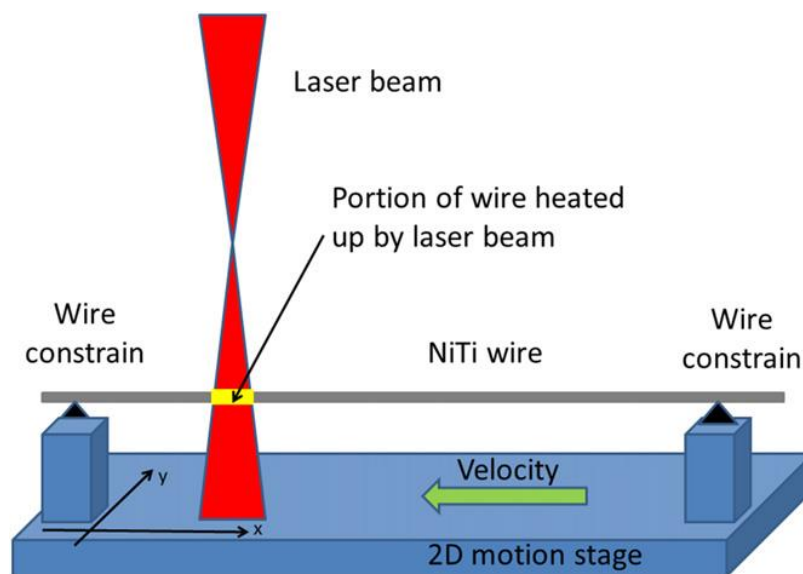


Figure 2.13 Schematic of the laser shape setting process on NiTi SMA wire [Biffi, 2016].

Regarding tensile test, the stress-strain response for the laser annealed wire is found to be very similar to commercial straight annealed wire in terms of plateau stress and strain and recoverable strain after unloading, as depicted in Figure 2.15. The mechanical hysteresis appears instead narrower in the laser treated wire than in the conventionally annealed one [Biffi, 2016].

In the study of Daly et al., a NiTi microgripper capable of self-positioning was fabricated through the application of laser processing with multiple memory material (MMM) technology to locally tune the thermomechanical response of NiTiInol wires.

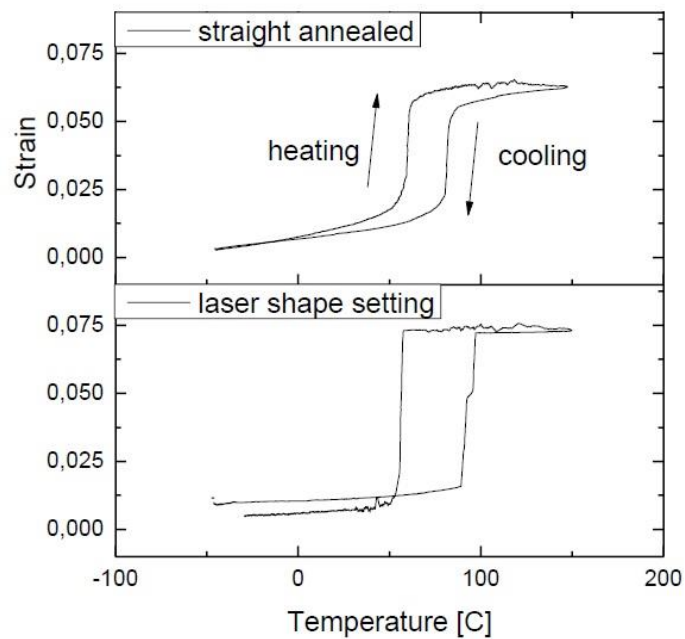


Figure 2.14 Thermo-mechanical response of the wires: straight annealed and laser shape setted [Biffi, 2014].

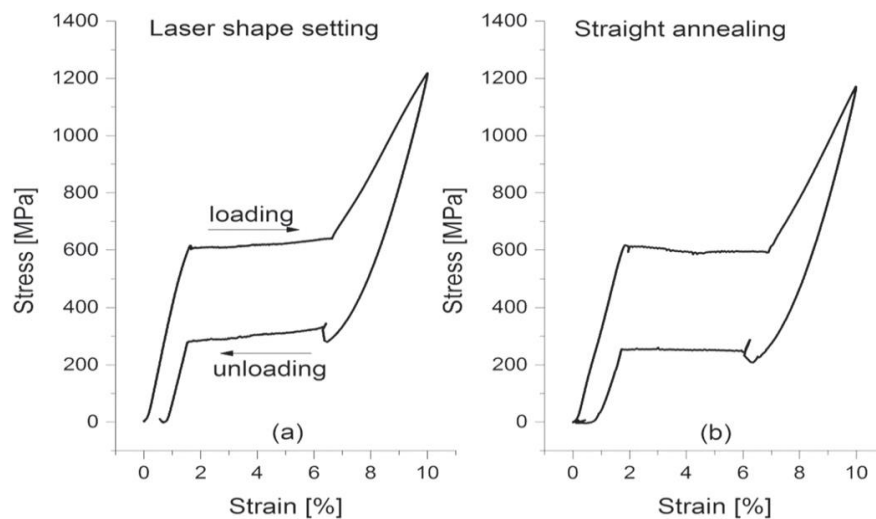


Figure 2.15 Stress–strain curves of SE NiTi wires at 25 °C: laser shape setting (a) commercial straight annealing (b) [Biffi, 2016].

The purpose of this study is to implement laser processing to fabricate a novel NiTi-based microsystems device with enhanced thermomechanical

functionality and eliminates the need for external positioning systems, greatly reducing the complexity of the NiTi microsystems device. Three independent material domains were locally embedded as the active components of the microgripper. The two lower temperature domains were utilized as the self-positioning microgripper segments, while the higher temperature domain actuated the microgripper head. Mechanical testing revealed three separate thermomechanical behaviors in the laser-processed microgripper, which corresponded to the independent shape memory recoveries of each embedded material characteristic, as reported in Figure 2.16 [Daly, 2012].

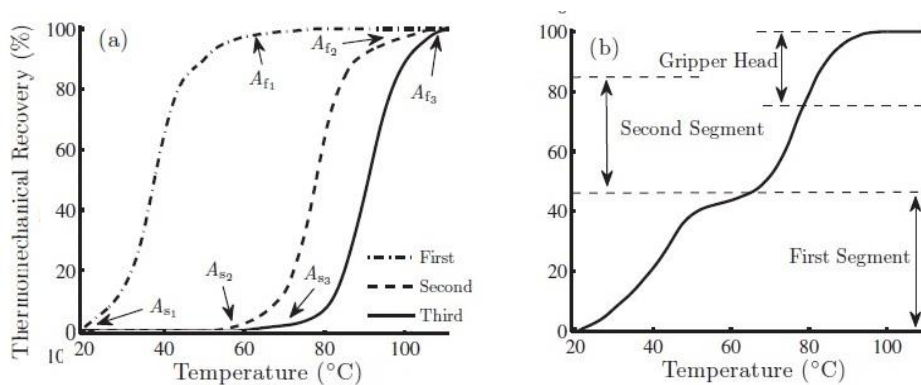


Figure 2.16 (a) Thermomechanical recovery of each microgripper component and (b) the combined recovery of the laser-processed NiTi microgripper [Daly, 2012].

2.2.2 Electropulse treatment (EPT)

An example of unconventional shape setting is the electropulse method, where current sparks can quickly heat up the wire by Joule effect and consequently a fast annealing can be induced in the alloy. Good functional properties can be induced, because the rapid thermal treatment can limit the grain size [Malard, 2011].

In the study of Delobelle et al., heat treatments of cold worked Nitinol SMA wires are performed with milliseconds electropulse. Investigation of the transformation and mechanical behaviour of the heat treated part of the wires is realised. The experimental set-up used for the heat treatment of

the wires is shown in Figure 2.17. It is demonstrated that milliseconds electropulses allow to realise homogeneous heat treatments and to adapt the mechanical behaviour of NiTi wires by controlling the electric energy. The material can be made elastic with different elastic modulus (see Figure 2.18 (a)), perfectly superelastic with different stress plateau levels (see Figure 2.18 (b)) and superelastic with important local residual strain. Due to the short duration and high temperature of the heat treatment, this technique allows to obtain mechanical properties that cannot be obtained with classical heat treatments of several minutes in conventional furnaces, such as linear evolution of the final loading and high tensile strength or increase of the stress plateau level with cycling for superelastic material [Delobelle, 2016].

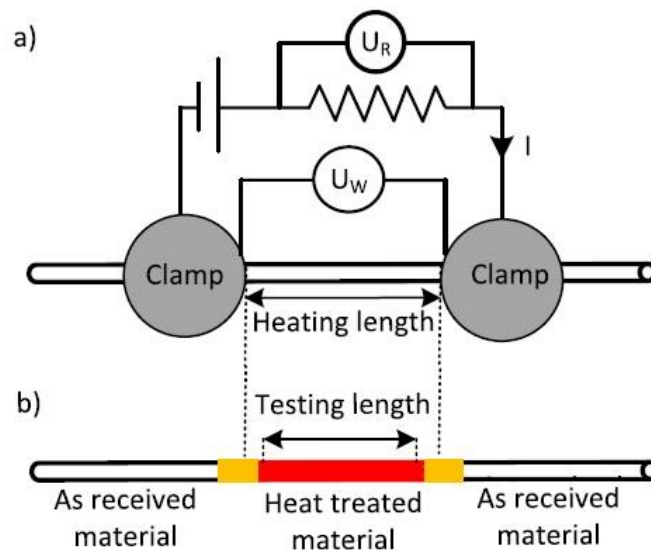


Figure 2.17 (a) Experimental set-up presentation. (b) Resulting material with local heat treatment [Delobelle, 2016].

Zhu et al. treated cold-rolled TiNi alloy by electropulsing with different process parameters and investigated superelasticity, electrical resistivity and microstructure evolution of the material. The recrystallization is found to happen in the cold-rolled TiNi alloys during electropulsing treatment (EPT) processing and it took few seconds to be completed. The short recrystallization time of the alloy is attributed to the acceleration of atomic diffusion and the movement velocity of the grain boundary by

electropulsing. In addition, the grain size increases with the charge voltage and the discharge frequency of the electropulse. The maximum superelasticity is gained when the TiNi alloy is treated by the electropulsing with the frequency of 300 Hz [Zhu, 2013].

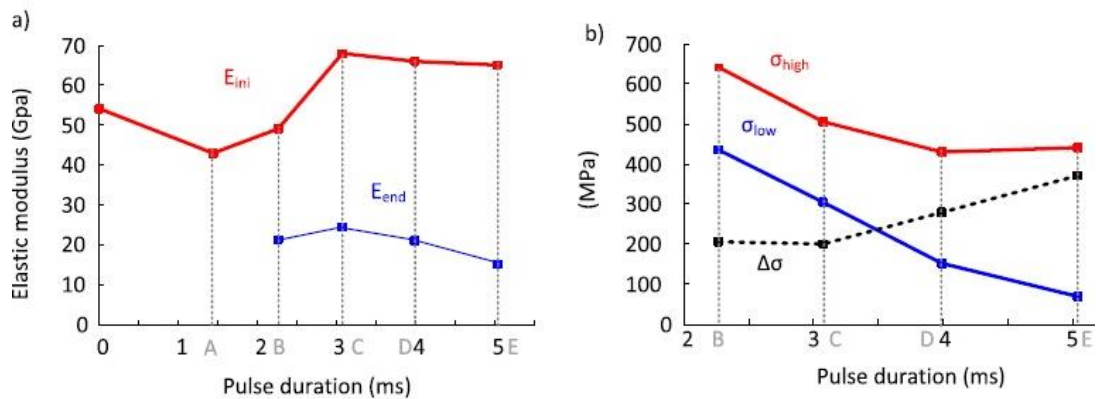


Figure 2.18 (a) Elastic moduli in function of pulse duration. (b) Plateau stresses at loading, unloading and hysteresis in function of pulse duration [Delobelle, 2016].

In Casati et al. research, high-power rapid current square pulses were applied to thin cold-drawn NiTi wires. To perform the treatments, specimens of the wire were vertically positioned, constrained in the apparatus by fixing clamps and subjected to double current pulse. However, the energy supplied to the wire induced a strong modification of the grain structure as shown by the TEM micrographs. Before the heat treatment, the strongly deformed microstructure of the wire featured an ultrafine grain size, with preferred orientation along wire drawing direction. The shape setting treatment induces the recrystallization of the cold-worked microstructure, resulting in equiaxed grains. In addition, dislocation structures are fully annealed out. Rapid current pulse treatment in Ti-rich NiTi induces shape memory effect with reduced thermal hysteresis and high recovery strain values. This novel treatment might replace conventional pre-device shape setting/training of the wire with a post-device shape setting with promising industrial advantages [Casati, 2014].

An application of this process is the continuous electropulse annealing system developed by Pilch et al. and presented in Figure 2.19. The NiTi wire is heat treated during re-spoiling while passing over two electrodes.

Electric power, wire speed and wire tension are key process parameters [Pilch, 2010].

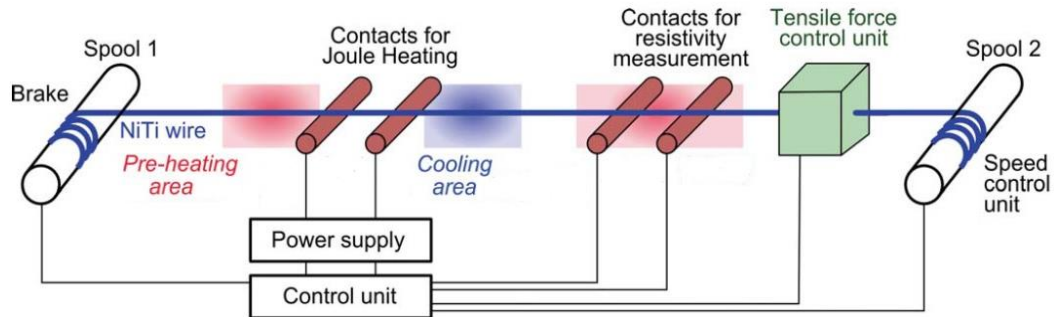


Figure 2.19 Schema of the equipment used for the treatment of continuous thin NiTi filaments [Pilch, 2010].

The length of the NiTi wire being annealed could be unlimited due to the continuity of the annealing process. The shape of the high temperature phase, austenite, could be set into straight form simultaneously. NiTi SMA wire continuous electropulse annealing is faster and easier when compared with the traditional furnace annealing, because almost instant heating could be achieved. Besides, the oxidation at high temperature annealing could be lowered, so material loss due to oxidation could be minimized. This is important especially for thin NiTi wire which had a very fast oxidation rate at high temperature due to the large surface area to volume ratio [Kin, 2006].

2.2.3 Electroplastic deformation (EPD)

Electro-plastic deformation (EPD) is a new process technology, which combines rolling and high energy density electropulse to increase the deformability of materials. It is particularly suitable for TiNi alloys, which are very brittle and hard to work at room temperature. The schematic of the process is presented in Figure 2.20, where the big rollers are cathode and the small ones anode. The rollers are connected to an electropulse generator which provide electropulses conducted by the metal.

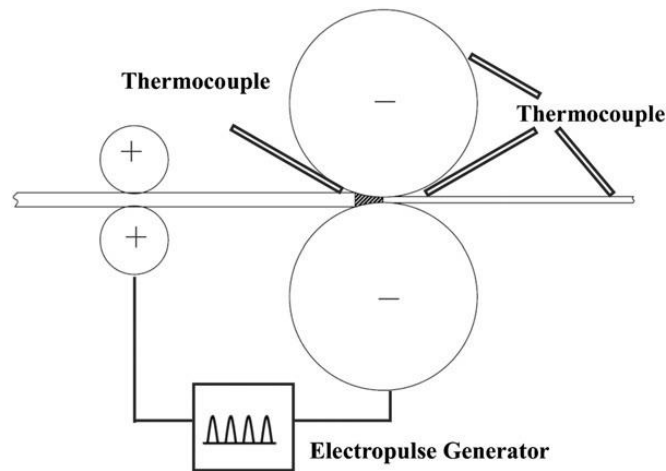


Figure 2.20 Schematic view of electroplastic rolling process [Zhu, 2013].

In Zhu et al. research, electroplastic rolling is used to process NiTi strips and investigate deformability, superelasticity and phase transition. The strips were subjected to several rolling pass and then annealed at different temperatures and times. In this case, the maximum thickness reduction for one pass was 21,6%, while the thickness reduction of the traditional rolling for NiTi alloys is around 10%. In addition, NiTi can be rolled at a relatively low temperature and spending shorter times, therefore the oxidation in the process is reduced. As given by Figure 2.21, the EPRed NiTi strips after annealing exhibits an excellent superelasticity and a recoverable strain of 6% is obtained [Zhu, 2013].

Stolyarov reports that EPR can be used for the fabrication of ultrafine-grained microstructure and nanostructure in long-sized semifinished NiTi products, which is on the contrary a complicated task by traditional metal working methods due to high strength and limited deformability of these materials. The type of the structure is determined mainly by the density of the pulse current as well as the degree of plastic strain [Stolyarov, 2009]. It is also found that EPR allows enhanced deformability of TiNi alloys together with improved strength and retained ductility [Stolyarov, 2012].

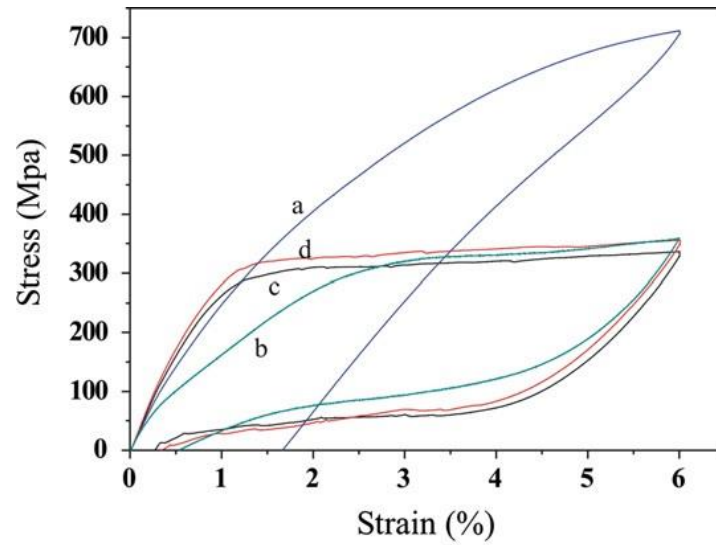


Figure 2.21 Superelastic properties of TiNi strips: (a) EPRed, (b) annealed at 400 °C for 30 min, (c) annealed at 500 °C for 30 min and (d) annealed at 500 °C for 60 min [Zhu, 2013].

The influence of chemical composition of NiTi-based SMAs on the EPR processing is investigated by Potapova et al., highlighting the main differences obtained after the processing of bars with different contents of the two elements. In particular, microstructure, microhardness and deformability are measured, and the possible reasons for the different behaviors are discussed [Potapova, 2013].

CHAPTER 3:

3 Aims of the work

The aim of this experimental study is to deepen the knowledge about the laser treatment of shape setting used as an alternative to conventional techniques for the treatment of thin Nitinol superelastic wires.

The focus of the research is in the first place the evaluation of the effects of the tension load applied to the wire during straight annealing, which is a fundamental parameter of this technological process, but which effects are nowadays not exhaustively investigated. The first goal is the adjustment of the available wire clamping system with the addition of a load cell and its dedicated measuring system, allowing the control of the force imposed to the wire. As second goal, four levels of uniaxial stress are selected for the analysis and their effects are measured in a finite range of incident power of the laser beam, in turn divided into three power levels. Characterizations are performed through differential scanning calorimetry, tensile test and metallographic analysis.

Furthermore, previous investigations concerning the laser annealing carried out through calorimetric and stress-strain characterization, available in literature, are extended in order to better understand the phenomena underlying the alloy modifications during laser annealing. This analysis is performed through mechanical cycling tests, which predict the material behavior during the component functioning in terms of response stability, and metallographic observations, useful to point out the reasons for the results in terms of functional properties obtained in the wires. The goal is to correlate the different aspects investigated to achieve an extensive understanding of the process.

The comparison between laser annealed samples and furnace treated samples, analyzed as first step of this work, further help in the process of determination of the influence of the analyzed process parameters, both from a macroscopic and a microscopic perspective. As a reference condition

for optimized wire properties, also the commercially available straight annealed wire is compared to the laser annealed samples.

CHAPTER 4:

4 Definition of materials, equipment and processes

4.1 Materials

The material used in this thesis work is quasi-equiatomic superelastic Nitinol under the form of thin wires mod. SmartFlex® produced by SAES® Getters Group, company specialized in the development and manufacture of Nitinol semifinished products, components and devices for industrial and medical applications (see Figure 4.1).



Figure 4.1 Commercially available wire spools from SAES Getters Group.

In particular, four different types of commercially available wire are subjected to the analyses presented in this work:

- 100 μm diameter as drawn (cold worked) wire;
- 100 μm diameter straight annealed wire;
- 200 μm diameter as drawn (cold worked) wire;
- 200 μm diameter straight annealed wire.

The homogeneity of the material properties is maximized by the use of samples belonging to the same spool for every type of wire examined. The as drawn wire, which presents a strain hardening due to the cold deformation undergone by the material, is used as starting material for the subsequent annealing treatments hold in the laboratory with both conventional and unconventional techniques. The straight annealed wire, subjected by the producer to furnace annealing under applied load and then trained to optimize the material properties, serve as parameter of comparison for the final material characterization.

The first step of this work is the characterization of the commercial wire for both conditions used, i.e. as drawn wire and straight annealed wire. In the following, the as drawn material is noted as CW, that stands for cold worked, and the straight annealed wire is noted SA.

4.1.1 As drawn wire

Figure 4.2 (a) and (b) show the calorimetric response for the CW wires of 100 and 200 μm diameter respectively. As expected, these curves do not present the phase transformation peaks, since the martensitic transformation is prevented by the strain hardened state of the material. As seen in previous studies [Miller, 2001; Braz Fernandes, 2013], this condition of the material is strongly required as starting point for the subsequent annealing treatments performed with both furnace and laser technology.

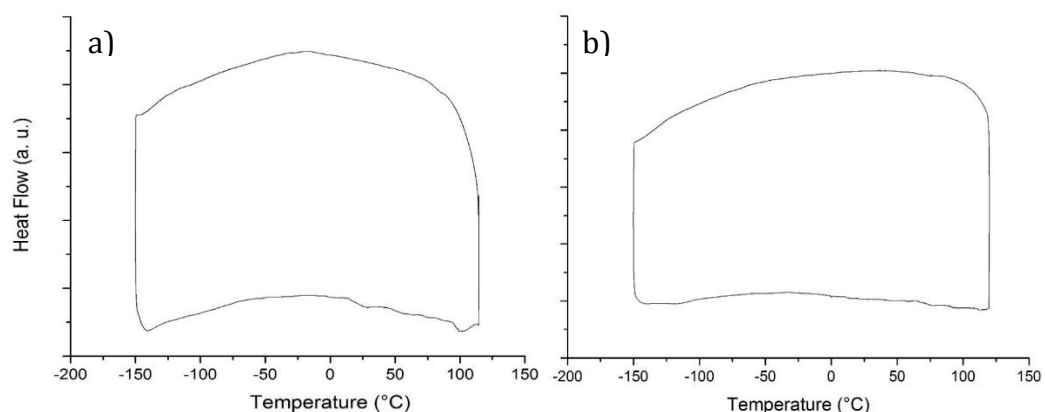


Figure 4.2 DSC curve of the 100 μm (a) and 200 μm (b) as drawn wire.

Figure 4.3 (a) shows the stress-strain curve for the cold worked 100 μm wire. The material is hardened due to the cold working, so the wire oppose a good resistance to the strain, requiring high stress values to deform, and it breaks after a small percentage of deformation. As seen from DSC analysis, this behavior clearly implies the lack of martensite transformation in the alloy. Starting from this condition, an annealing treatment is required to induce the superelastic behavior of the wire. The corresponding curve for the 200 μm sample (see Figure 4.3 (b)) is interrupted before the fracture of the wire due to the force limit of the load cell of the instrument, but it is useful to compare the initial slope of the two curves as a confirmation of the wire behavior.

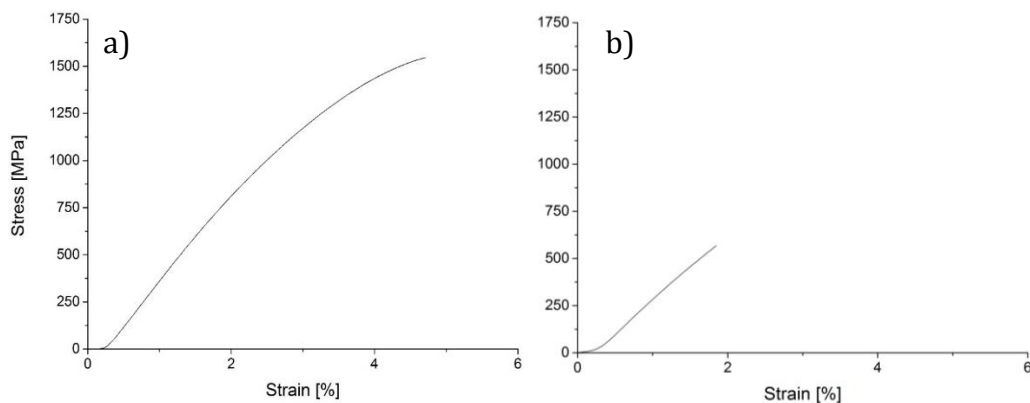


Figure 4.3 Stress-strain curve of the 100 μm (a) and 200 μm (b) as drawn wire.

4.1.2 Straight annealed wire

The functional properties of the straight annealed wires are shown in the calorimetric curves in Figure 4.4 (a), wire of diameter 100 μm , and Figure 4.4 (b), wire of diameter 200 μm ; these properties will be the reference condition for the evaluation of the results of the unconventional treatment.

The material shows two exothermic peaks on cooling and two endothermic peaks on heating, these two almost overlapped for the 100 μm wire. During the transformation from austenite to martensite the first exothermic peak at higher temperature corresponds to the reaction from austenite (A) to

rombohedral-phase (R), while the second exothermic peak at lower temperature corresponds to the reaction from rombohedral-phase (R) to martensite (M). In the reverse transformation, from martensite to austenite, the two endothermic peaks are due to the presence of the rombohedral-phase transformation also during heating. Analyzing the curve representing the heat flow as a function of sample temperature, it is possible to identify the temperatures that characterize these transformations occurring inside the material in the annealed condition, reported in Table 4.1 and Table 4.2. The terms M_s , M_f , R_{cs} and R_{cf} are the temperatures of the martensite and R-phase start and finish of transformation on cooling, while the terms A_s , A_f , R_{hs} and R_{hf} are the temperatures of the austenite and R-phase start and finish of transformation on heating. The enthalpy of transformation upon cooling and heating is instead noted as $\Delta H_{cooling}$ and $\Delta H_{heating}$, respectively. Looking at the austenite finish temperature it can be observed that the SA sample presents an austenite and R-phase structure at room temperature, while it is fully austenitic at human body temperature.

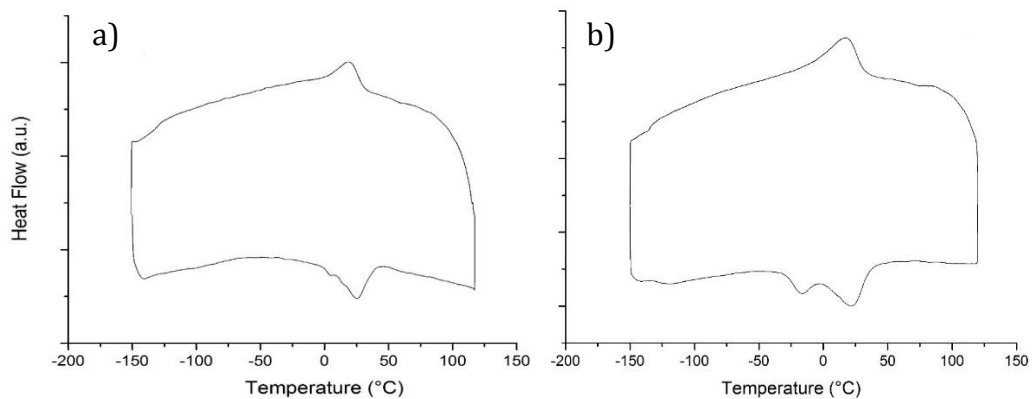


Figure 4.4 DSC curve of the 100 μm (a) and 200 μm (b) straight annealed wire.

Φ [μm]	M_s [$^{\circ}\text{C}$]	M_f [$^{\circ}\text{C}$]	R_{cs} [$^{\circ}\text{C}$]	R_{cf} [$^{\circ}\text{C}$]	$\Delta H_{cooling}$ [J/g]
100	-0.4	-134.9	33.2	0.4	5.08
200	-9.1	-134.6	32.3	-9.1	4.73

Table 4.1 Phase transformation temperatures and enthalpy value for the straight annealed wires upon cooling.

Φ [μm]	A_s [$^{\circ}\text{C}$]	A_f [$^{\circ}\text{C}$]	R_{hs} [$^{\circ}\text{C}$]	R_{hf} [$^{\circ}\text{C}$]	$\Delta H_{\text{heating}}$ [J/g]
100	7.4	36.7	-31.5	7.4	6.98
200	-3.8	36.2	-30.3	-3.8	6.65

Table 4.2 Phase transformation temperatures and enthalpy value for the straight annealed wires upon heating.

Figure 4.5 (a) presents the mechanical response at room temperature for the straight annealed 100 μm wire. The wire undergoes the imposed deformation of 8% without breaking and, after the unloading phase, it has a very small amount of residual deformation. The initial elastic response is followed starting from 1.63% strain by a plateau region, during which transformation from austenite to martensite occurs under increasing strains. Upon completion of the transformation at approximately 6.50% strain, further loading results in elastic deformation of the fully transformed martensite matrix. Unloading of the transformed material is initially elastic, followed by a second plateau region, during which the reverse transformation occurs. Finally, elastic unloading of the regenerated austenite phase takes place. The plateau is clearly distinguishable both for loading and unloading phases, giving to the curve the characteristic shape of the superelastic flag: it clearly testifies the presence of the superelastic effect in the material. Also in this case, a complete mechanical characterization for the 200 μm wire is not provided due to the force limit associated to the available DMA instrumentation, but the initial part of the curve is visible in Figure 4.5 (b). Table 4.3 displays the most meaningful values of stress and strain extracted from the DMA analysis for the 100 μm wire. The terms σ_{loading} , $\sigma_{\text{unloading}}$ and $\Delta\sigma$ refer to the plateau stress on loading, plateau stress on unloading and mechanical hysteresis, while the terms ϵ_{start} , ϵ_{finish} , $\Delta\epsilon$ and $\epsilon_{\text{residual}}$ indicate the plateau start strain, plateau finish strain, plateau total length and residual deformation, respectively.

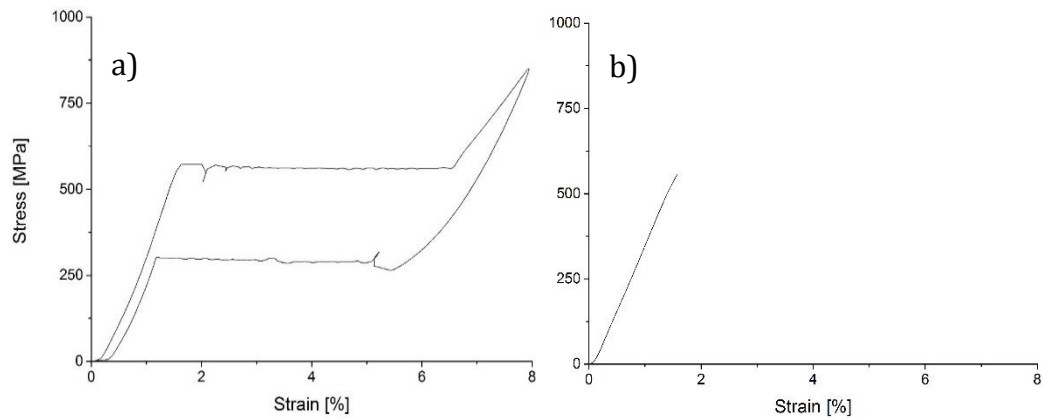


Figure 4.5 Stress-strain curve of the 100 μm (a) and 200 μm (b) straight annealed wire.

σ_{loading} [MPa]	$\sigma_{\text{unloading}}$ [MPa]	$\Delta\sigma$ [MPa]	ϵ_{start} [%]	ϵ_{finish} [%]	$\Delta\epsilon$ [%]	$\epsilon_{\text{residual}}$ [%]
560	292	268	1.63	6.50	4.87	0.31

Table 4.3 Characteristic stress and strain values for the 100 μm straight annealed wire.

4.2 Conventional heat treatment

The conventional heat treatment of the wires is carried out using a muffle furnace (Figure 4.6).



Figure 4.6 Muffle furnace used for the conventional heat treatment.

With this technique, both wires of 100 μm and 200 μm diameter are treated, starting from the initial condition of cold worked material.

The wire is cut in segments of 8 cm, length required to allow the subsequent characterizations, and the segments are introduced in a small tube of quartz to preserve the straightness during the treatment. The whole is then inserted into a second larger tube of quartz.

The treatment is performed at nine different levels of temperature in the interval between 300 and 800 $^{\circ}\text{C}$. The soaking time is always equal to 12 minutes, that is a duration long enough to allow the stabilization of the temperature inside the sample and guarantee a uniform treatment of all the material, but short enough to avoid the oxidation of the surface of the wire.

The treatment is performed in air, while the quenching takes place in water at ambient temperature. The parameters set, equal for both the diameters of wire, are listed in Table 4.4.

Ø wire [µm]	Temperature [°C]	Time [min]	Quenchant
100/200	300	12	Water
100/200	400	12	Water
100/200	450	12	Water
100/200	500	12	Water
100/200	550	12	Water
100/200	600	12	Water
100/200	650	12	Water
100/200	700	12	Water
100/200	800	12	Water

Table 4.4 Test conditions for the furnace treatment.

4.3 Unconventional heat treatment

The unconventional heat treatments of the wires are performed through laser technology, with the laser system described in the following section.

4.3.1 Laser system

The annealing treatment of the Nitinol wires is performed with an ytterbium active fiber laser source operating in continuous emission mode, with maximum output power 300 W and wavelength 1064 nm (IPG Photonics, model YLR-300/3000-QCW-MM-AC-Y12), shown in Figure 4.7. Through the appropriate display it is possible to adjust the percentage of the power to be used.

The laser beam is collimated and then focalized through a laser head (Laser Mech, model Fiber Mini), shown in Figure 4.8. This laser head is suitable for a wide range of applications and provides the possibility to add an assistant gas during the process. The head positioning along the vertical axis is controlled by means of a manual slide mounted above it. In this way it is possible to perform the treatment imposing the desired distance between the focal lens and the working surface.



Figure 4.7 Laser source IPG Photonics YLR-300/3000-QCW-MM-AC-Y12.



Figure 4.8 Laser head model Fiber Mini from Laser Mech.

The distance between the focal lens and the sample surface is related to the beam diameter according to the caustic of the laser beam, whose trend is represented in Figure 4.9 for the analyzed laser system. The waist diameter, with respect to the nozzle exit hole, is placed at a distance of 1 mm. Figure 4.10 shows the corresponding trend of the irradiance, which is the amount of power for surface unit, on varying the distance from the focal position.

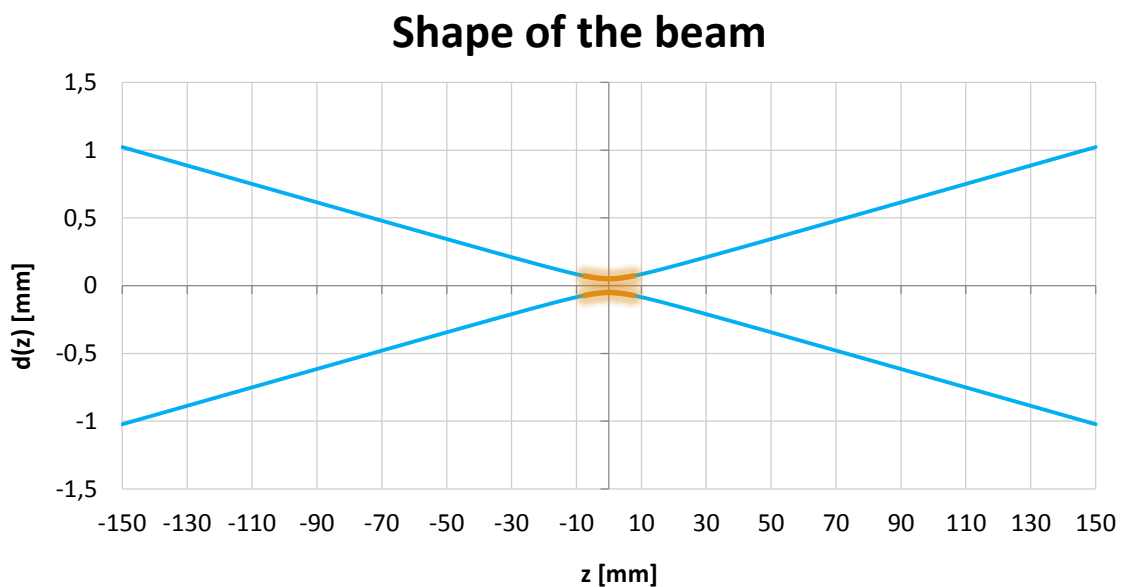


Figure 4.9 Caustic of the laser beam beyond the focalization lens; the depth of field is highlighted in orange.

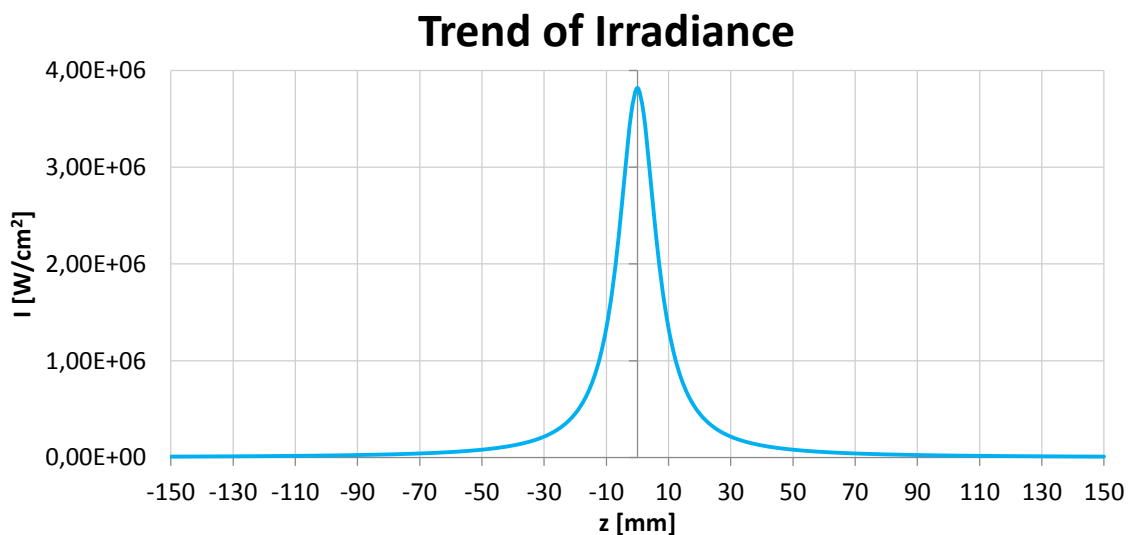


Figure 4.10 Trend of the irradiance of the laser beam as a function of the distance from the focal position.

The main characteristics of the laser system are listed in Table 4.5.

Parameter	Description	Value
λ [nm]	Emission Wavelength	1070
d_{fo} [μm]	Core Fiber Diameter	50
BPP	Beam Product Parameter	1,70
M^2	Beam Quality Factor	4,99
f_r [mm]	Collimation Length	75
f_f [mm]	Focal Length	150
d_o [mm]	Waist Diameter	0,10
Δz_{pdc} [mm]	Depth Of Field	7,34
P_{CW} [W]	Max Output Power (CW)	300

Table 4.5 Main characteristics of the laser system.

A two-axes motion stage (Aerotech, model PRO165LM) allows the control of the relative displacement on the horizontal plane between the laser beam and the working surface (Figure 4.11). During the process, the laser head remains in a fixed position, while the sample is mechanically moved along the required path. The motion and the control of the axes are managed from the computer by means of a specific software. In particular, from the program interface it is possible to set the starting position, the trajectory and the speed assigned to the moving part of the system during the working cycle.

The sample is placed on a specific aluminum support and it is fixed with two locking plates (Figure 4.12 (a)). This sample holder was designed and realized inside the laboratory and is provided with a mobile column which allow the adjustment to different lengths of the workpiece, varying in a range between 2 and 10 cm. A load cell is mounted on the fixed column of the sample holder in order to allow the application and the measurement of loads acting on the sample (Figure 4.12 (b)).

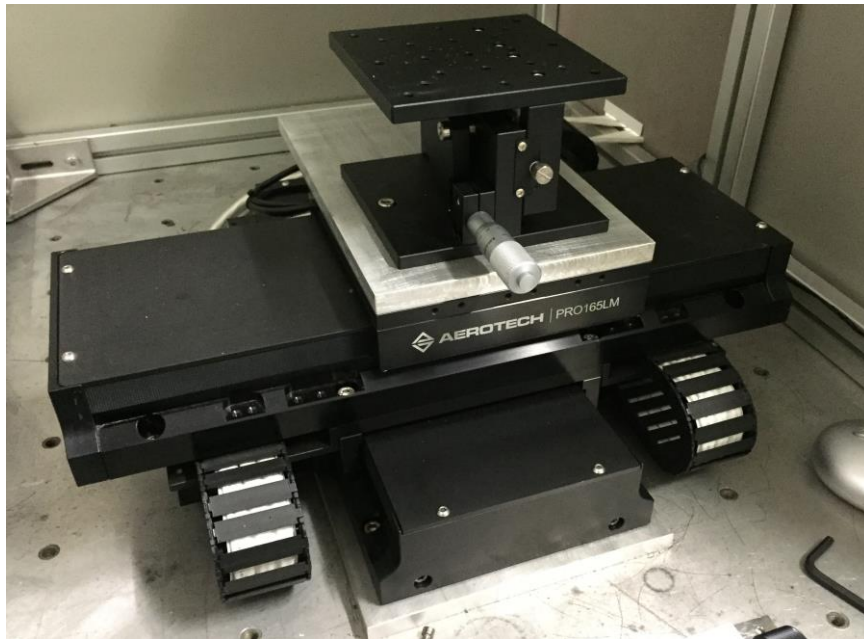


Figure 4.11 2D motion stage used for the control of the sample holder (Aerotech - PRO165LM).

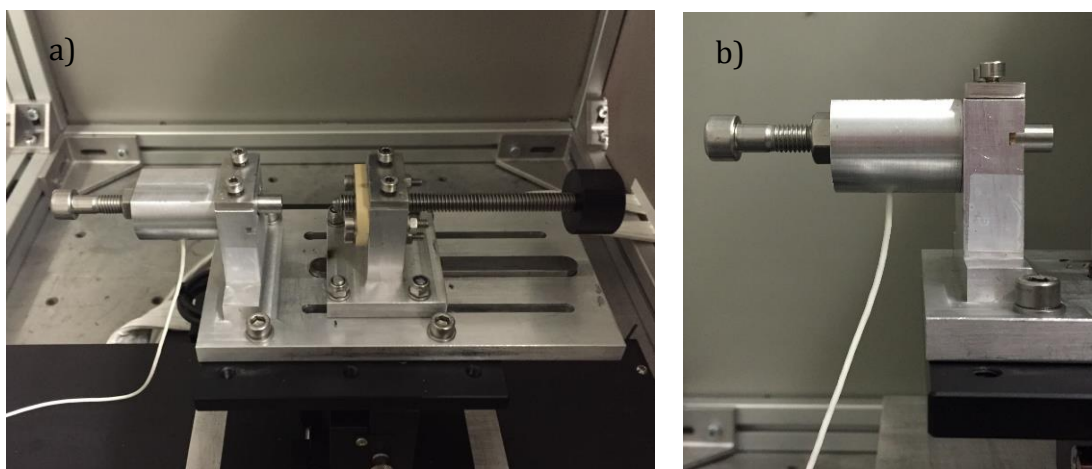


Figure 4.12 Complete view of the sample holder mounted on the motion stage (a) and detail of the structure containing the load cell (b).

A screw is placed on the sliding column of the sample holder and through its tip it can transmit a load to the sensor, corresponding to the load applied on the Nitinol wire. The cell is placed in a metallic structure, designed to meet the need of a better precision in the application of the load. In

particular (as clearly visible in the drawing reported in Appendix A) this structure allows the application of a preload on the cell through a compression spring which can act on the load cell before the heat treatment, shifting the working range of the instrument to higher output values. It also guarantees a more stable contact between the screw tip and the cell sensor, avoiding radial loads and providing a pure axial stress, required for a correct measurement of the load. The load cell is linked to an amplifier module and a device for the acquisition of the output data.

The main purposes of the load cell relatively to the annealing of the wires are:

- to quantify the preload applied to the wire during its positioning to allow an accurate replication of the stress field to which the wire is subjected in the treatments;
- to understand the effects of the application of a preload on the wire before the carried out of the treatment on the final superelastic behavior of the wire, in terms of characteristic temperatures variation, microstructure orientation and mechanical properties modification.

The load cell utilized in this work is the model 8416-5020 with amplifier module model 9235 (Figure 4.13 (a) and (b)), both produced by the Burster company.

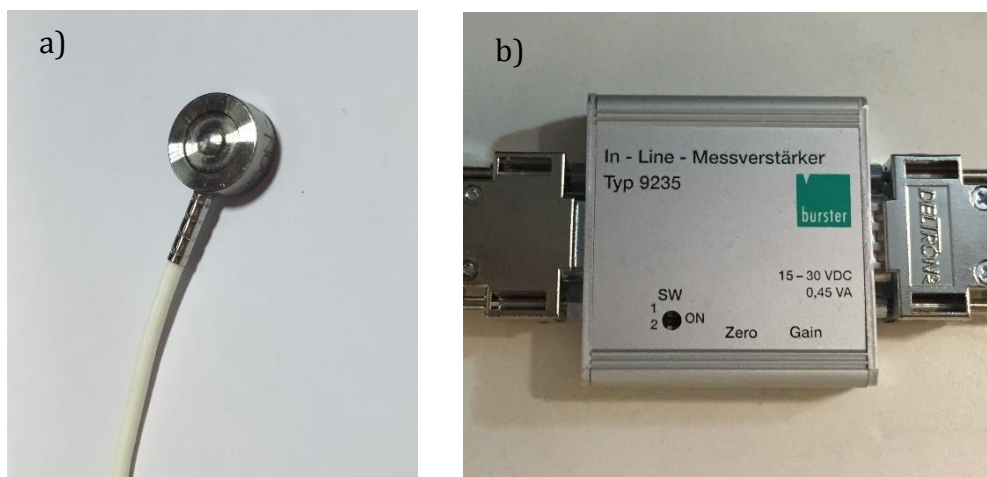


Figure 4.13 Load cell 8416-5020 (a) and amplifier 9235 (b).

The main characteristics of load cell and amplifier are listed in Table 4.6 and 4.7.

Sensor type	Compression load cell
Nominal force	0-20 N
External diameter	10,6 mm
Sensor diameter	3 mm

Table 4.6 Technical specifications of the load cell.

Supply voltage	15-30 V _{DC}
Input power	15 mA
Output voltage	0±10 V

Table 4.7 Technical specifications of the amplifier.

Also the temperature of the laser source is a critical parameter for the repeatability of the annealing treatment, so an air conditioning device is placed in the laser room, allowing to keep the temperature in a proper working range.

Figure 4.14 shows the entire laser system in the configuration used for the treatments presented in this work. The working area is contained in a metallic structure to protect the surroundings from the laser radiations.

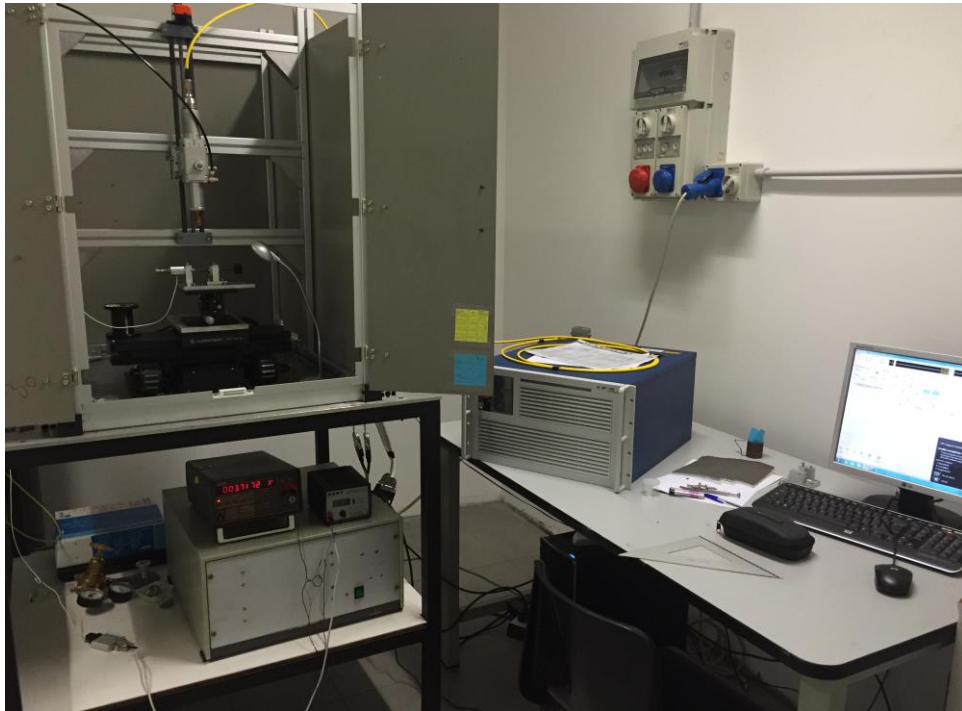


Figure 4.14 View of the complete laser system utilized in this work.

4.3.2 Calibration of the load cell

Before the load cell mounting on the laser system, it is necessary to perform a calibration of the instrument itself. The calibration operation is a necessary step to determine the characteristic relation between input (applied load [N]) and output (tension [V]) of the instrument. In this case it was followed the method of application of known masses.

To perform the calibration, a special structure was built, shown in Figure 4.15.



Figure 4.15 System used for the calibration of the load cell.

The load cell, positioned in the horizontal plane and fixed to a small metallic plate, is connected through a cable to the amplifier to provide the supply voltage and at the same time multiply the signal in output from the cell. The amplifier is provided with a quadrupole cable to enable the connection with the power supply (HP, model E3632A) and the voltmeter (Keithley, model 196 DMM), visible in Figure 4.16.

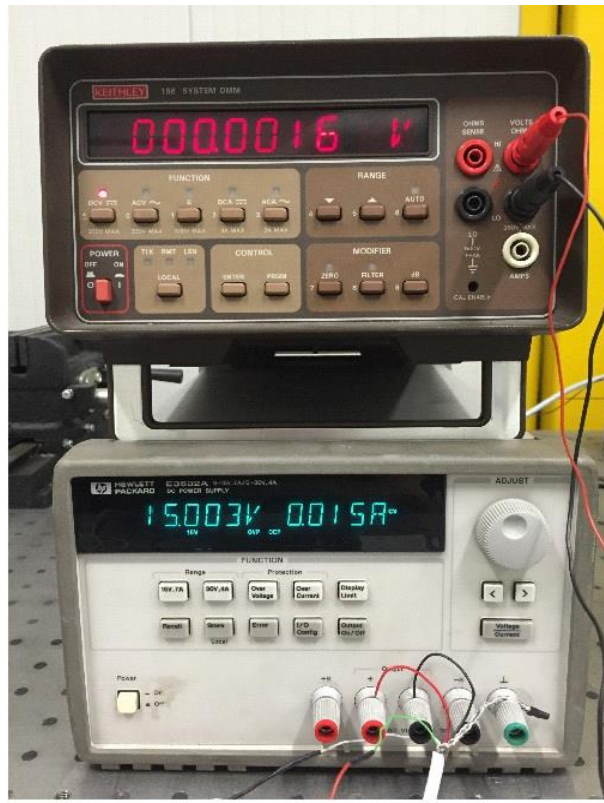


Figure 4.16 Voltmeter and amplifier used for the cell calibration.

Once the supply of the load cell is settled, from the amplifier the values of nominal sensitivity, zero value and gain are selected on the basis of the range of voltage desired as output. The main parameters of the system, in the configuration used in this work, are listed in Table 4.8.

Supply voltage	20 V
Supply current	15 mA
Nominal sensitivity	2 mV/V (switch 1 e 2 open)
Gain	4 V/kg

Table 4.8 Main characteristics of the calibration system.

A guide is placed over the load cell for the insertion of a screw rod with a special tip which allows the correct transmission of the forces in the contact

with the cell (Figure 4.17(b)). Subsequently the is placed in the structure and some weights are applied on it (Figure 4.17(a)), previously measured with a scale and selected with a step of 100 g in the range from 0 to 2 Kg. All the procedure is repeated five times to verify the repeatability of the measurements, varying every time the application order of the weights to avoid the presence of systematic errors.

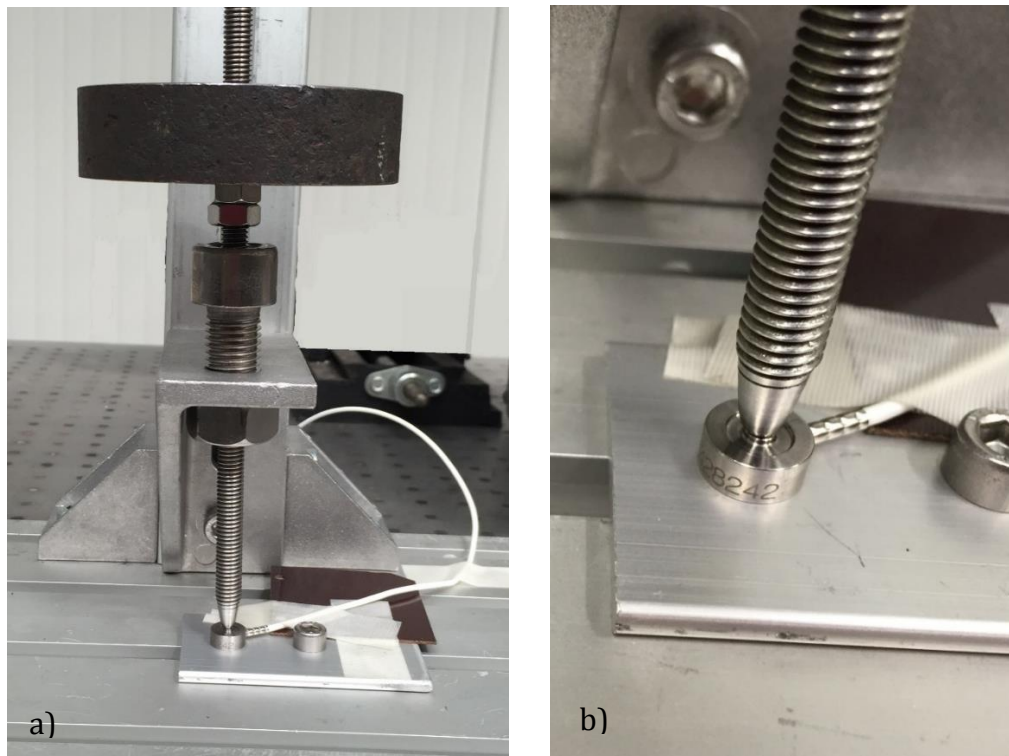


Figure 4.17 Load cell with a test mass applied (a) and detail of the contact between screw tip and load cell (b).

From the preformed tests, calculating the average of the voltage signals measured as output, the calibration curve of the load cell is obtained, as reported in Figure 4.18. The value of the applied load in newton is attained multiplying the value of the corresponding mass for the gravitational acceleration. As it can be seen from the graph, the curve shows a liner trend for all the considered range.

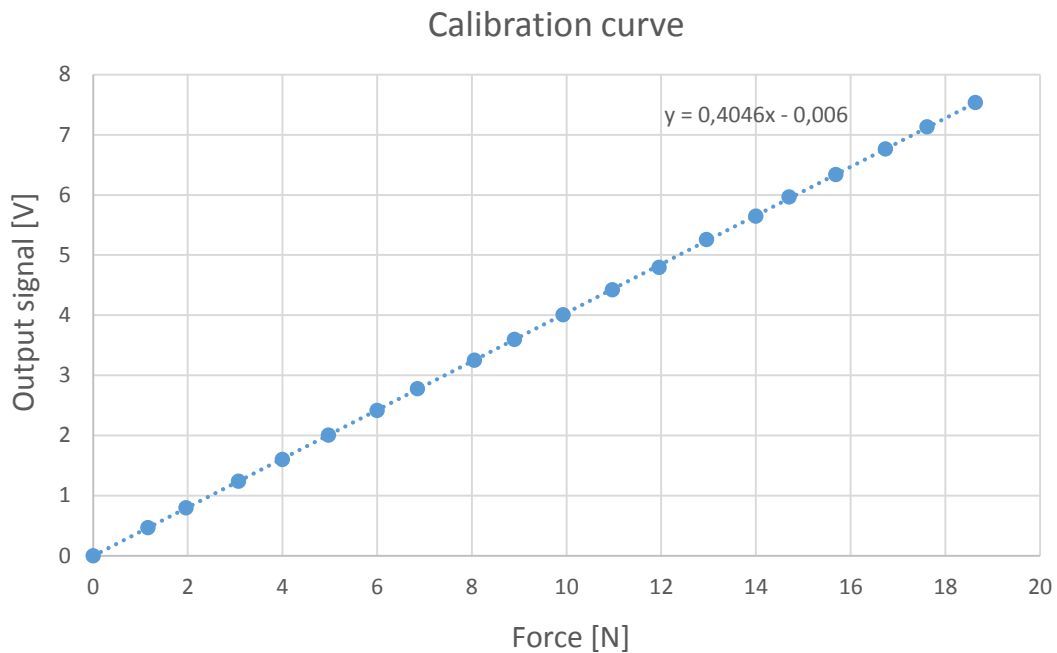


Figure 4.18 Calibration curve of the load cell.

By using the method of linear regression, it is possible to find the equation of the straight line which approximate the calibration curve, used for the conversion of the output signal form volt to newton (or vice versa):

$$y = 0,4046x - 0,006 \quad \text{with} \quad \begin{cases} y = \text{output signal [V]} \\ x = \text{applied force [N]} \end{cases}$$

In Figure 4.19, the trend of the standard deviation between the values found as output signal is reported in function of the applied load, both in volts and percentage. This value allow us to estimate the resolution of the measuring system used in function of the considered load. As expected, the value of the error rises when the mass applied to the system increase, but its trend is almost linear if evaluated as percentage of the corresponding output signal.

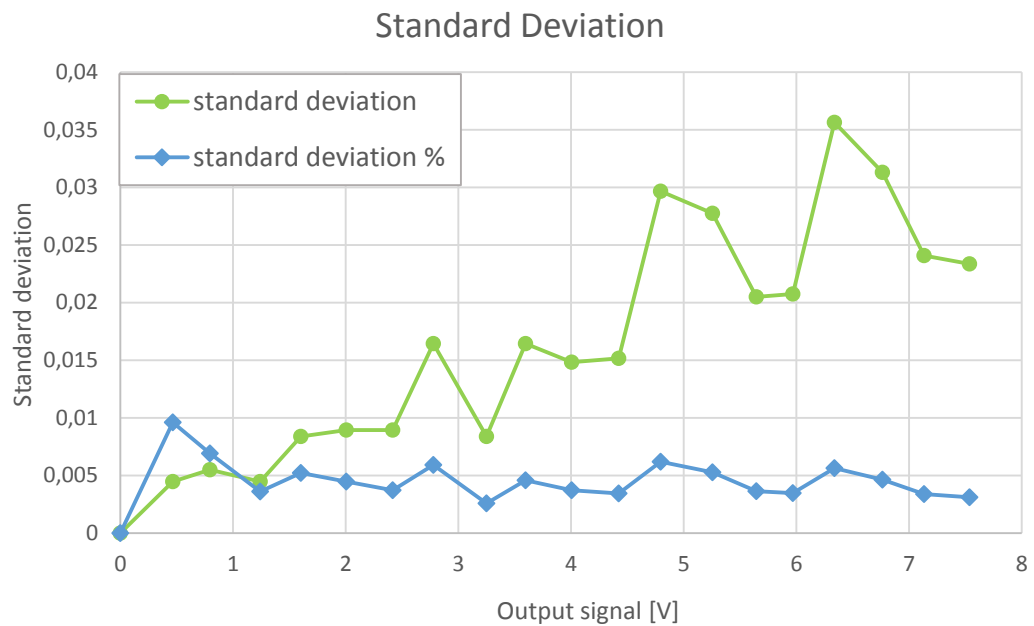


Figure 4.19 Standard deviation calculated on the five calibration tests carried out on the load cell.

Last step is the mounting of the load cell in the laser system, inside the specific structure designed to contain it.

4.3.3 Laser shape setting

To perform the annealing through laser technology, the wire is clamped to the sample holder, placed under the laser head (Figure 4.20), which is composed by a fixed column and a sliding column. Then the desired load is imposed through the rotation of the screw applied in front of the load cell, so that the force applied is all transferred to the wire, but its value is measured by the sensor. During the annealing treatment, the sample is moved linearly by the motion stage, so that the laser beam hits the wire along all the length included between the clamps, equal to 40 mm.

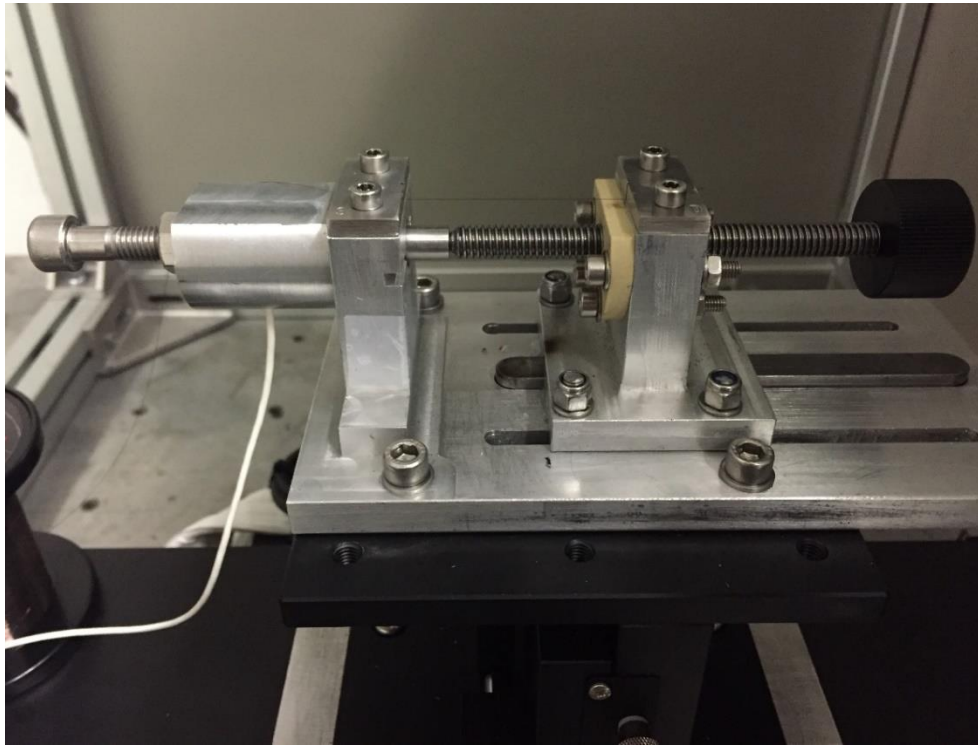


Figure 4.20 Detail of the sample holder with the Nitinol wire positioned and preloaded to perform the laser annealing.

During the laser shape setting, a portion of the incident power of the beam is transferred to the wire surface, depending on how much the laser beam is defocused. In this work, the distance between the focal position and the top surface of the wire is set equal to 97 mm, so the beam diameter in correspondence of the interaction point is 1,3 mm. The choice of this focal height, far from the focus position, is due to two main reasons: to make easier the positioning of the sample in the center of the laser beam, larger than the thin Nitinol wire; to have an almost uniform power distribution incident on the wire, due to the Gaussian shape of the power distribution. The interaction between the laser beam and the wire is schematically represented in Figure 4.21. It can be estimated that a heat flow having an almost flat profile is transferred to the upper surface of the wire. Due to the small wire diameter, it can be considered that all the wire portion, under the laser beam, can be quickly and uniformly heated up.

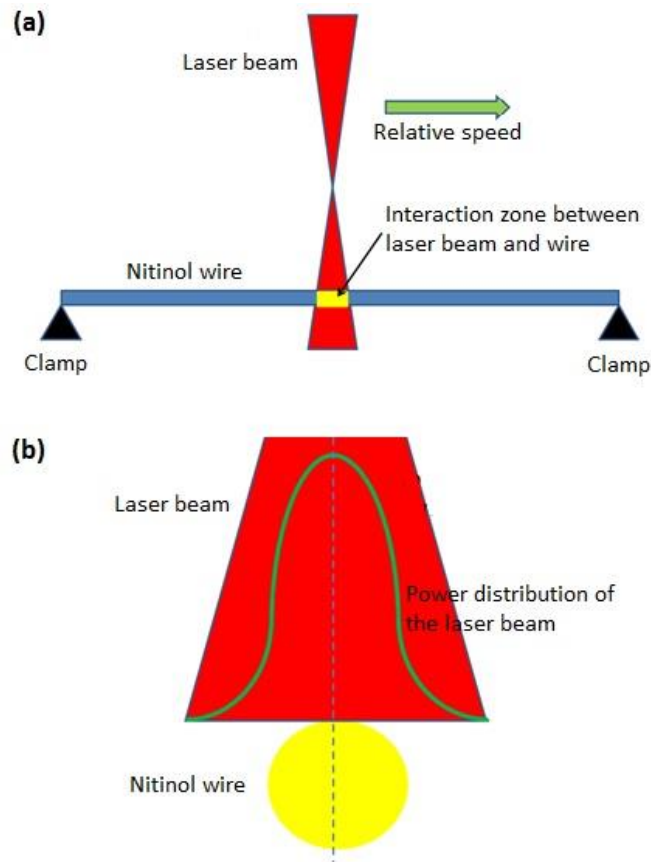


Figure 4.21 Schematic of the NiTi wire laser shape setting process: longitudinal (a) and transversal (b) view.

The laser annealing parameters used for the shape setting of the wires are summarized in Table 4.9, both fixed and variable. All laser shape setting treatments are performed with RT between the range from 21 to 22 °C to avoid fluctuations of the power supplied by the diode source, so to guarantee an higher conformity among test conditions. In addition, no assistant gas is used, so all the treatments are performed in air. All the wire segments used for the treatment are in a cold worked condition before the heat treatment. The choice of the speed of the treatment is based on previous studies held on Nitinol superelastic wires of the same size [Zohari, 2015] and is maintained as constant parameter for all the laser annealing campaign, equal to 50 mm/s.

Source temperature	21-22 °C
Assistant gas	No
Treated length	40 mm
Environment	Air
Process speed	50 mm/s
Power	65-75-85 W
Load	5-50-150-300 MPa

Table 4.9 Laser annealing fixed and variable parameters used in this work.

The variables investigated in this work for the laser annealing are incident power and preload applied during the treatment. Three different levels of incident power are set: 40%, 42,5% and 45%. For the system used, the incident power levels corresponds to 65 W, 75 W and 85 W respectively. This range of power is selected on the basis of previous researches [Zohari, 2015; Biffi, 2016] as an interval of incident power that is able to correctly induce the functional properties on the Nitinol wire, avoiding the limit cases of lack of transformation or melting of the sample. For every power level, four different values of preload are set: 5 MPa, 50 MPa, 150 MPa and 300 MPa. The first load condition (5 MPa) is an attempt to simulate the condition of annealing performed without preload; a minimum load is applied in order to guarantee the wire positioning and the treatment homogeneity.

The visualization of the design of experiments is shown in Figure 4.22. For each process condition, three replications were done for evaluating the repeatability of the process.

All treatment conditions are investigated in the 100 μm diameter wire.

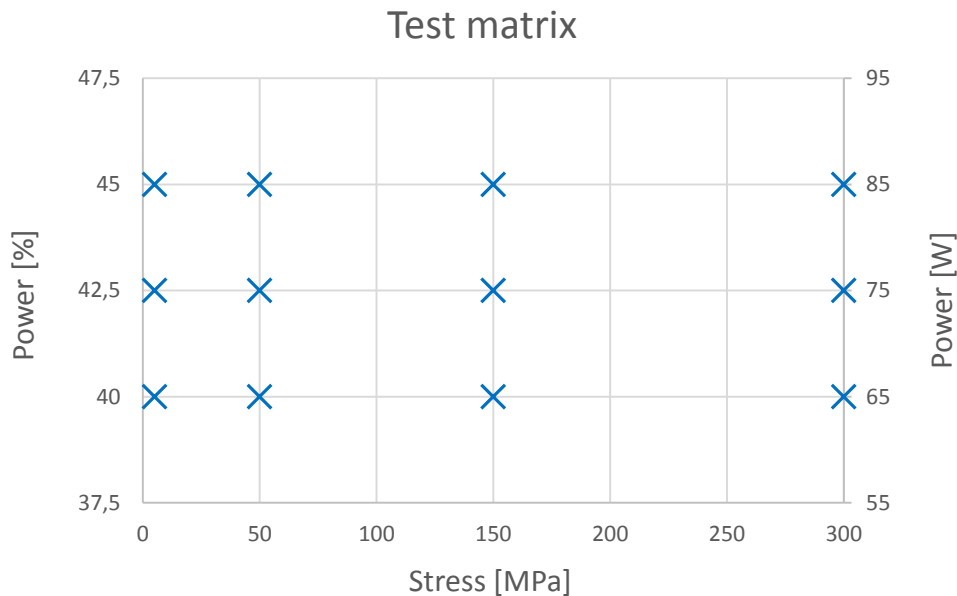


Figure 4.22 Complete test matrix of the laser annealing campaign. The blue crosses represent the conditions investigated for the 100 μm diameter wire.

4.4 Methods of characterization

4.4.1 Calorimetric analysis

One of the most diffused techniques for the characterization of the transformations in the SMAs is the *differential scanning calorimetry*, known also with the acronym DSC. This technique is based on the measurement of the difference of heat flow between the sample under examination and a reference sample during an imposed thermal cycle.

The simplified scheme of the inner part of the instrument is presented in Figure 4.23. The pan containing the sample under analysis is placed in a special housing inside the measuring chamber, which is provided also with a space for an empty pan, used as reference sample for the test. Successively it is hermetically closed to insulate the working environment from the outside. The presence of the reference pan is of fundamental

importance to obtain an output signal that is independent on the thermic effects external to the system and it allows to detect as output the own behavior of the material itself, regardless of the experiment conditions. The temperature of the two samples is monitored through thermocouples placed in the platform below the aluminum pans.

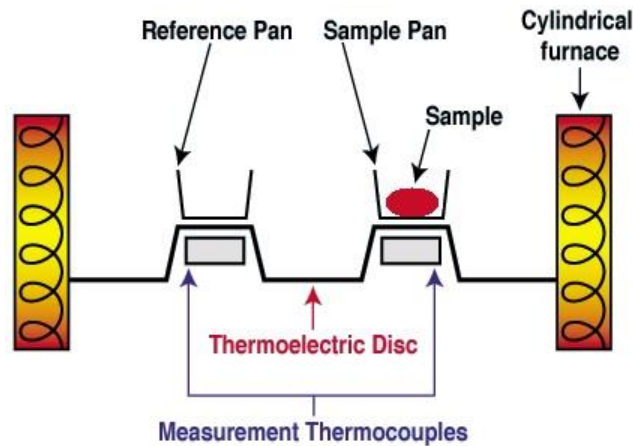


Figure 4.23 Scheme of the measuring chamber of the DSC (www.psrc.usm.edu).

The basic principle is that, when the sample undergoes a phase transformation during the imposed thermal cycle, more or less heat will be transferred to it with respect to the reference pan to maintain them at the same temperature. The increase or decrease of the heat flow absorbed by the sample depends on the process type: if endothermic, more heat is required to compensate the heat removed during the transformation; if exothermic, less heat is needed to maintain the sample temperature.

The result of the DSC analysis is a curve representing the heat flow as a function of the sample temperature, as shown in Figure 4.24. From this curve it is possible to measure for every peak:

- the *characteristic temperatures* of transformation start and finish, identified by the intersection between the tangents to the slope of the peak and the tangent of the baseline;

- the *latent heat*, or enthalpy, of the transformations involved, equal to the product between the area under the peak and a calorimetric constant of the instrument.

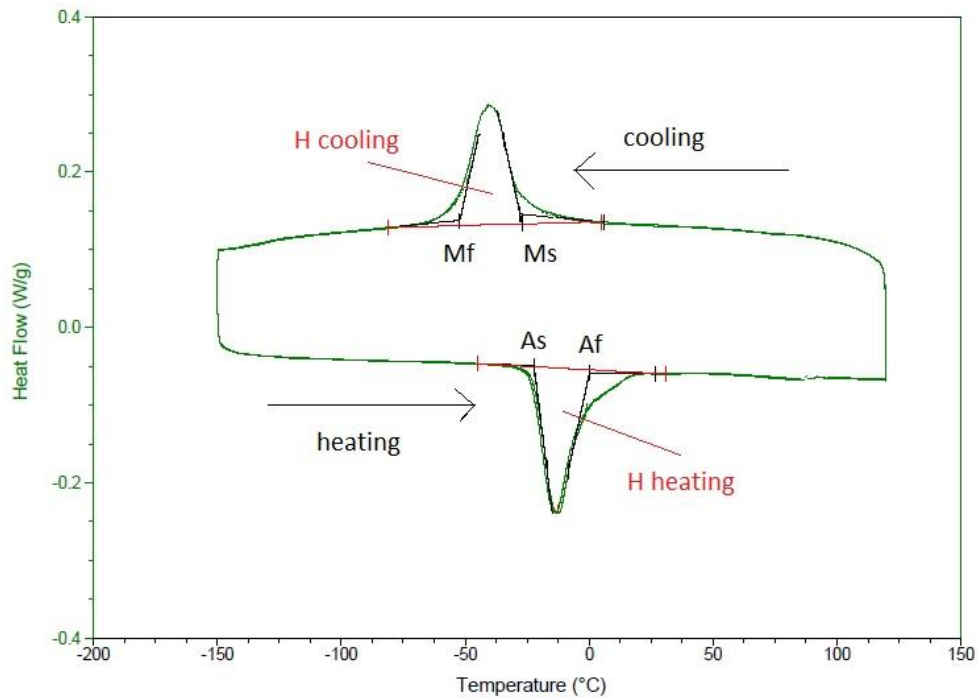


Figure 4.24 DSC curve for a generic Nitinol SMA, with visible phase transformations upon cooling and upon heating and corresponding characteristic temperatures and enthalpies indicated.

The model of DSC used in this work is Q100 produced by TA Instruments (Figure 4.25) equipped with liquid nitrogen cooling system (LNCS). The main characteristics of the DSC system are listed in Table 4.10.

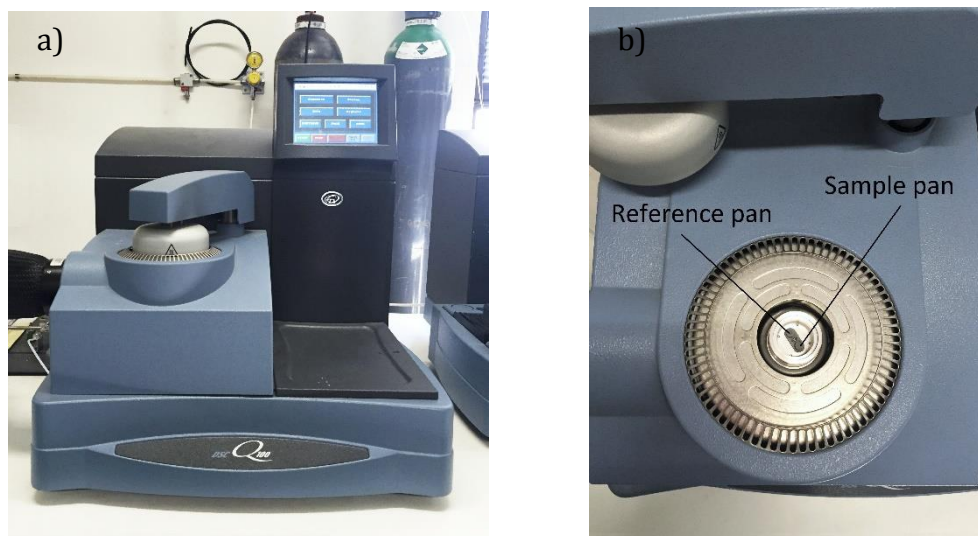


Figure 4.25 DSC used in this work, model Q100 TA Instruments, (a) and detail of the measuring chamber (b).

Temperature range	From -180 to 550 °C
Shielding gas	Nitrogen and helium
Cooling system	Liquid Nitrogen
Sample pan	Aluminum pan with lid
Shielding gas flow	50 mL/min
Sample weight	Between 0.5 and 100 mg

Table 4.10 Main characteristics of the DSC system used in the analysis.

In order to make the calorimetric analysis of the material, the wires are cut into pieces of length equal to 4-5 mm, weighed and collected in small aluminum pans. All the samples used in the tests need to have a minimum total length sufficient to guarantee an adequate contact surface between the material and the thermocouple. Samples are subjected to heating and cooling cycles between -150 °C and 120 °C at a rate of 10 °C/min , interposing between each ramp 2 minutes of isothermal soaking to stabilize the material condition. Each test involves the realization of three consecutive cycles for each sample to check the stability of the response. The tests are conducted in a controlled atmosphere, provided by a continuous flow of helium and nitrogen.

4.4.2 Mechanical analysis

Dynamic mechanical analysis, abbreviated DMA, is a very useful technique for the study and the characterization of SMAs. This technique is based on the measurement of the strain of the sample when a stress is applied to the material at a given temperature. A general schematic of the primary components of a DMA instrument is shown in Figure 4.26.

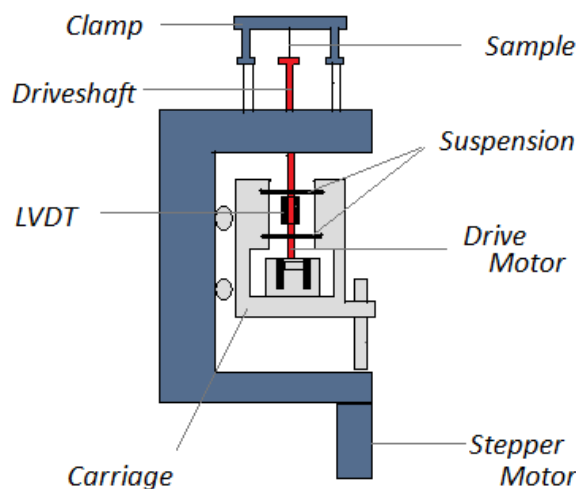


Figure 4.26 General schematic of a DMA instrument. [en.wikipedia.org]

The instrumentation of a DMA is provided with a displacement sensor, such as a linear variable differential transducer (LVDT), a temperature control system or furnace and a drive motor to provide the oscillatory or static force required. The drive motor transmits force directly to a rectangular air bearing slide. Pressurized air flows to the bearings forming a frictionless surface that permits the slide to “float”. In this way, very weak materials like films and fibers can be characterized with ease. In order to hold the sample being tested, sample clamps are present in the upper part of the instrument. Depending on what is being measured, samples will be prepared and handled differently.

Analyzers are made for both stress (force) and strain (displacement) control. In strain control, the sample is displaced at a given rate and the resulting stress of the sample is measured. The advantages of strain control

include a better short time response for materials of low viscosity and experiments of stress relaxation are done with relative ease. In stress control, a set force is applied to the same and several other experimental conditions (temperature, frequency, or time) can be varied. Stress and strain can be applied via torsional or axial analyzers. Common geometries and fixtures for axial analyzers include three-point and four-point bending, dual and single cantilever, tensile and shear plates and sandwiches.

The curve presented in Figure 4.27 is a stress-strain curve typical of a superelastic SMA. The characteristic mechanical behavior of a superelastic alloy can be recognized, including the initial elastic deformation in austenitic phase up to σ_{Ms} , the plateau relative to the SIM transformation between ϵ_{Ms} and ϵ_{Mf} , the subsequent elastic and plastic deformation in martensitic phase and the very low residual deformation after unloading.

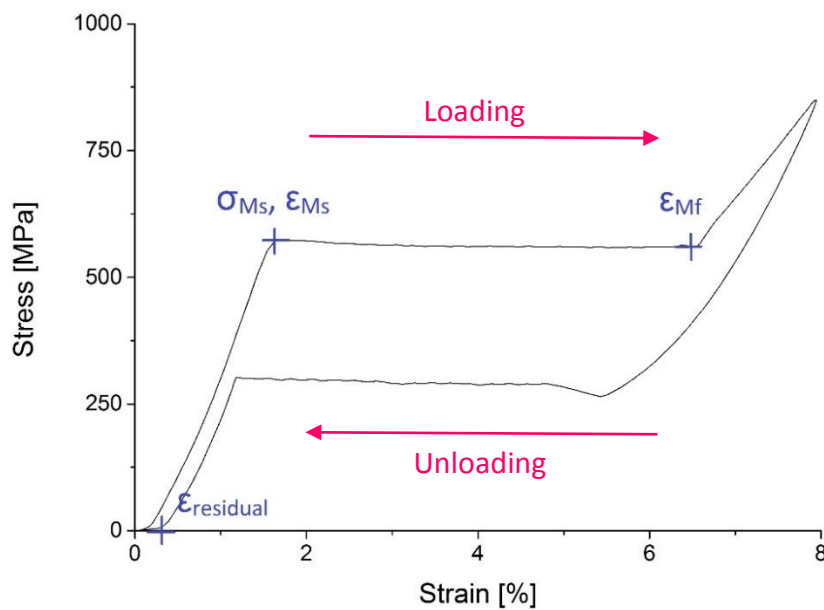


Figure 4.27 Typical stress-strain curve for a generic superelastic Nitinol SMA at room temperature.

The model of DMA used in this work is Q800 produced by TA Instruments (Figure 4.28) equipped with *gas cooling accessory* (GCA) which uses cold nitrogen gas generated from controlled heating of liquid nitrogen. The main characteristics of the DMA system are listed in Table 4.11. The Q800 features a variety of sample clamps that provide for multiple modes of

deformation. In this work, tensile fixture are used, suitable for both films and fibers. In this mode, the sample is placed in tension between a fixed and moveable clamp.

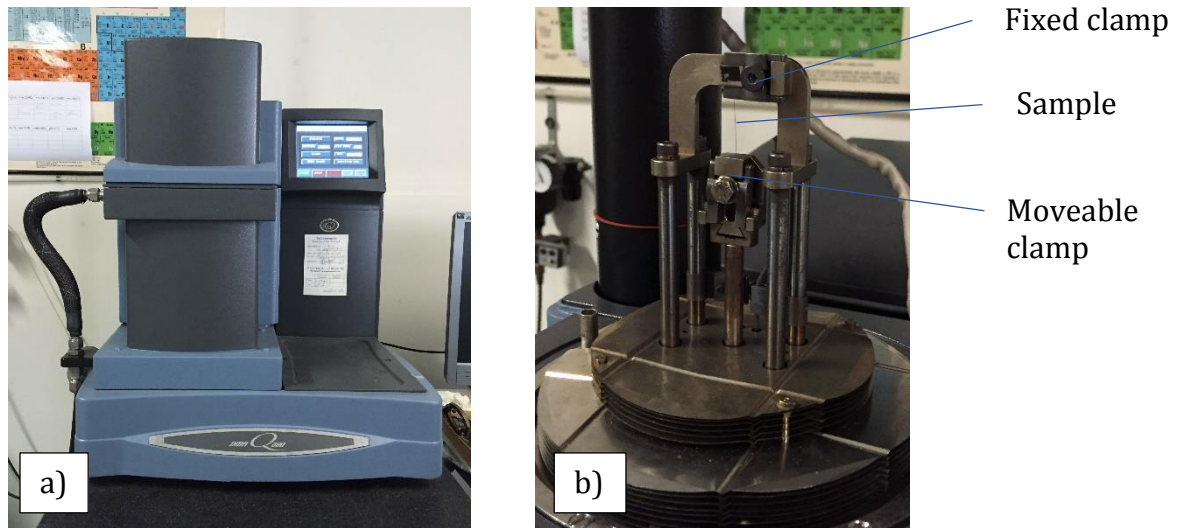


Figure 4.28 DMA used in this work, model Q800 TA Instruments, (a) and detail of the clamps with the wire inserted (b).

Temperature range	From -150 to 600 °C
Maximum force	18 N
Force resolution	0,00001 N
Deformation mode	Tension
Sample length	5 to 30 mm

Table 4.11 Main characteristics of the DMA system used in the analysis.

Two types of mechanical tests are performed on each material condition. The first one is a stress-strain test at room temperature. The wire is fixed between clamps with a free length equal to 20 mm. Then it is subjected to mechanical cycle composed of two subsequent steps: strain controlled uniaxial loading at a rate of 1%/min up to a total percentage of deformation able to show the entire superelastic plateau of the material, and complete unloading at the same rate with recording of the residual strain. Each test is

conducted at a controlled temperature equal to 25 °C. The second type of test is the mechanical cycling, which consist of 50 repeated identical loading and unloading cycles to investigate the stability of the mechanical response of the material. In this case, the maximum deformation imposed for each cycle is equal to 4% to simulate a likely working condition for the wire. Indeed, superelastic Nitinol components in most engineering applications experience mechanical cycles, so it become essential to realize that the functional properties must not only be set as required, but also must be stable during cycling.

4.4.3 Metallographic analysis

The internal structure of the material in the analyzed conditions is observed using a light microscope from Leica, model Aristomet (Figure 4.29).

With this instrument it is possible to reach a magnification up to 1000x of the surface under analysis, so a good examination of the evolution of the material structure for the two considered technologies can be performed. In particular, the aim of these observations is the characterization of the qualitative trends present in the material owing to the parameter variation in terms of grains dimension, shape and appearance, as well as preferential orientation of the texture.

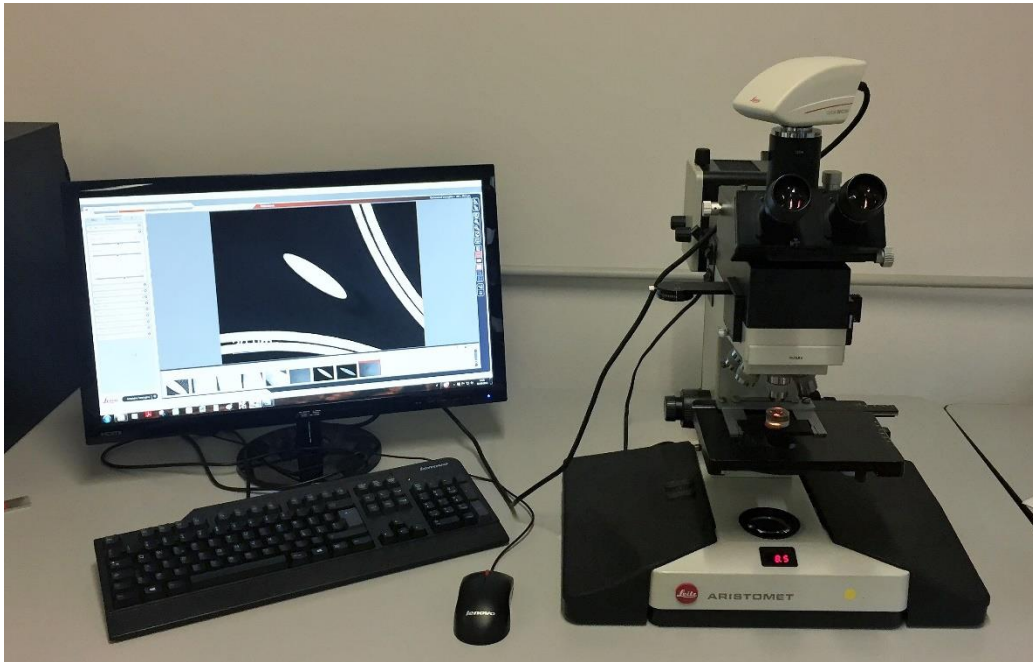


Figure 4.29 Optical microscope utilized in this work (Leica, mod. Aristomet).

Before the microscopic observation, the samples are mounted in a cold two-part EpoFix resin with a special support realized with the 3D printer (Figure 4.30 (a)) to help the wire positioning with the same orientation and angle. An angle of 10° is selected to allow the analysis of a tilted section of the wire, so to gain qualitative information about the microstructural variations along the drawing direction of the wire. An example of wire section observed in this characterization step is reported in Figure 4.30 (b). All the samples are placed with the drawing direction parallel to the horizontal direction to simplify the comparisons.

The surface preparation is carried out with a manual lapping machine (model FORCIPOL 1V from Metkon) (Figure 4.30 (c)) and includes two steps:

- rough grinding with silicon carbide abrasive papers of 320, 600, 800 and 1200 grit in sequence for the initial material removal;
- fine polishing using polishing cloths with diamond grit suspension with abrasive particles of size 6, 3 and $1\ \mu\text{m}$ to produce a mirror finish.

After every step, the samples are subjected to ultrasonic cleaning in ethyl alcohol to remove the extraneous particles.

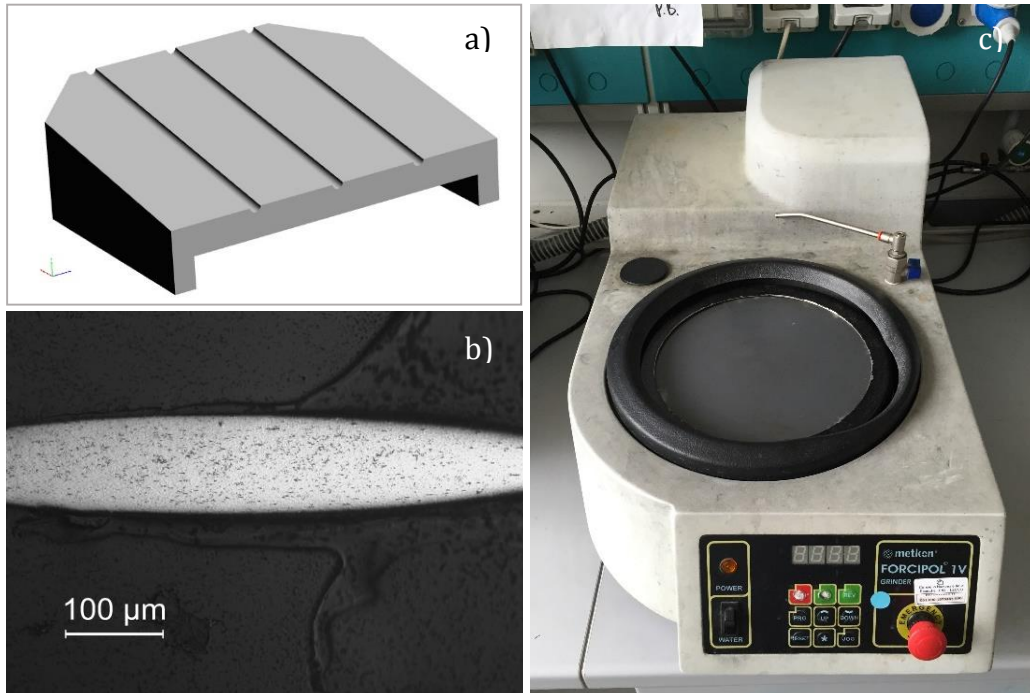


Figure 4.30 3D printed support for samples (a), section of a 100µm wire seen by the light microscope (b) and lapping machine used for the sample preparation (c).

In order to reveal the microstructure of the polished surface for the metallographic analysis, a chemical etching of the sample surface is carried out in an acid solution composed by HF at 3 % vol., HNO₃ at 12 % vol. and H₂O for the remaining part. The duration varies from sample to sample, approximately in the range from 30 to 50 seconds. The reagent, corroding in a selective way the most reactive phases, highlights the structure of the material.

CHAPTER 5:

5 Analysis of results and discussion: furnace annealing

The characterization of the furnace annealed wires shows a strong dependence of the material behavior on the annealing temperature, being equal the annealing time, as already seen in many researches as the one by Huang et al. [Huang, 2001]. As expected, the best treatment conditions are found in the range between 400 and 500 °C: for lower temperature, the energy given to the sample is not sufficient to induce the proper microstructure needed for showing superelasticity, while for temperatures exceeding 600 °C the mechanical response is not stable because the material is completely recrystallized. In addition, it can be stated that the increase in the wire diameter taken into account in this work does not affect the material calorimetric behavior in a massive way. The trends identified for these samples are mainly consistent with the information found in the literature and will be used to help the understanding of the phenomena that underlies the annealing of Nitinol.

In the following, cold worked wires annealed in furnace at temperatures equal to 300, 400, 450, 500, 550, 600, 650, 700 and 800°C are called FA 300 °C, FA 400 °C, FA 450 °C, FA 500 °C, FA 550 °C, FA 600 °C, FA 650 °C, FA 700 °C and FA 800 °C sample respectively.

5.1 Calorimetric analysis

The DSC curves of the 100 μm and 200 μm diameter Nitinol wires treated in furnace at the various temperature are presented in Figure 5.1 and 5.2 respectively, with increasing annealing temperatures starting from the top. As a reference condition, also the calorimetric response for the cold worked wire is presented in the same figure for both diameters.

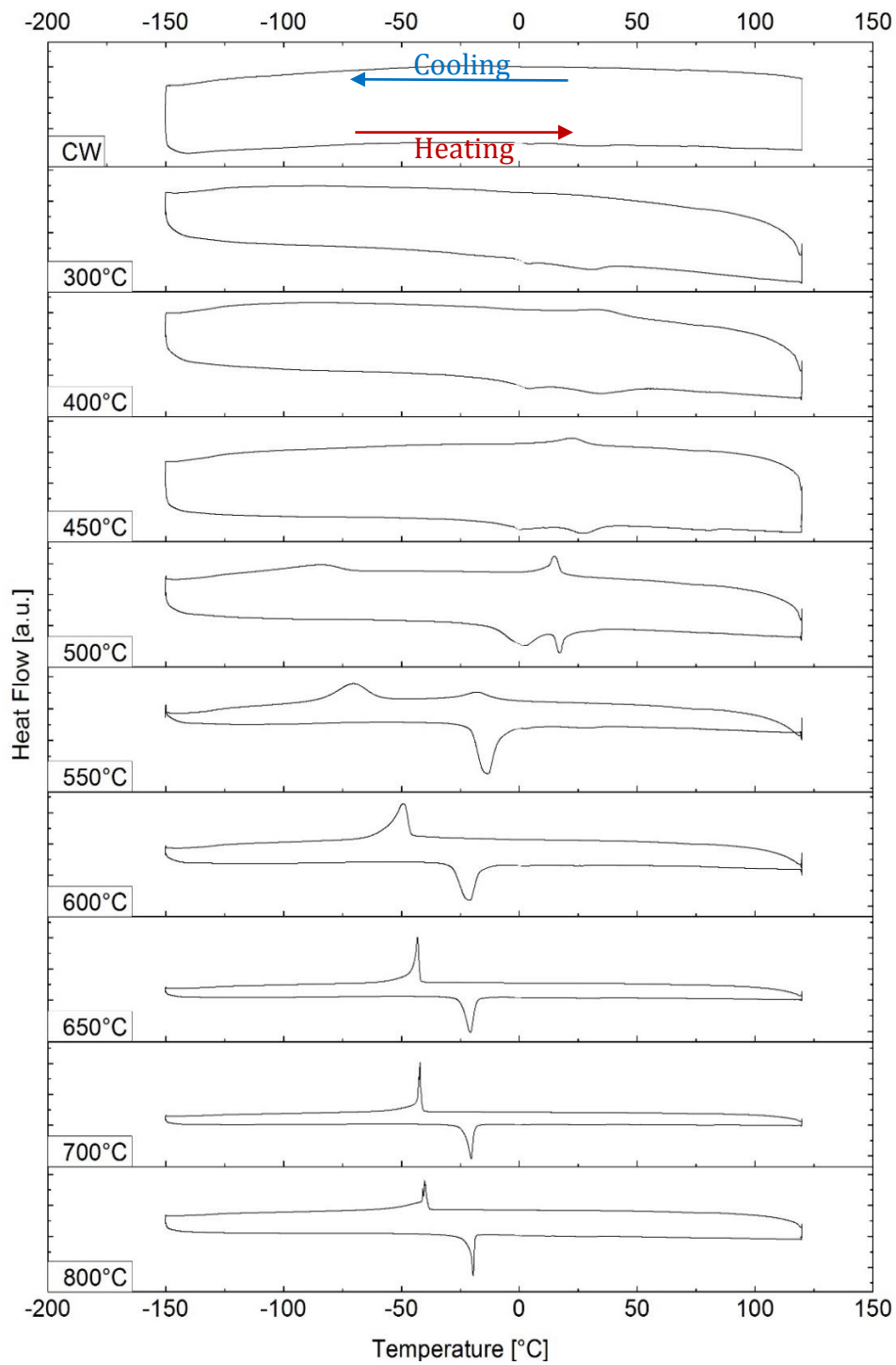


Figure 5.1 Evolution of the calorimetric response of the 100 μ m wire, starting from the cold worked condition (top) to the furnace annealed material, treated at 300, 400, 450, 500, 550, 600, 650, 700 and 800°C (bottom).

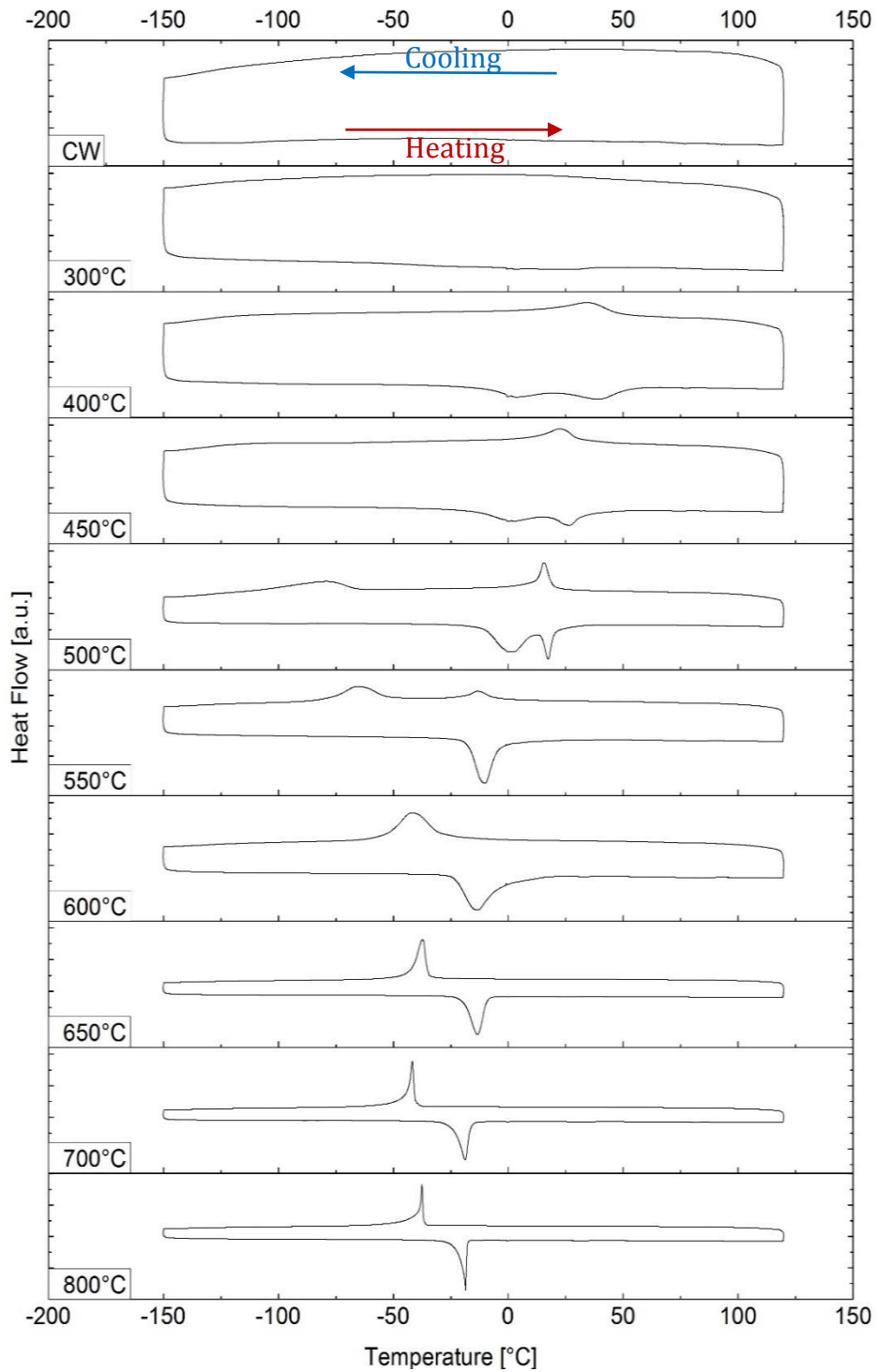


Figure 5.2 Evolution of the calorimetric response of the 200 μm wire, starting from the cold worked condition (top) to the furnace annealed material, treated at 300, 400, 450, 500, 550, 600, 650, 700 and 800°C (bottom).

Matching the DSC curves obtained for analogous conditions for the 100 μm and 200 μm wires, it is possible to observe comparable results, indeed calorimetric response are very similar. Being the treatment temperature the same, effects of furnace annealing are nearly the same for both wire sizes.

The cold worked wire before the heat treatment showed no peaks, while small and wide peaks starts to appear in the conventional heat treated wires annealed at the lower temperatures, due to the restoration of the martensitic transformation.

The lower temperature tested for the treatment is 300 $^{\circ}\text{C}$: while in the smaller size of wire the transformation temperatures are hardly detectable in the DSC curve because the peaks are not well visible yet, with the bigger size of the wire it is absolutely not possible to identify them. This sample presents a behavior comparable to the behavior of the wire in the cold worked condition, without visible transformation peaks. It means that for the 200 μm diameter wire, being the annealing time the same, a slightly higher temperature is required to obtain an identical calorimetric response with respect to the 100 μm diameter one. Despite this slight difference in the results for the 300 $^{\circ}\text{C}$ samples, we can conclude for both wire diameters that the temperature of the heat treatment for the selected time is not sufficiently high to guarantee a good functionality of the alloy. On the contrary, transformation peaks can be easily distinguished in the other curves, starting from 400 $^{\circ}\text{C}$ annealing.

In general, increasing the heat treatment temperature, the peaks of martensite and austenite transformation become more narrow and sharp and they progressively get closer one each other. The trend of the range of temperature of the peaks can be observed more clearly in Figure 5.3, where the width of each transformation, calculated as the difference between start and end temperature of transformation, is reported for the 100 μm diameter wire. A lower temperature range means that the transformation from one phase to another phase will occur faster, and therefore the material is more homogeneous during the heating and cooling cycles.

The evolution of the characteristic temperatures of transformation start and finish for martensite (M_s and M_f) and R-phase (R_{cs} and R_{cf}) upon cooling

is reported in Figure 5.4 and 5.5 respectively, while for austenite (A_s and A_f) and R-phase (R_{hs} and R_{hf}) upon heating this trend is represented in Figure 5.6 and 5.7. In all the figures, the corresponding temperature value for the straight annealed wire is shown.

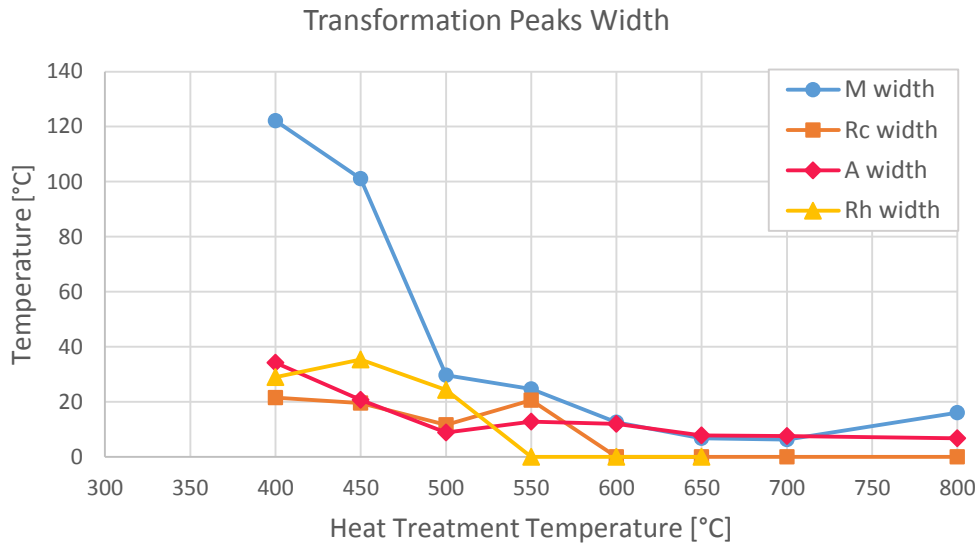


Figure 5.3 Evolution of the peak width of the martensite and R-phase transformations upon cooling and austenite and R-phase transformations upon heating for the 100 μm wire as a function of the furnace annealing temperature.

Austenite finish temperature A_f is of particular relevance in the determination of the material behavior in terms of superelasticity, because it dictates the transition between shape memory and superelastic properties [Russel, 2000]. It can be clearly observed from Figure 5.4 that A_f lowers increasing the heat treatment temperature, going under room temperature for furnace annealing performed at more than 500 °C. This indicates that the material in these conditions has a complete superelastic behavior at room temperature. For most of the superelastic components applications, being them in the biomedical field, the material is required to be completely in austenitic phase in the human body environment [Duerig, 1999; Morgan, 2004; Petrini, 2011; Spini, 2014], so the A_f must be referred to the body temperature and the upper limit is expanded to around 37 °C. For this purposes, all wires exhibit a suitable range for the austenite transformation, with the exception of the 400 °C sample.

Some of the curves show a two-stage transformation on heating and on cooling. In particular, we can observe austenite transforming into R-phase and then R-phase transforming into martensite upon cooling ($A \rightarrow R \rightarrow M$) for the wires annealed at 300, 400, 450, 500 and 550°C, and the reverse two-step transformation on heating ($M \rightarrow R \rightarrow A$) for wires annealed at 300, 400, 450 and 500 °C. For higher temperatures of the heat treatment, the R phase is not present, since its transformation peak is completely overlapped with the martensitic one upon cooling and the austenitic one upon heating. In these cases, we obtain a single peak transformation ($A \rightarrow M$ and $M \rightarrow A$). Figure 5.5 and 5.7 represent the evolution of the R-phase temperatures upon cooling and heating for the annealing conditions for which this transformation is present.

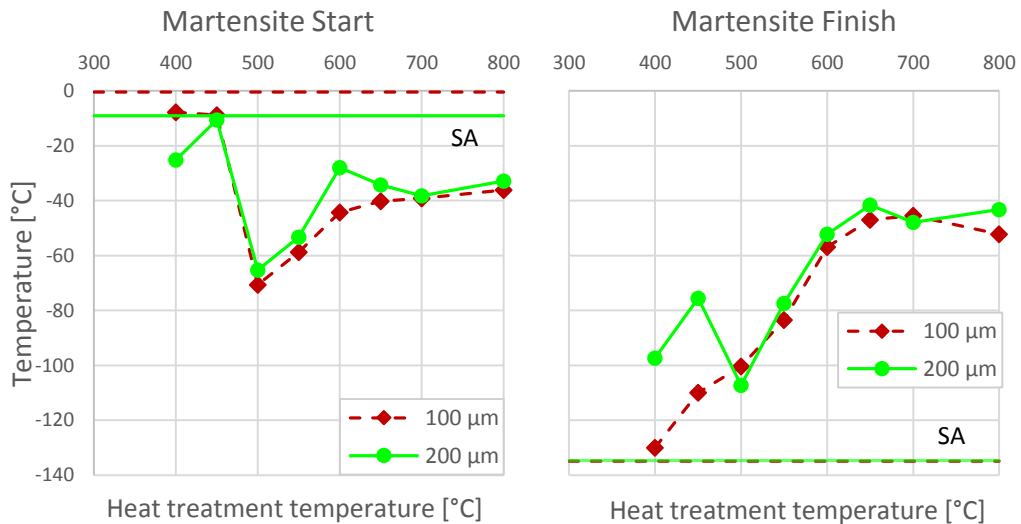


Figure 5.4 Martensite characteristic temperatures upon cooling: martensite start (left) and martensite finish (right). The straight lines are the corresponding characteristic temperatures for the straight annealed wires.

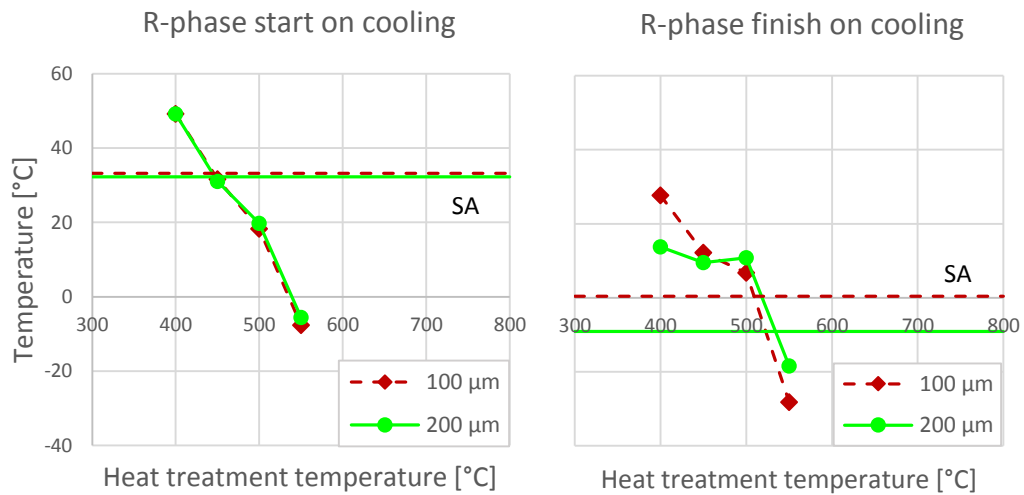


Figure 5.5 R-phase characteristic temperatures upon cooling: R-phase start (left) and R-phase finish (right). The straight lines are the corresponding characteristic temperatures for the straight annealed wires.

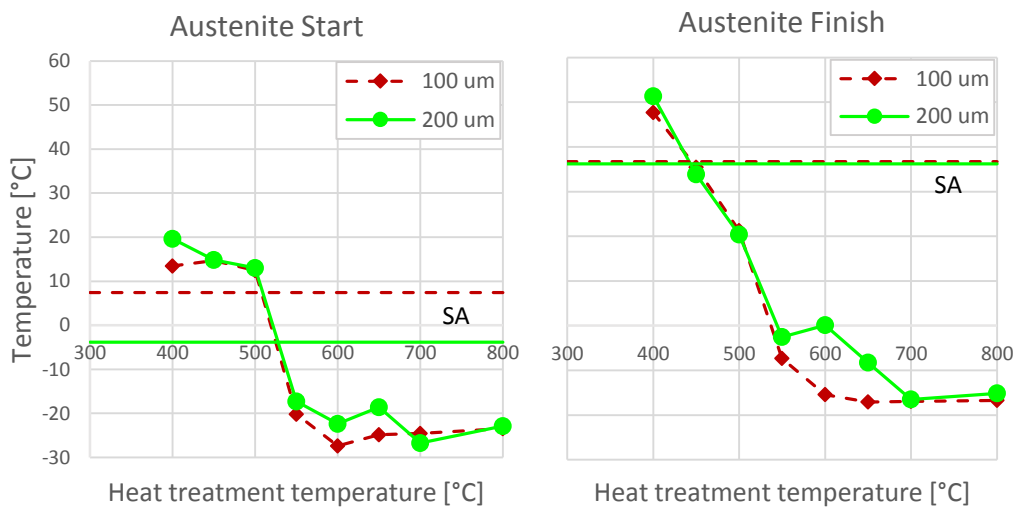


Figure 5.6 Austenite characteristic temperatures upon heating: austenite start (left) and austenite finish (right). The straight lines are the corresponding characteristic temperatures for the straight annealed wires.

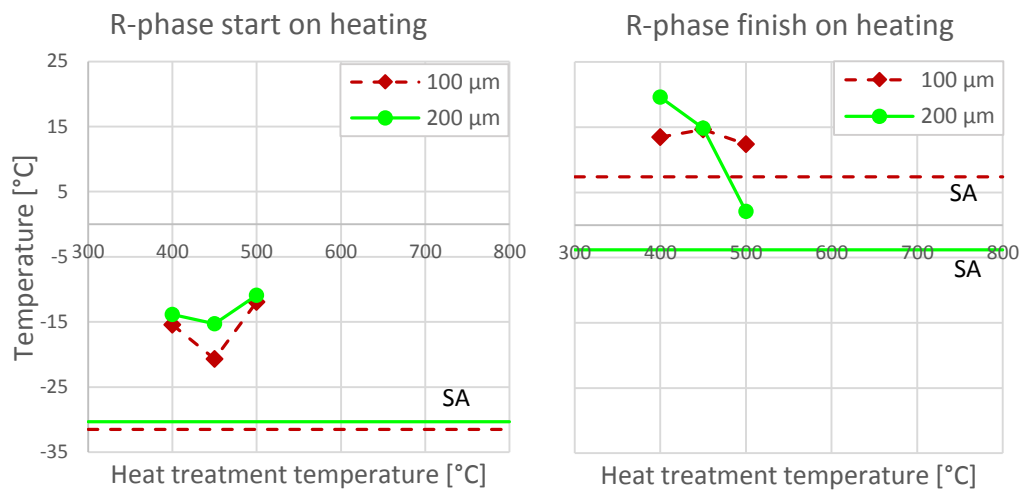


Figure 5.7 R-phase characteristic temperatures upon heating: R-phase start (left) and R-phase finish (right). The straight lines are the corresponding characteristic temperatures for the straight annealed wires.

Starting from a heat treatment temperature of 600 °C, the solubilization of the material can be noticed. This phenomenon is due to the recrystallization of the alloy, which occurs for soaking at high temperatures during the heat treatment. From a calorimetric point of view, this condition is characterized by very narrow and elongated peaks. This means a great homogeneity of the material, which transforms in a very reduced range of temperatures, smaller than 15 °C. Furthermore, for the wires treated at 700 °C and 800 °C, the martensitic transformation presents jagged peaks, as shown in Figure 5.8 (b). On the contrary, in all other conditions transformations appear in the DSC curves as single peak, as represented in Figure 5.8 (a). Looking again at the evolution of the peaks width in Figure 5.3, it is possible to notice a discontinuity in the negative trend of the transformation temperatures on both heating and cooling, with values that become almost stable increasing the annealing temperature above 600 °C, again due to the solubilization phenomenon.

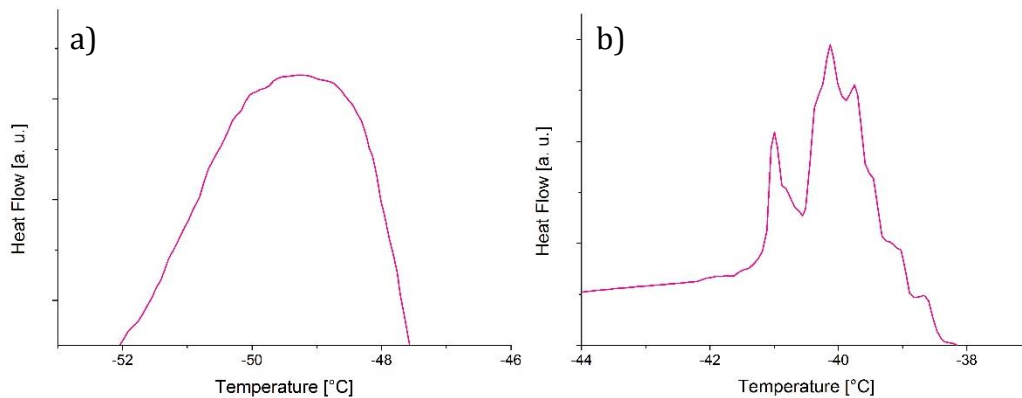


Figure 5.8 Comparison between the shapes of the martensitic transformation peak for the 600°C furnace annealed sample (a) and the 800°C furnace annealed sample (b).

The enthalpy or latent heat of transformation of R-phase and martensite upon cooling (Figure 5.9 (left)) and R-phase and austenite upon heating (Figure 5.9 (right)) is reported as a function of the annealing temperature. It is possible to recognize a progressive increase of the enthalpy values correlated to the increase of the annealing temperature, as previously seen by Miller et al. [Miller, 2001]. This is because the dislocations associated with the high levels of plastic deformation that characterize the CW material generate an internal stress state that restricts the martensite from transforming into austenite. This martensitic phase remains ‘pinned’ in the microstructure until the dislocations are removed through an annealing process. Therefore, the generation of the ‘pinned’ martensitic microstructure reduces the latent heat of transformation because of less material undergoing the transformation, and this effect is progressively removed as the annealing temperature increases, causing as a consequence an increase of the transformation enthalpy. This positive trend is maintained until the complete recrystallization is reached at 600 °C, condition in which the maximum enthalpy value is found [Miller, 2001], then enthalpy values start to drop for the higher treatment temperatures.

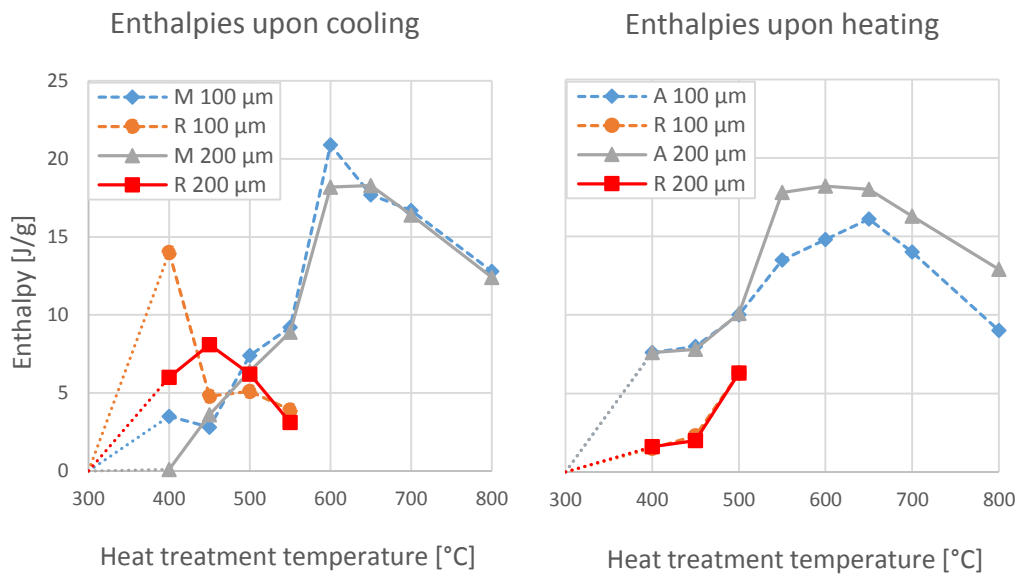


Figure 5.9 Transformation enthalpies of R-phase and martensite upon cooling (left) and R-phase and austenite upon heating (right).

With respect to the straight annealed wire behavior, major similarities in the calorimetric response can be found for the 450 °C annealed wires. The comparison between the corresponding DSC curves is shown in Figure 5.10 for the 100 μm wires. The main detectable difference is that in the commercially treated wire the R-phase peak is not visible upon heating, but the temperature ranges of austenite and martensite transformations are very close for the two considered conditions.

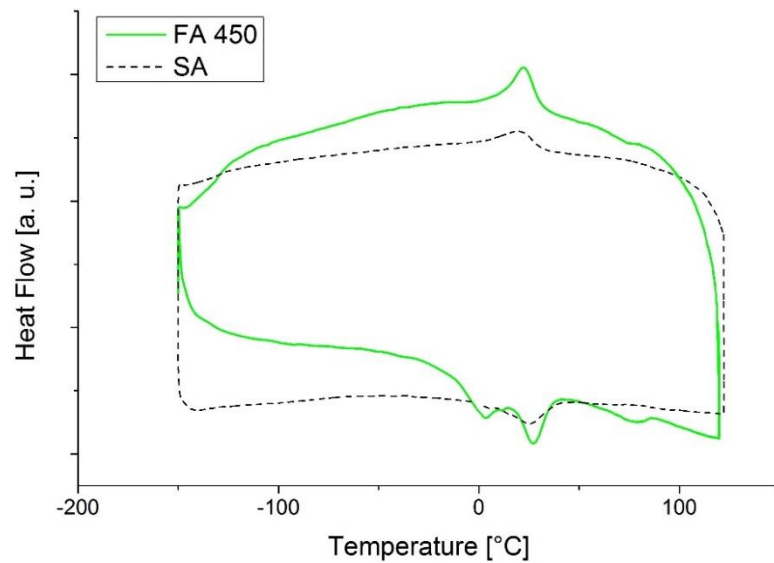


Figure 5.10 Comparison between DSC curves of the 100 μm 450 °C furnace annealed wire and the 100 μm straight annealed wire.

5.2 Mechanical analysis

Figure 5.11 and 5.12 show the stress-strain curves obtained for the 100 μm and 200 μm diameter wire annealed in furnace. The maximum value of deformation imposed to the material during the test was set through preliminary tests in order to show the entire superelastic plateau of the material and the subsequent unloading. This procedure was necessary to gain information about the mechanical behavior of the alloy in the different conditions in terms of plateau stress and strain, mechanical hysteresis and residual deformation.

The DMA curves for the 200 μm wire cold worked and treated at 300 °C are not complete due to a limit of available instrumentation, but from the initial part of the two curves we can confirm a calorimetric behavior in accordance with DSC results for this wire and DMA result for the lower size of the wire.

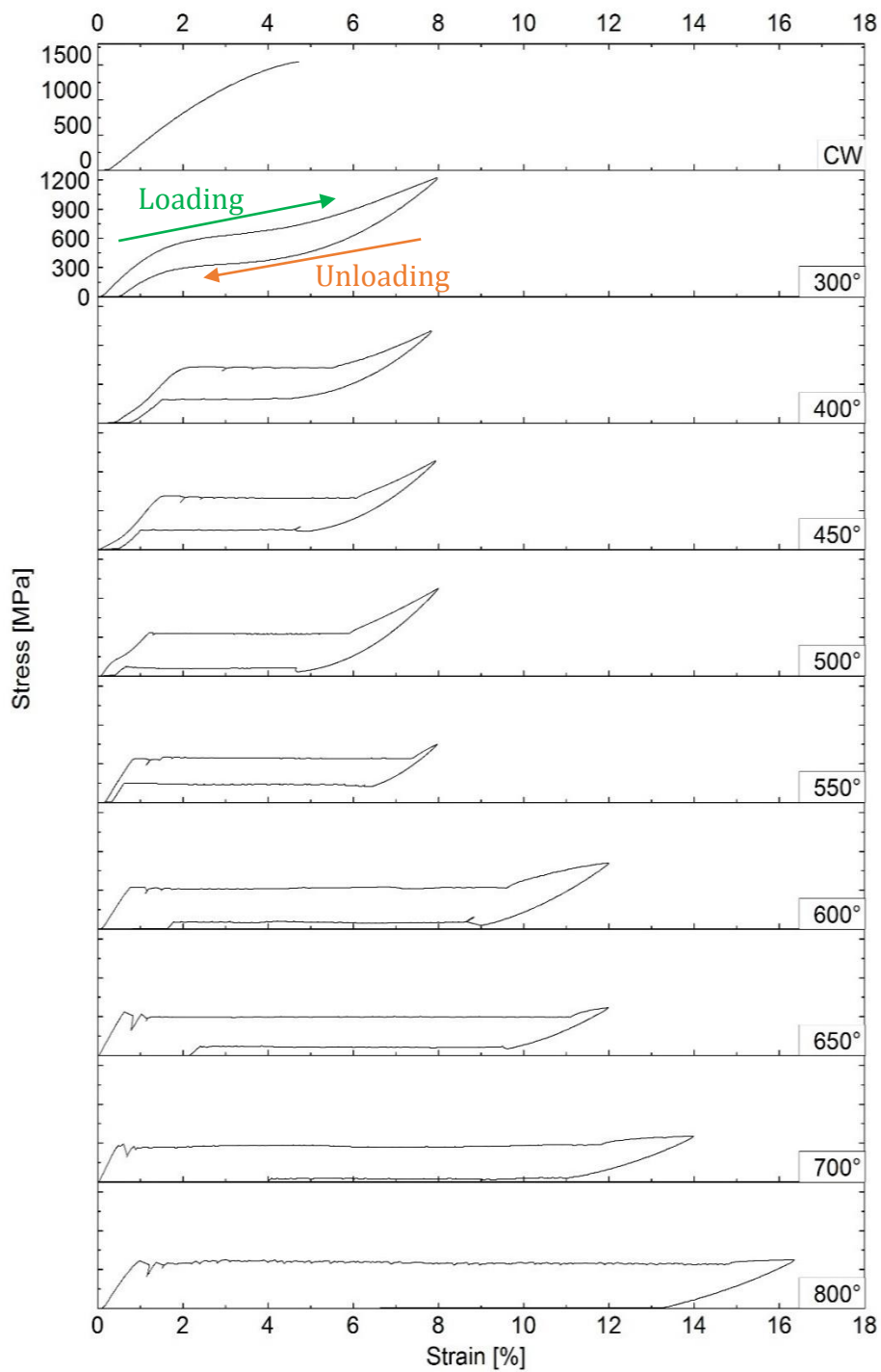


Figure 5.11 Evolution of the stress-strain response of the 100µm wire, starting from the cold worked condition (top) to the furnace annealed material, treated at 300, 400, 450, 500, 550, 600, 650, 700 and 800°C (bottom).

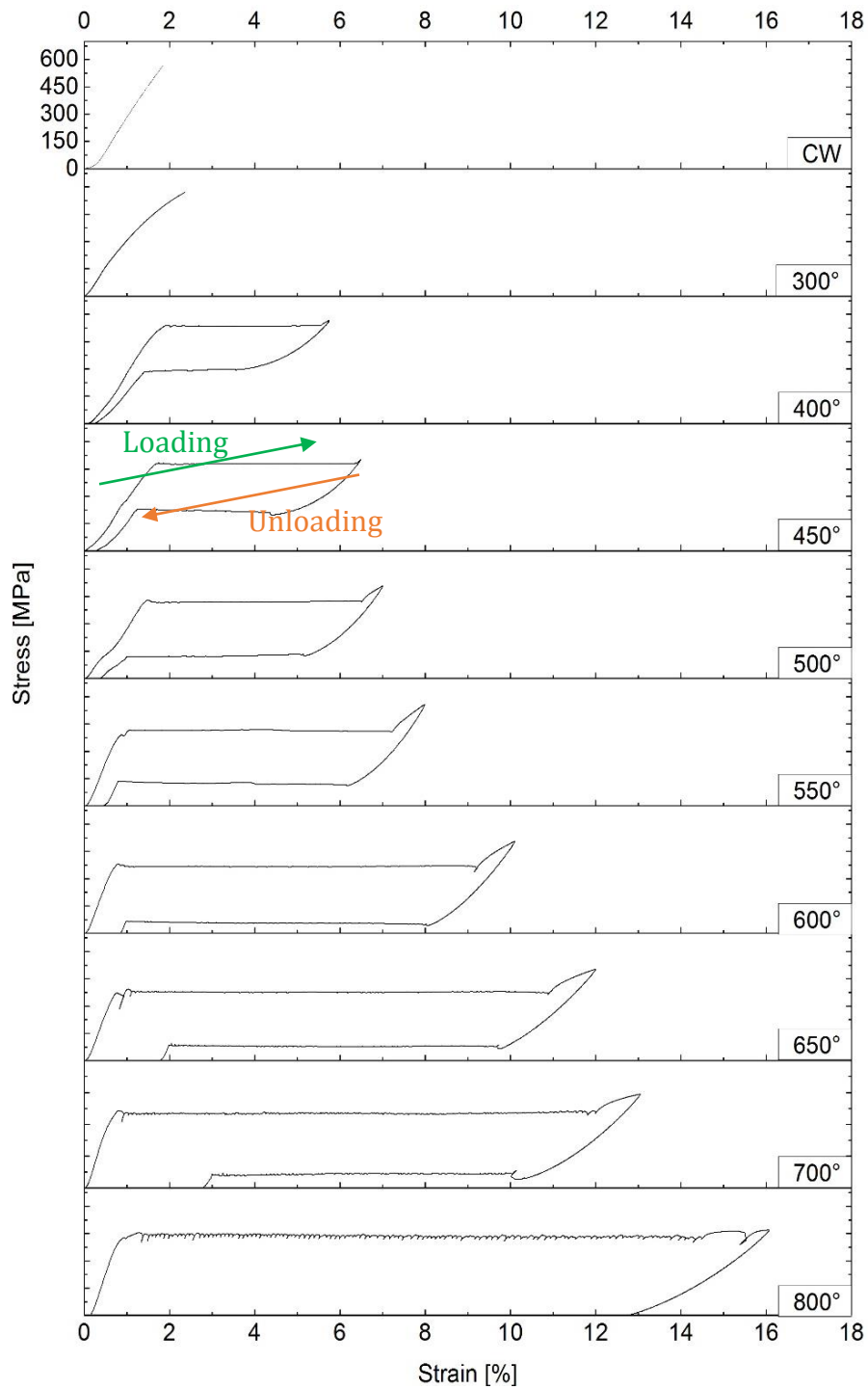


Figure 5.12 Evolution of the stress-strain response of the 200µm wire, starting from the cold worked condition (top) to the furnace annealed material, treated at 300, 400, 450, 500, 550, 600, 650, 700 and 800°C (bottom).

The mechanical response of the wires confirms the previous observations based on the calorimetric behavior. Also these analysis proves that the treatment carried out at 300 °C is not able to give the required functional properties to the material, while starting from the annealing at 400 °C it is possible to recognize the characteristic superelastic flag. As visible in Figure 5.13 and 5.14, the loading plateau length increases with the increase of the annealing temperature, while the plateau stress decreases at the same time. However, the elongation of the loading plateau means an increase of the residual strain, which become too high for wire treated at more than 600 °C, causing a progressive loss of the superelastic properties. The mechanical hysteresis follows a slightly positive trend for increasing annealing temperatures, but substantial differences among the various conditions are not observed. Conditions between 450 °C and 550 °C seems to own the better performances, both in terms of residual strain and loading plateau.

Also for the mechanical response, it is possible to detect in the 450 °C annealed wire, the major similarities with the straight annealed wire. The two conditions for the 100 μm wires are overlapped in Figure 5.15 for an easier comparison.

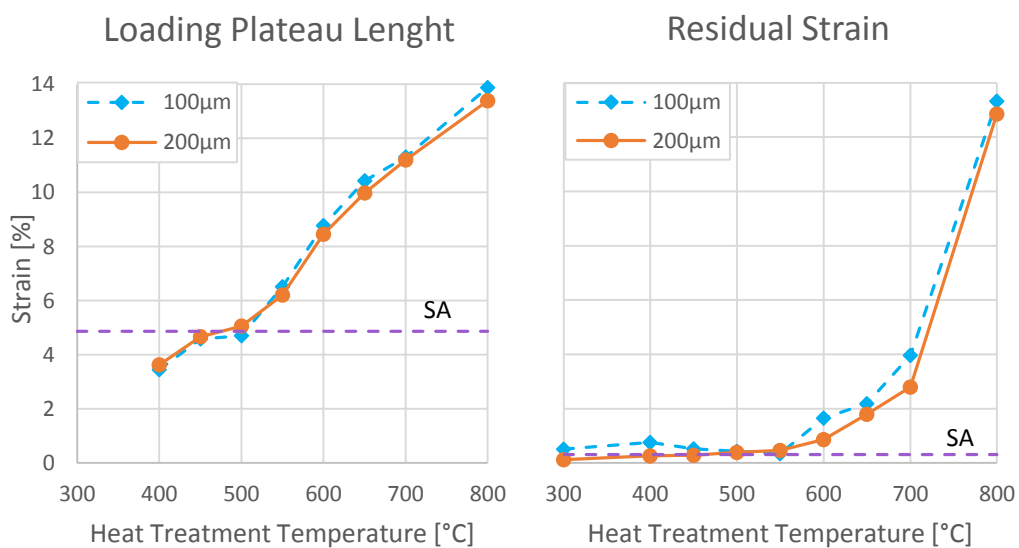


Figure 5.13 Length of the superelastic plateau upon loading phase (left) and residual strain after the first loading/unloading cycle (right). The straight lines correspond to the strains measured for the 100μm straight annealed wire (data for the 200μm wire are not available).

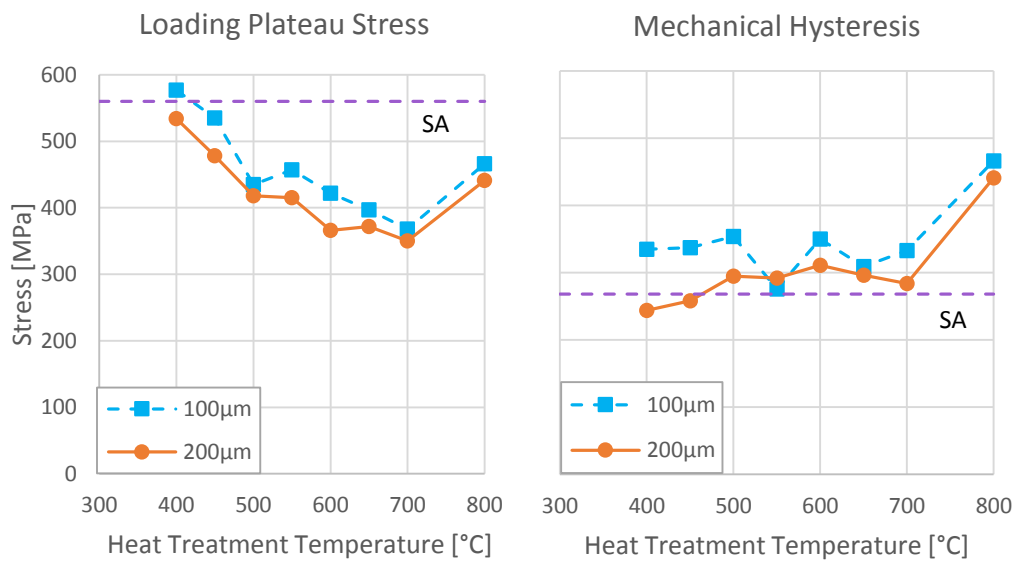


Figure 5.14 Stress value of the superelastic plateau upon loading phase (left) and mechanical hysteresis of the first loading/unloading cycle (right) measured at 3% strain. The straight lines correspond to the stresses measured for the 100µm straight annealed wire (data for the 200µm wire are not available).

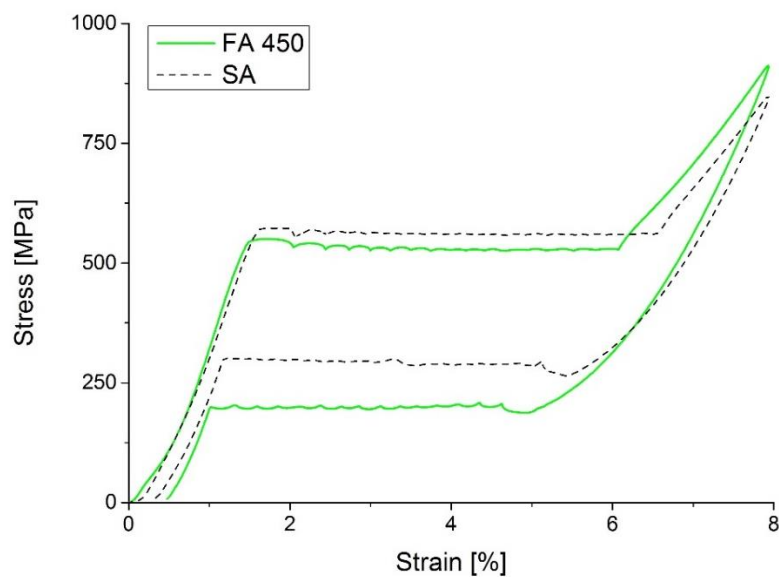


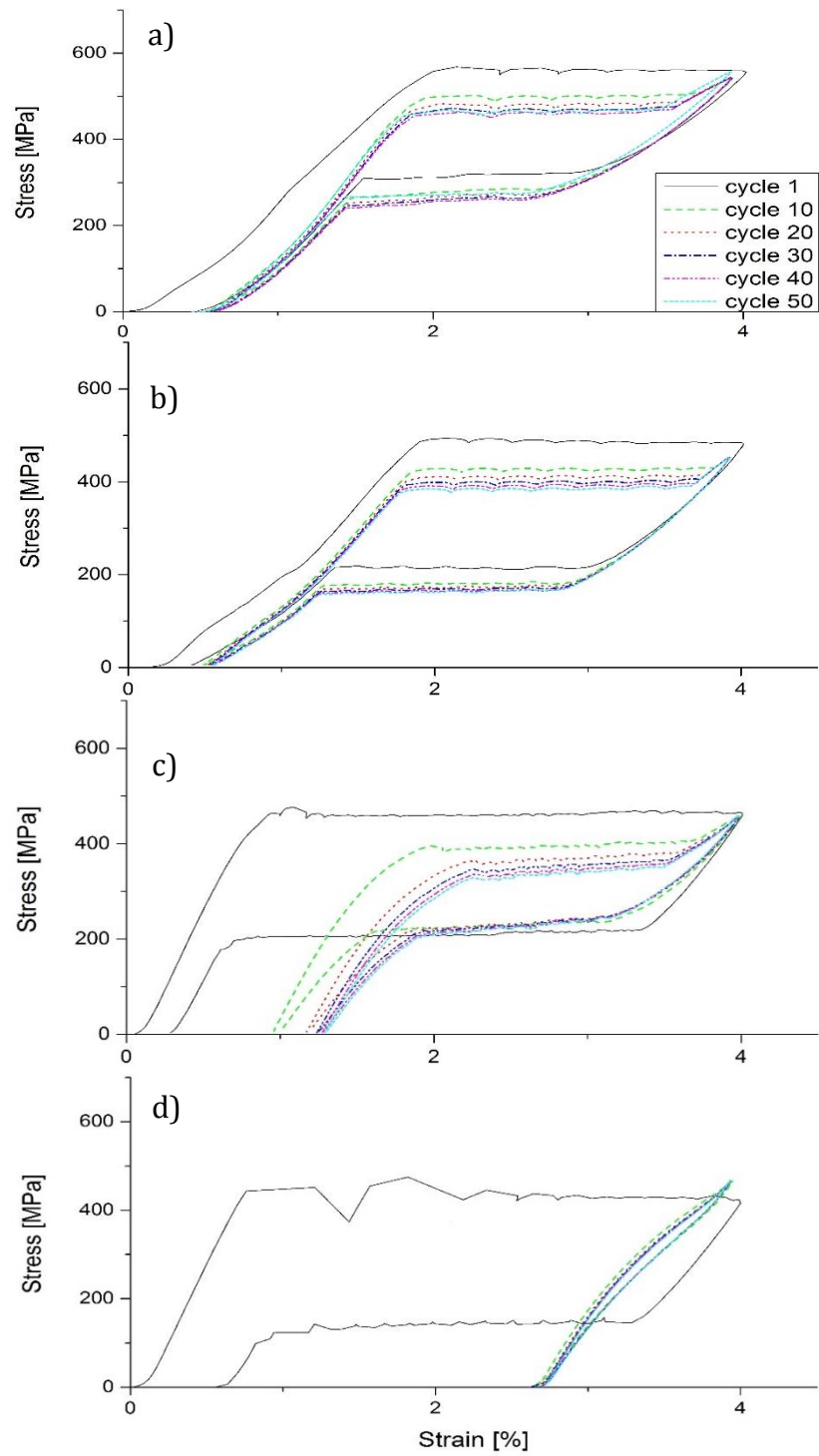
Figure 5.15 Comparison between stress-strain curves of the 100 µm 450 °C furnace annealed wire and the 100 µm straight annealed wire.

5.3 Mechanical cycling

Mechanical cycling tests up to 4% strain are conducted on 400, 450, 550 and 650 °C furnace annealed 100 μm wire to investigate the stability of the mechanical behavior for the conventionally treated wire. The stress-strain curves obtained for the cycle 1, 10, 20, 30, 40 and 50 for the four samples are presented in Figure 5.16. From a qualitative point of view, it is possible to recognize a better stability of the stress-strain response for the two wires treated at lower temperatures, while in the remaining conditions the shape of the superelastic plateau undergoes considerable modification starting from the earlier cycles.

For all analyzed conditions, with the exception of the last case in which the plateau immediately disappears, both the loading and unloading plateau stresses lower during the cycling. The evolution of the mechanical hysteresis measured at a strain level of 2,5% is reported in Figure 5.17 as a function of the number of the mechanical cycles carried out on the material, together with the corresponding trend found for the SA sample. The hysteresis value is maximum for the FA 400 °C sample and very low for the FA 550 °C one, and for all annealing temperatures it decreases during cycling. It can be observed that the trend found for the FA 450 °C wire is really close to the SA wire one.

The choice of this behavior as optimal, instead of the condition with the lower mechanical hysteresis, is justified on the basis of the observation of the residual strain accumulated after the unloading phase. This value is found to be very high for the FA 550 and FA 650 °C samples, so these wires do not exhibit acceptable functional properties. This is confirmed by Figure 5.18, which shows the amount of recoverable strain obtained during the cycling test. The FA 400 and FA 450 °C samples own high and comparable amounts of recoverable strain, but a better performance is observed in this case in the SA wire.



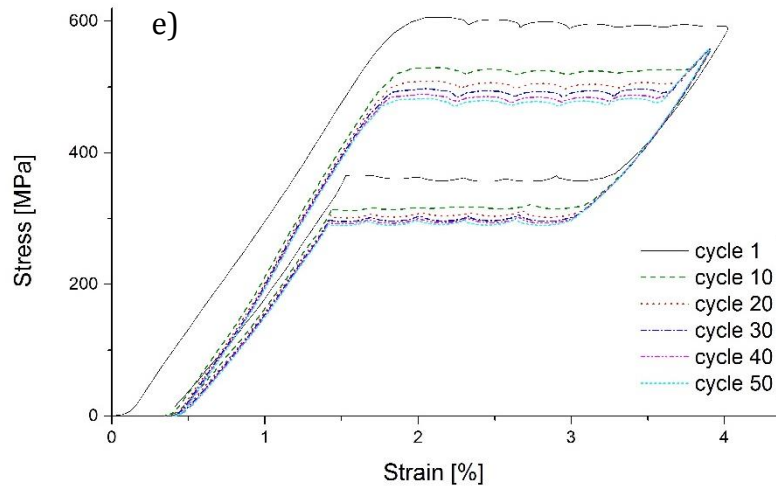


Figure 5.16 Stress-strain curves acquired at cycle 1, 10, 20, 30, 40 and 50 for the wire treated at 400 (a), 450 (b), 550 (c) and 650°C (d) and for the SA wire (e) loaded up to 4% strain.

Concerning the stability of the response, the value of recoverable strain for the FA 400 and FA 450 °C samples is almost constant from the first cycle, while, after about 10 cycles for the 650 °C treated wire and 25 cycles for the 550 °C treated wire, no further permanent strain is accumulated. On the contrary, after 50 cycles the mechanical hysteresis still maintain a negative trend for all examined samples.

From the mechanical cycling characterization, it can be concluded that, despite the treatments conducted at high temperature are those that lead to a greater homogeneity of the calorimetric behavior of the material and to a longer superelastic plateau, these conditions do not occur as optimal due to the instability of the response of the material observed through mechanical cycling tests. This behavior can be attributed to the solubilization of the material and the consequent loss of the functional properties of the wire.

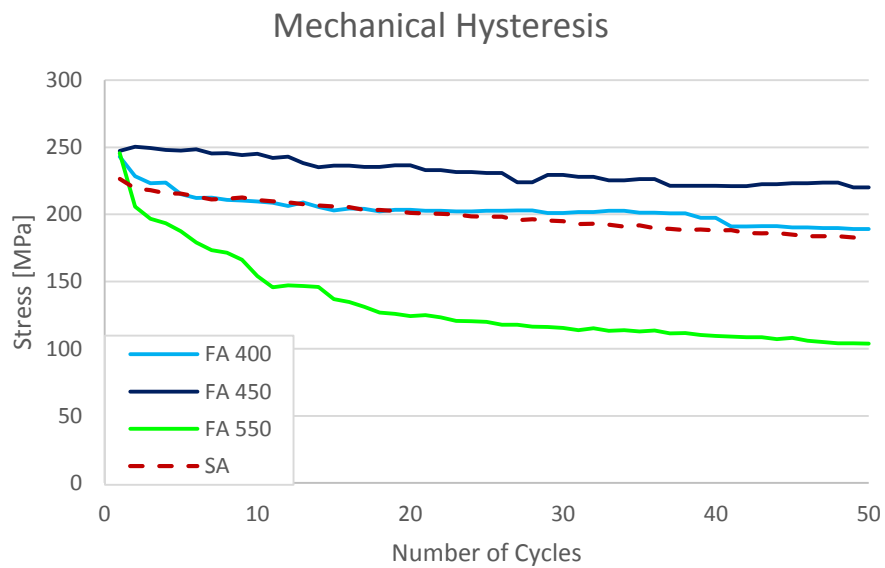


Figure 5.17 Evolution of the mechanical hysteresis measured at 3 % strain as a function of the number of cycles for the furnace annealed wires. The dashed line represents the corresponding trend for the straight annealed wire.

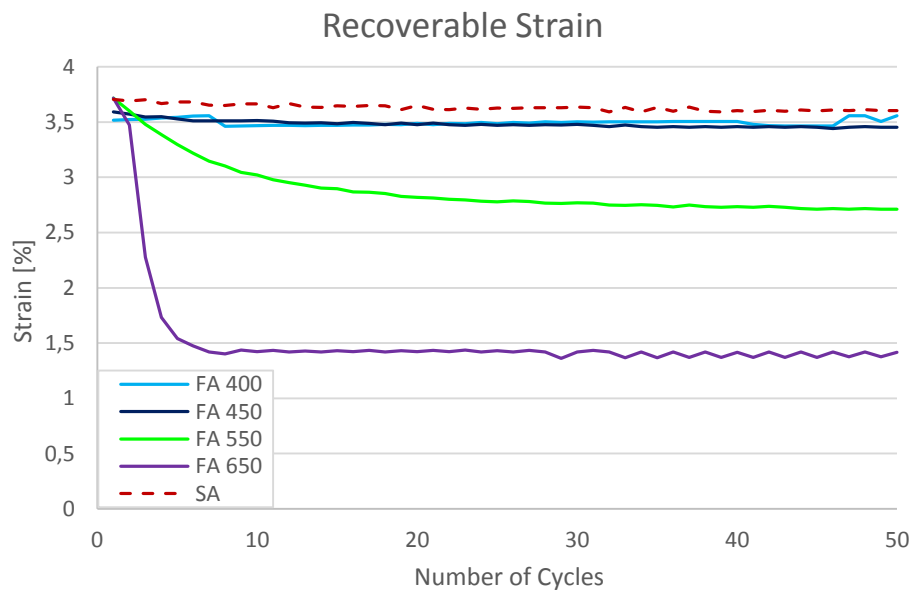


Figure 5.18 Evolution of the recoverable strain as a function of the number of cycles for the furnace annealed wires. The dashed line represents the corresponding trend for the straight annealed wire.

5.4 Metallographic analysis

The microstructure observation of the furnace annealed samples is performed with the optical microscope at room temperature. In Figure 5.19 the main types of morphology observed for the sample with diameter 200 μm are reported to show the general evolution of the microstructure varying the annealing temperature. In general, the progressive increase in the degree of annealing led to a gradual disappearance of the martensitic phase induced by the cold working, as well as new grains formation and coarsening and decrease of the precipitates density, because the temperature at which the material is subjected cause in the alloy the phenomena of recovery and then recrystallization [Meng, 2012]. More in detail, all conditions are reported at the highest magnification in Figure 5.20, 5.21 and 5.22. The steps of the microstructural evolution are the same for both diameters of wire, as assumed on the basis of the previous characterizations.

The microstructure detected for the starting material, subjected to severe cold drawing, is reported in Figure 5.20. Besides the suppression of the superelastic properties of the alloy, the cold working of the material raises the strength and decreases the ductility, leading to lower recoverable strain due to the introduction of random dislocations into the material. Annealing treatment after cold working is performed in order to overcome this issues, being able to diminish the effects of the previous plastic deformations and to restore the functional properties of SMA, thanks to a rearrangement of dislocations, followed by a decrease of the strength [Mitwally, 2009].

Several steps of microstructure variations are expected to develop increasing the annealing parameters, due to the temperature undergone by the material.

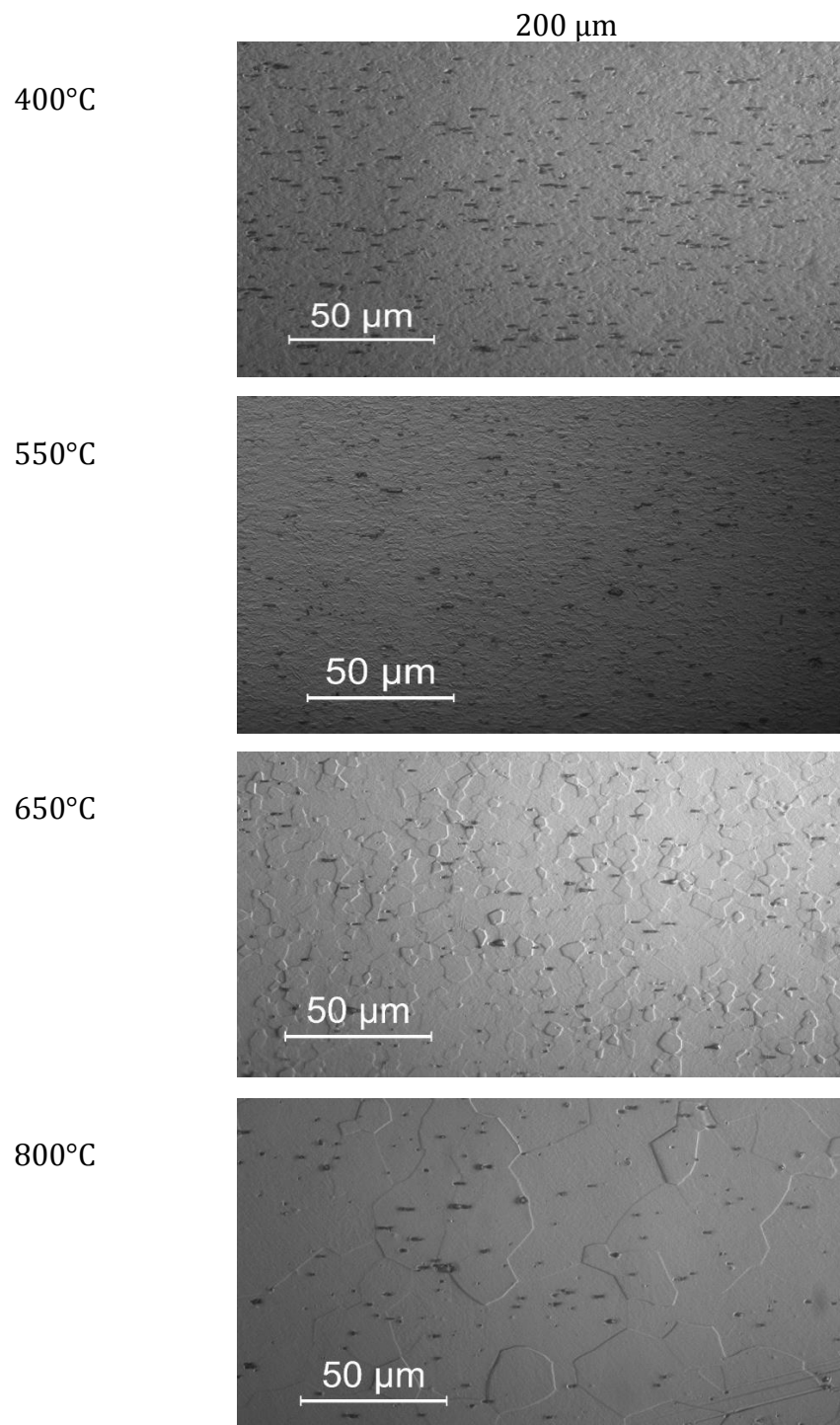


Figure 5.19 Microstructural evolution for the 200 μm wire annealed in furnace at 400, 550, 650 and 800°C.

The lower temperature samples, FA 300 °C for both diameters (Figure 5.21 (a)), are almost unaffected by the laser annealing, still in their cold-worked state and is martensitic. Indeed, they show the microstructures very similar to the cold worked samples. For this low degree of annealing, the cold-work induced martensite has been reverted back to austenite, but without significant microstructural recovery. It is known that due to the mechanically induced stabilization effect, cold-work induced martensite requires increased temperatures to revert back to austenite [Meng, 2012].

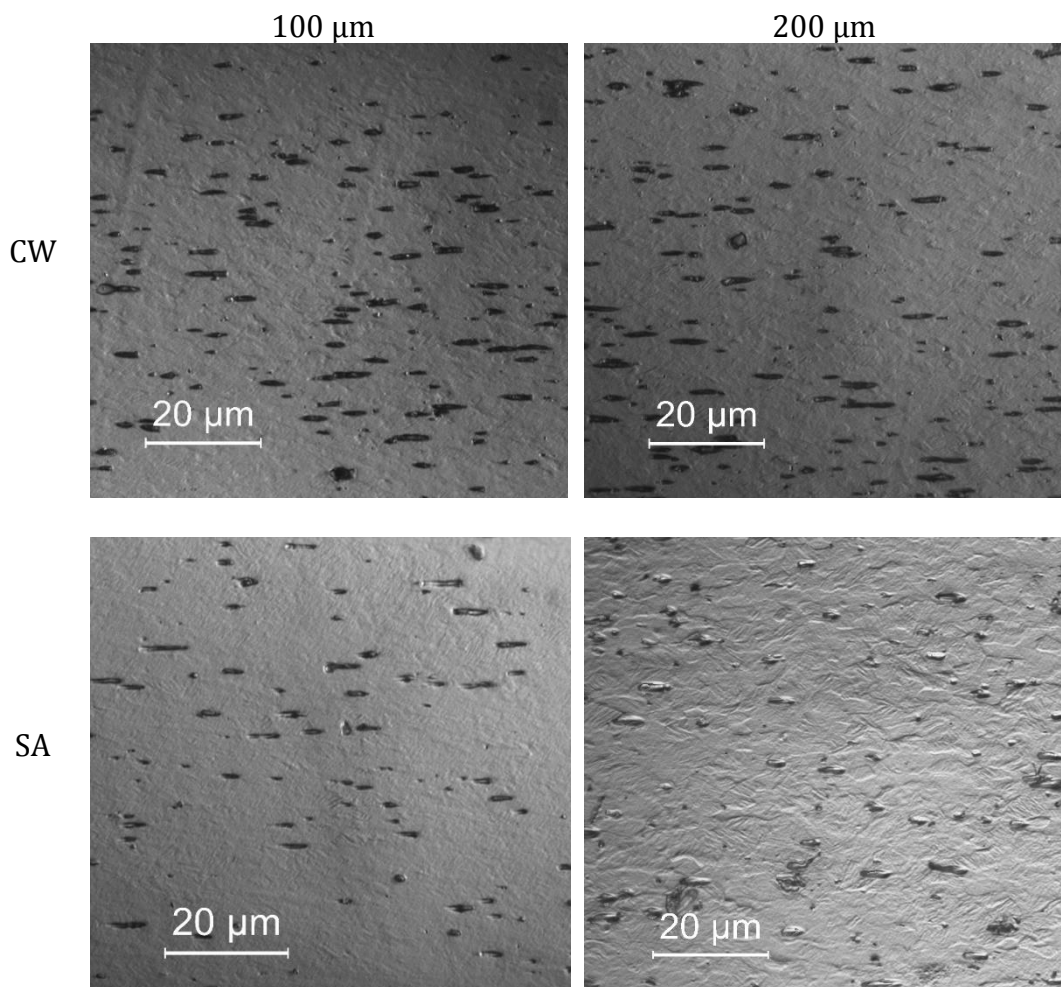


Figure 5.20 Optical micrographs of 100 μm and 200 μm wires in the cold worked and straight annealed conditions.

These samples still contain a high density of defects inherited from the cold work, which appear as darker particles in the micrographs. These particles are highly oriented, indeed their shape is extended along the drawing direction. In these conditions, grain size is nanometric due to the severe plastic deformation imposed to the material during cold drawing and in order to distinguish them, more magnification is required.

Starting from a temperature of about 350°C, the recovery of the material takes place. The upper limit of the recovery temperature range is the recrystallization temperature of the alloy, around 600 °C [Meng, 2012], so samples FA 400 °C, FA 450 °C, FA 500 °C and FA 550 °C (Figure 5.21 (b) and (c) and Figure 5.22 (a) and (b)) are in this state. These four samples exhibit similar microstructures characteristic of elongated un-recrystallized grains; this structure is visible also for the SA 100 µm and 200 µm wires (Figure 5.20). Another effect of the recovery process is the reduction of the density of precipitates. The grain boundaries and the precipitates make dislocation movement difficult; thus, they are important in obtaining optimum superelasticity [McNaney, 2003]. The optimal functional properties exhibited by the wire treated at 450°C can be due to the achievement of the best trade-off between grain size and amount of precipitates within the material. In addition, the superelastic response of such treated wire is stable, since the stress-induced martensitic transformation can proceed in the nanosized microstructure while the dislocation generation and/or slip in the martensite phase are suppressed by the small grain size [Malard, 2011]. From the FA 500 °C sample for the 200 µm diameter and FA 550 °C sample for the 100 µm diameter, grains starts to appear as visible. They present an irregular shape and a striped surface, due to the presence of martensite variants, caused by the initial cold working [Mitwally, 2009]. These martensite variants appears as fine parallel plates within the grains, as verified from electron micrographs carried out by Li et al. [Li, 2008].

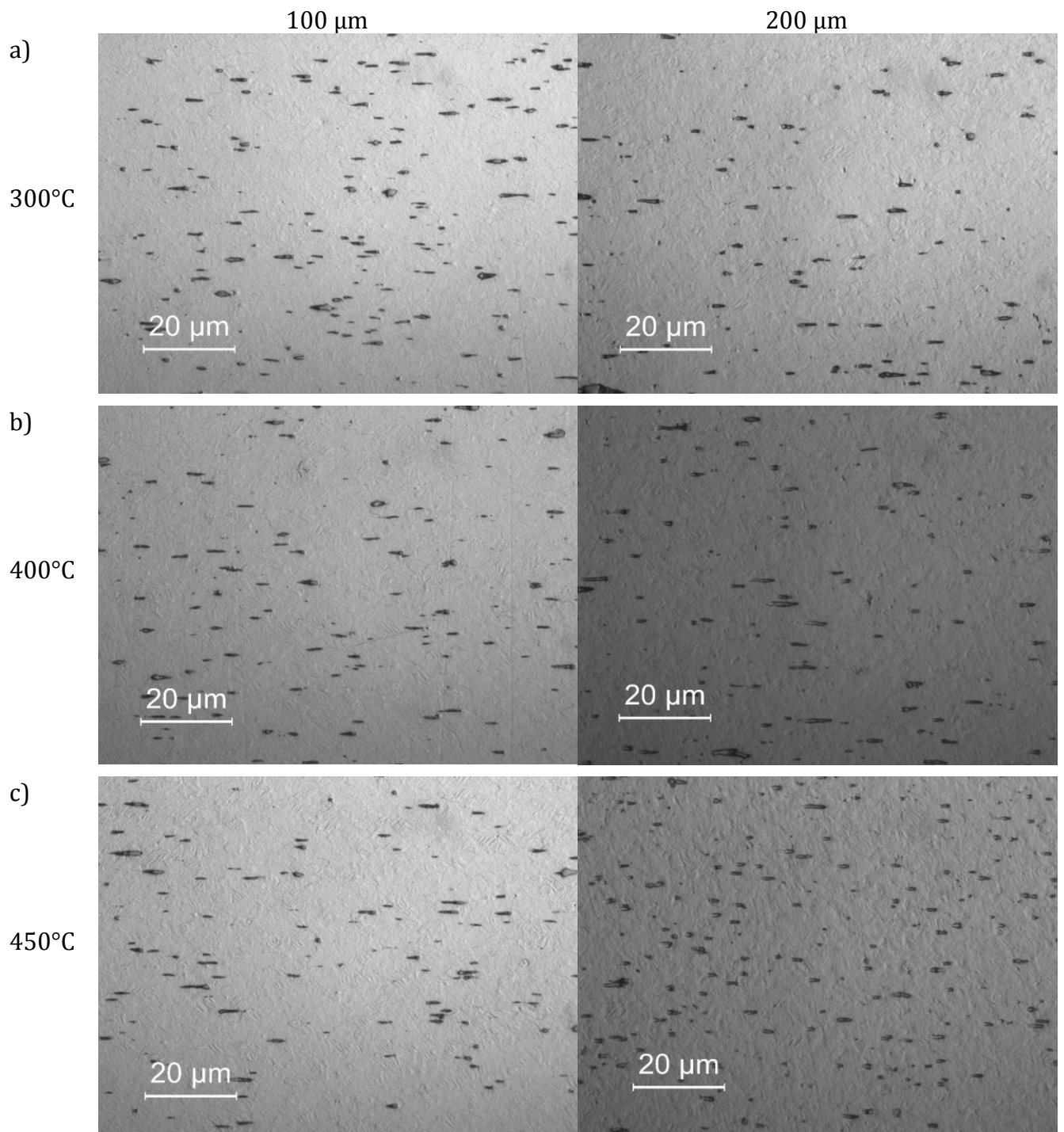


Figure 5.21 Optical micrographs of 100 μm and 200 μm wires annealed in furnace at 300 $^{\circ}\text{C}$ (a), 400 $^{\circ}\text{C}$ (b) and 450 $^{\circ}\text{C}$ (c).

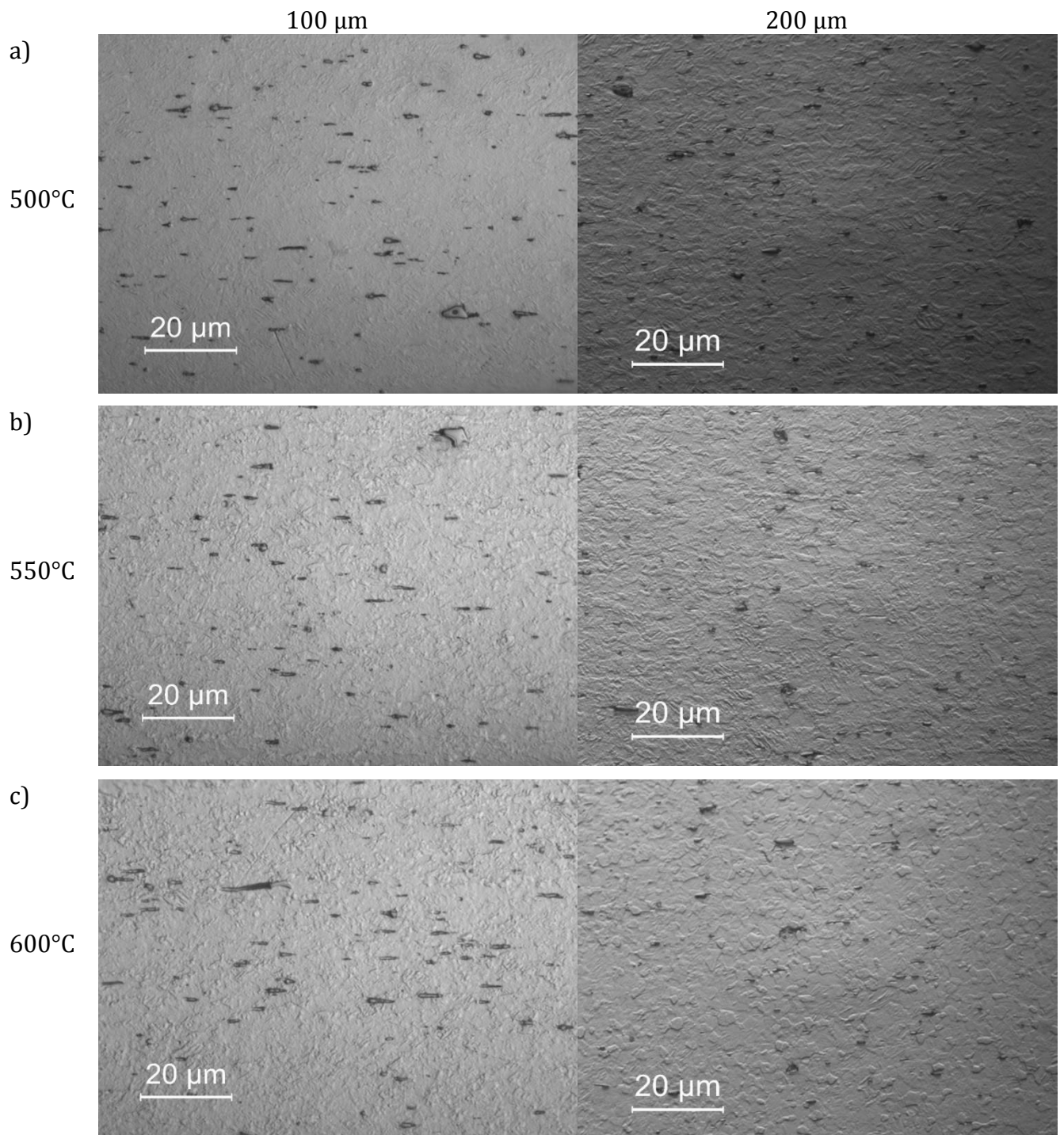


Figure 5.22 Optical micrographs of 100 μm and 200 μm wires annealed in furnace at 500 °C (a), 550 °C (b) and 600 °C (c).

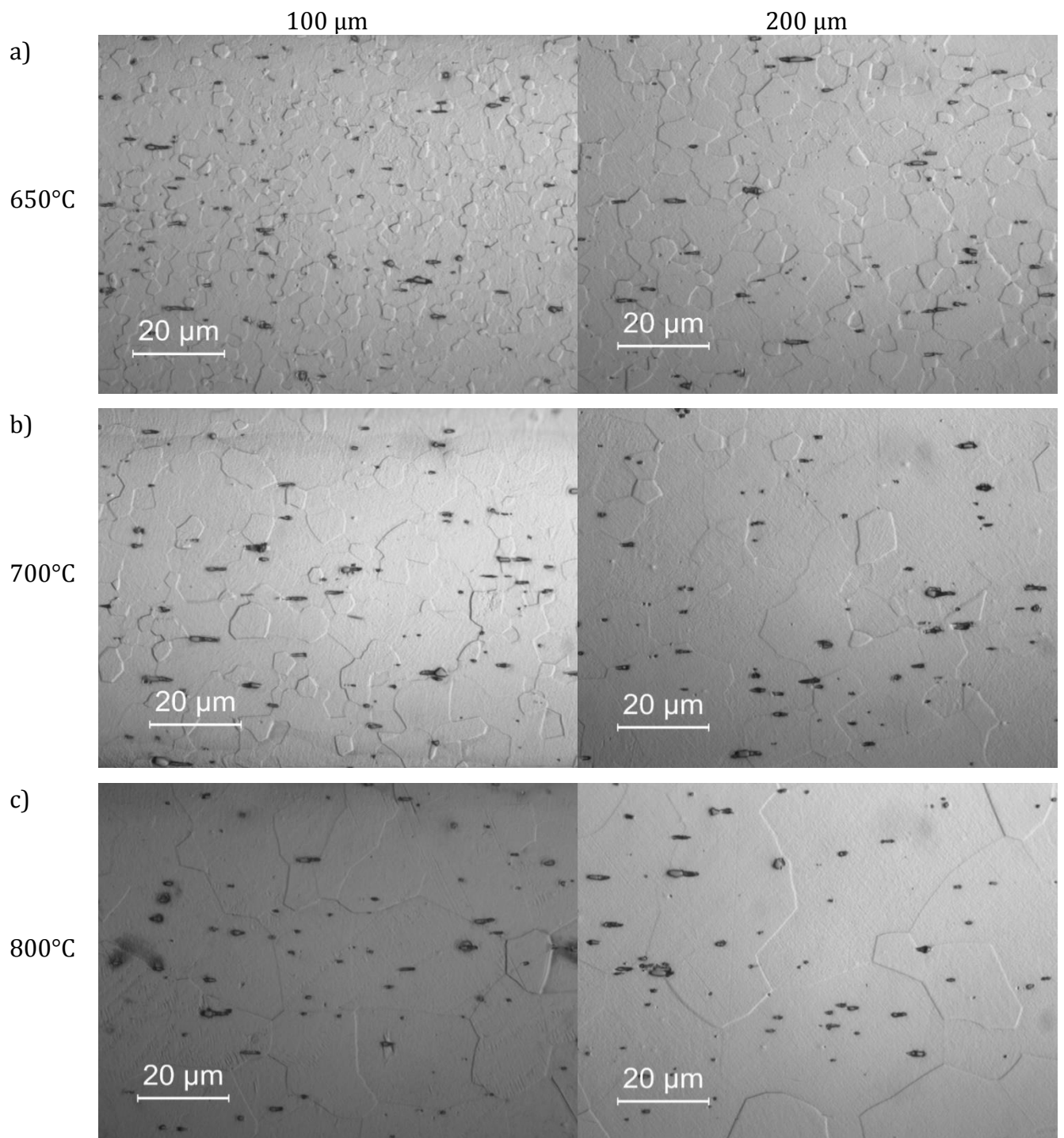


Figure 5.23 Optical micrographs of 100 μm and 200 μm wires annealed in furnace at 650 °C (a), 700 °C (b) and 800 °C (c).

The termination of the recovery process, at about 600 °C, represents an important threshold point in the microstructure evolution, associated with a deterioration in the functional properties of the alloy [Malard, 2011], as detected in the previous thermomechanical characterizations. These remaining conditions presents a recrystallized microstructure, which is the last state of the material before the melting of the alloy, at about 1330 °C [Wang, 2013]. The variation of the sample microstructure with respect to the previous conditions is clearly evident from the micrographs. New grains are formed in the material and they are characterized by an equiaxial shape and a smooth surface. In addition, it is possible to observe the grain coarsening obtained above the recrystallization temperature with an increase in the degree of annealing of the material. Indeed, in FA 600 °C samples, grains are still very small and the surface is not completely flat, but presents some stripes. FA 650 °C, FA 700 °C and FA 800 °C samples (Figure 5.23 from (a) to (c)) show increasing grain size from few microns up to around 20-30 μm and a well-delineated grain boundary. The grain size observed in the present work are also consistent with the results found by Chang et al. for furnace annealing at 500 and 600°C [Chang, 2001] and by Wang et al. for furnace annealing at 700 °C [Wang, 2013].

CHAPTER 6:

6 Analysis of results and discussion: laser shape setting

The functional properties, exhibited by the material after the annealing process, are strictly related to the amount of energy given to the material during the treatment. The amount of energy in turn depends on the thermic cycle imposed to the material in terms of treatment temperature and duration. In the case of laser annealing performed with speed 50 mm/s and beam diameter at the interaction surface equal to 1,3 mm, the exposition time of each portion of wire surface under the laser beam can be estimated to be equal to 0,026 s for all treatments performed in this work. The temperature induced by the laser beam on the wire depends on the incident power amount, but it can not be controlled or measured easily in this configuration. For the furnace annealing, treatments duration are consistently longer, usually from 10 to 30 min [Miller, 2001; Huang, 2001; Miyara, 2014], so it can be estimated a higher temperature of laser annealing required to produce similar effects on the material. Through the comparison of the results obtained for the different process parameters in the two technologies, it is possible to give an estimation of the range of temperature reached by the wire during the unconventional annealing. Once a parallelism between the furnace annealing and the laser annealing is established, a correspondence between the parameters that characterize the two treatment techniques can be obtained. However, also difference are noticed for the two annealing techniques, due mainly to the different kind of process involved.

In the following, cold worked wires laser annealed with incident power equal to 65 W, 75 W and 85 W are called LA 65 W, LA 75 W and LA 85 W.

6.1 Calorimetric analysis

In Figure 6.1 and 6.2, the evolution of the calorimetric response of the material varying the incident power of the laser beam used for the treatment is reported for each level of load considered in this work. The starting condition of the material, the cold worked state, is shown at the top of each figure and the curves are overlapped to the one obtained for the 100 μm straight annealed wire. All laser treated samples presents the characteristic peaks of the martensitic forward and reverse transformation, confirming as first fundamental result that all power level selected for the annealing in the present work are sufficient to induce the superelastic properties in the alloy. As seen for the furnace treatments, an increase of the amount of energy given to the material during the annealing process results in a sharpening and lengthening of the peaks, along with the approximation and consequent overlapping of the peaks when the transformation occurs in two steps. Indeed, only samples treated with power 65 W and 75 W display the R-phase transformation on cooling, while a single peak transformation characterize the 85 W treatment. On heating, the R-phase transformation is not present in any of the samples. The qualitative comparison with the straight annealed material reveals lower characteristic temperatures and higher amount of latent heat of transformation in the laser annealed samples.

In most of the DSC curves of the samples treated at power 75 W and 85 W, the martensitic transformation appears as a multiple peak. This can be due to a phenomenon of multiple-step martensitic transformation, similar to the one observed in Ni-rich alloys: due to the composition inhomogeneity of the material, the martensitic transformation sequences occur on cooling in more than one step [Khalil Allafi, 2002]. This can be due to the influence of slight concentration differences between precipitate interfaces and matrix or to large-scale microstructural inhomogeneities, such as a heterogeneous distribution of particles in the microstructure. In this case, the local regions containing a high fraction of precipitates undergo a normal transformation, while the remaining precipitate-free regions, containing a higher Ni content, transform independently. Both phenomena would result in multiple-step martensitic transformations [Carroll, 2004].

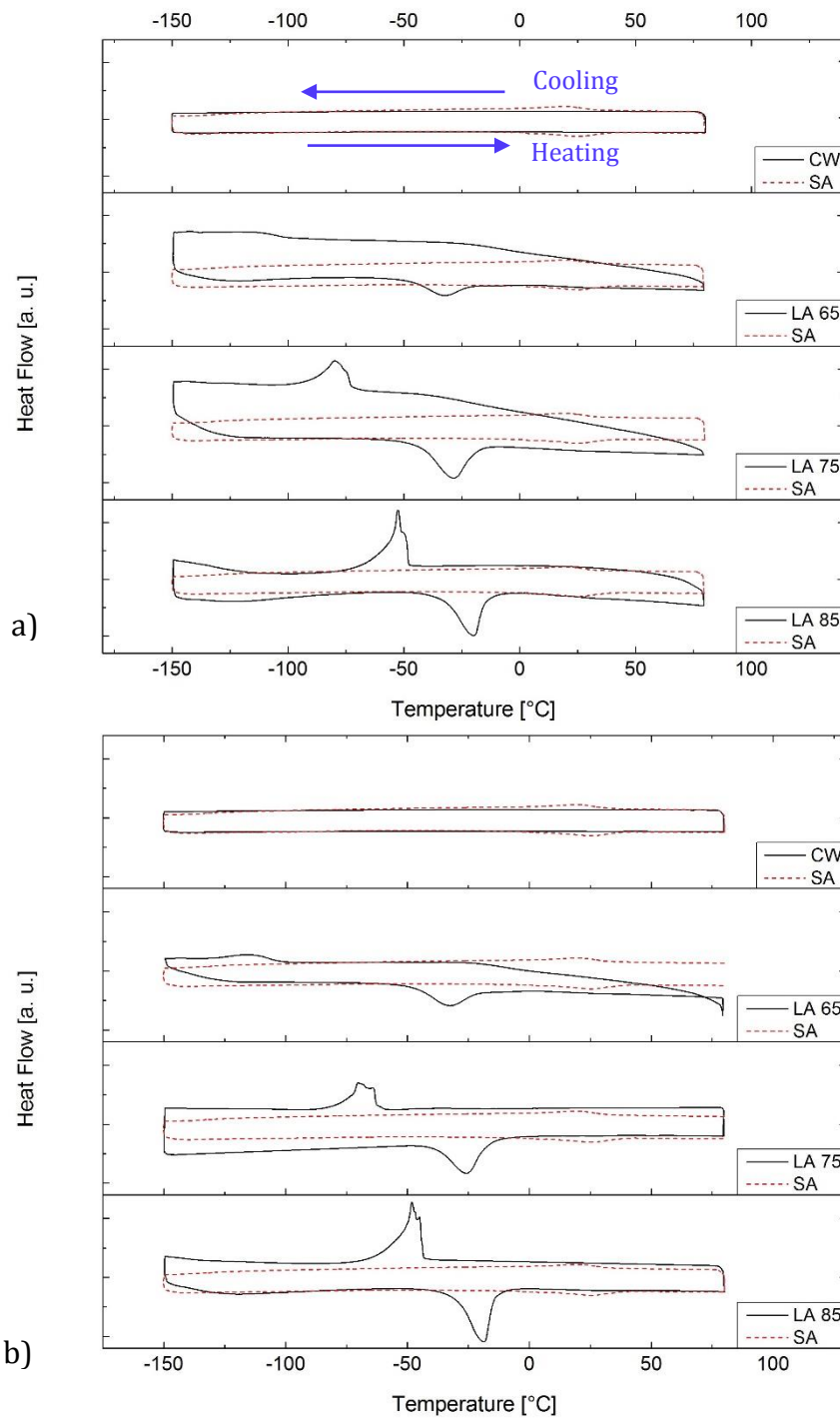


Figure 6.1 Evolution of the DSC response for the laser annealing with load 5 MPa (a) and 50 MPa (b), starting from the cold worked condition to the laser annealed material, treated with incident power 65 , 75 and 85 W.

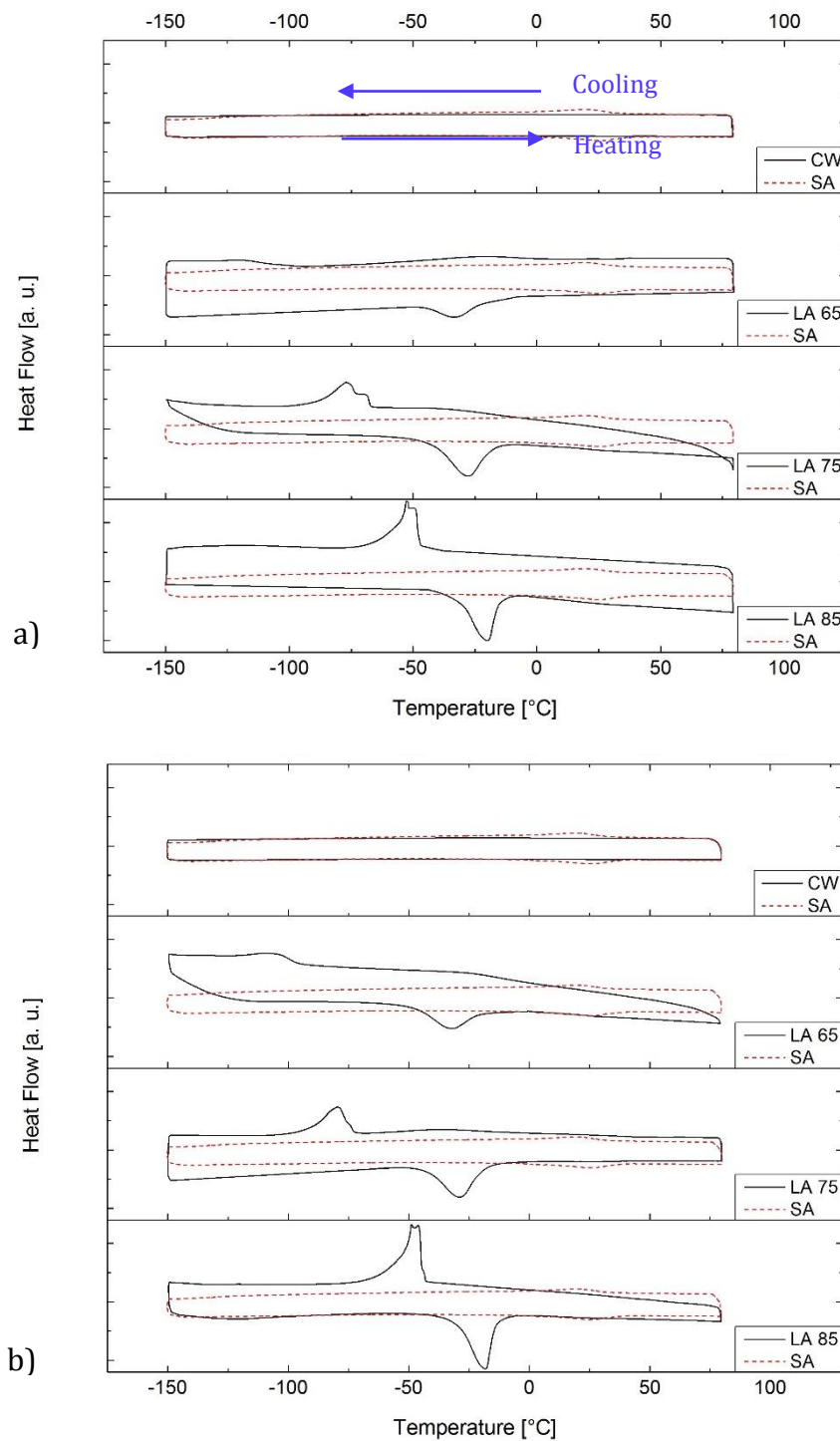


Figure 6.2 Evolution of the DSC response for the laser annealing with load 150 MPa (a) and 300 MPa (b), starting from the cold worked condition to the laser annealed material, treated with incident power 65, 75 and 85 W.

The cause of the material structure inhomogeneity, not detected in the case of furnace annealed samples, can be found in the nature of the laser process itself: instead of uniformly heating all the component and maintain it at a constant temperature for several minutes, the laser beam hits the wire just on the upper surface and the heat is transferred to one portion of the material at a time, leaving the heating of the whole section to conductivity phenomena. However, due to the small dimensions of the analyzed wires, the material structural heterogeneities are not enough to affect the functional properties in a negative way. The lack of multiple-step martensitic transformation in the 65 W annealed samples can be attributed to lower thermal gradients generated between the different portions of the wire during the treatment.

A better investigation about load and power influence on the characteristic temperatures can be performed by looking at Figure 6.3, 6.4 and 6.5, where the start and finish temperatures of martensite and R-phase transformation on cooling and austenite transformation on heating are reported as a function of incident power and applied load. Since three repetitions are carried out for every process condition, the graphs are realized using the average and the standard deviation of the measured values.

Concerning the influence of the applied load on the treatment at fixed power, small variations in the characteristic temperatures can be noticed, but they are not significative with respect to the values' dispersion. It can be therefore stated that the calorimetric response of the material is not particularly sensitive to the load variation.

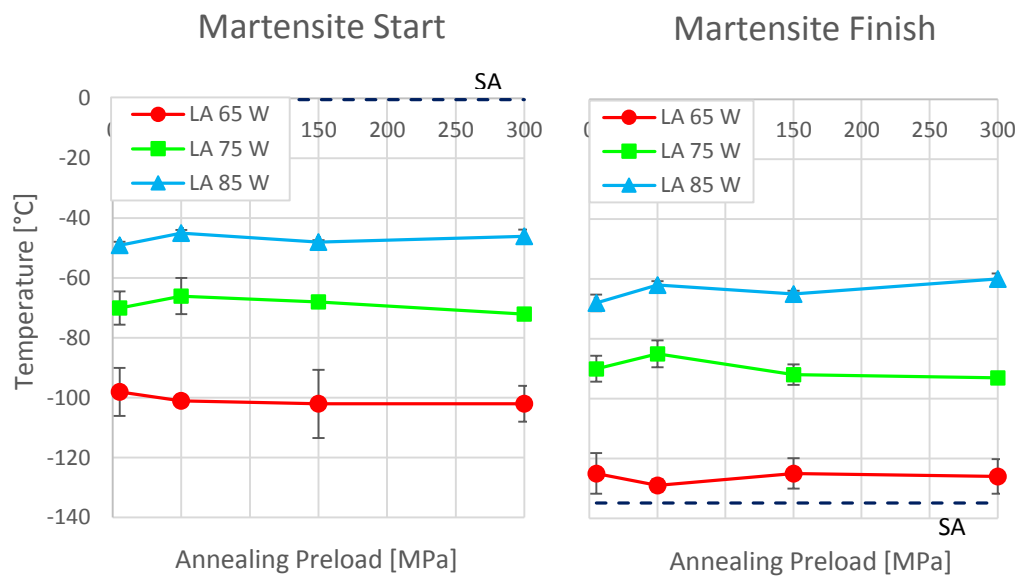


Figure 6.3 Martensite characteristic temperatures upon cooling: martensite start (left) and martensite finish (right). The dashed lines are the corresponding characteristic temperatures for the straight annealed wire.

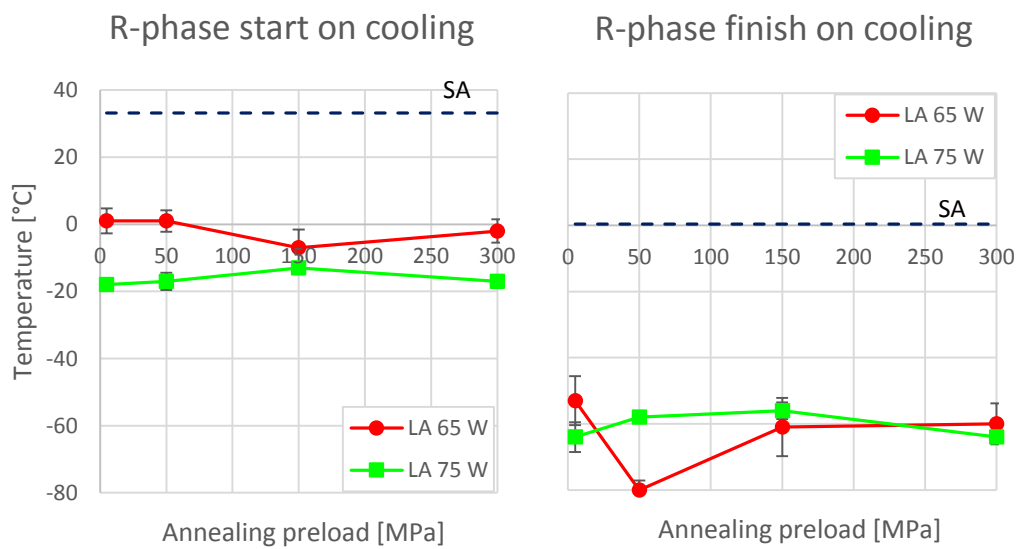


Figure 6.4 R-phase characteristic temperatures upon cooling: R-phase start (left) and R-phase finish (right). The dashed lines are the corresponding characteristic temperatures for the straight annealed wire. The R-phase transformation is not present for the LA 85 W wire.

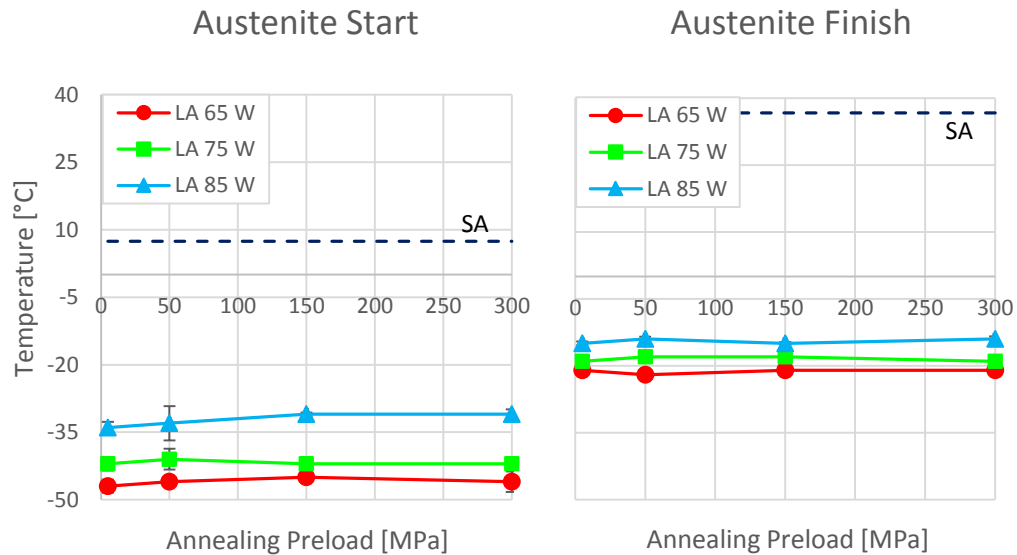


Figure 6.5 Austenite characteristic temperatures upon heating: austenite start (left) and austenite finish (right). The dashed lines are the corresponding characteristic temperatures for the straight annealed wire.

More evident changes are instead connected to incident power variation. The martensite start and finish temperatures (see Figure 6.3) are raised by the increase of incident power of the laser beam, while the peak width of the transformation decreases (see Figure 6.6). Similar trends of temperatures and peak width are found for the austenite transformation (see Figure 6.5 and Figure 6.6). It is important to notice that the A_f temperature is below the room temperature for all the process conditions, meaning that the alloy presents a superelastic behavior at room temperature for all the samples. The width of the martensite and austenite peaks is consistently smaller than the value found for the straight annealed wire, indicating a greater homogeneity of the material during the phase transition. In both transformations, the enthalpy increases with the power level (see Figure 6.7).

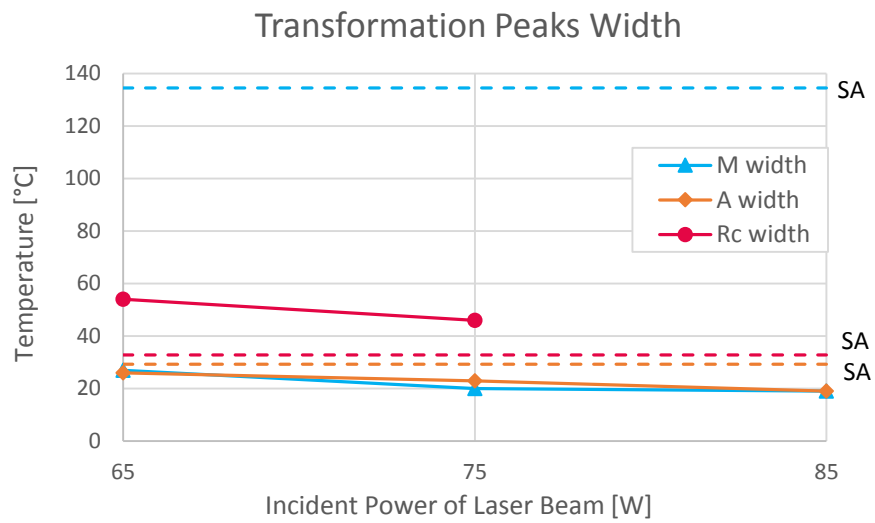


Figure 6.6 Evolution of the peak width of the martensite and R-phase transformations upon cooling and austenite transformation upon heating as a function of the laser annealing power for the annealing with minimum level of applied load (5 MPa).

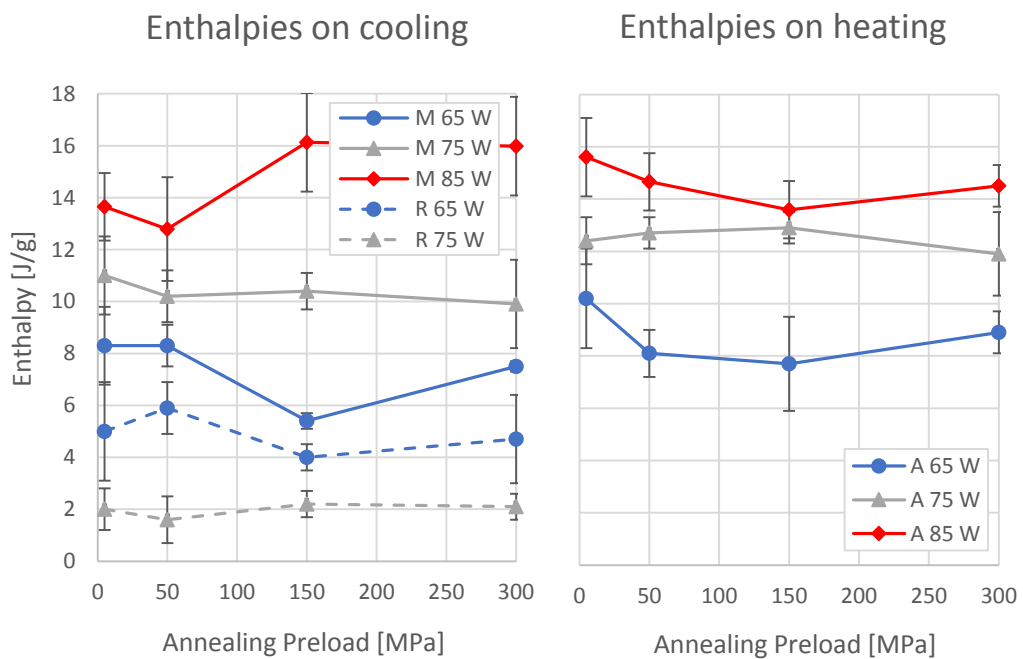


Figure 6.7 Transformation enthalpies of R-phase and martensite upon cooling (left) and austenite upon heating (right) for the three levels of incident power analyzed.

Comparing the laser annealed samples analyzed above to the furnace treated ones, it is possible to identify a correspondence between the process parameters of the two technologies in terms of achievable calorimetric response. Regarding laser shape setting, only the wires treated at the minimum level of load (5 MPa) are used for the comparison in order to guarantee a higher coherence with the furnace annealing, where the wire straight shape is maintained through the use of a small tube of quartz. Nevertheless, the low influence of the load on the calorimetric properties of the material allow us to extend the considerations also to the remaining conditions.

As expected, analogous trends are detected for an increase in laser power or in furnace temperature: indeed, as mentioned before, an increase of the treatment power implies an increase of temperature generated on the wire. The only exception is the evolution of the austenite transformation, which occurs for increasingly lower temperatures decreasing the energy provided by the laser beam, on the contrary of what is observed for the furnace treatment. In addition, the A_s and A_f temperatures values found for the laser annealing process are always lower than the ones measured in the furnace treated wires. Since this difference is present for all analyzed samples, this aspect will be neglected in the following detailed comparison. More in detail, the LA 65 W wire can be associated to an intermediate condition between the FA 500 °C and FA 550 °C, having two wide and low transformation peaks upon cooling and one single peak upon heating. The characteristic temperatures of martensite and R-phase peaks are closer to the value found for the FA 500 °C sample, as well as the peaks width and the enthalpy values. The sample LA 75 W presents more elongated and close peaks on cooling, recalling again the shape of the curve of the FA 550 °C condition, analogy confirmed in this case also by temperatures and enthalpies quantitative comparison. The last power level tested, 85 W, induce calorimetric properties on the material that are very similar to the effects of furnace annealing at 600 °C or more. Indeed, the DSC curve of the LA 85 W sample exhibits single peak transformations both on cooling and heating, with narrow and high peaks. The enthalpy values and the width of the peaks suggest a low level of solubilization, as observed in the FA 600 °C wire, and also transformation temperatures ranges are comparable for these two samples.

6.2 Mechanical analysis

Stress-strain curves for the laser annealed samples subjected to a loading/unloading cycle are shown in Figure 6.8 and 6.9, where the first condition represents the cold worked sample, starting material for all the treatments. The test are performed in strain control and the maximum imposed strain is equal to 10%. The curves are overlapped to the mechanical response acquired for the straight annealed sample loaded up to the same maximum strain. All the laser annealed samples reveal the typical behavior of superelastic SMAs, meaning that the energy provided to the material at all investigated power levels is enough to provide the alloy with the required functional properties. Increasing the incident power of the laser beam, it can be easily observed an increase of the plateau total length, but also of the residual deformation, as confirmed by the values reported in Figure 6.10. Concerning characteristic stress values, an increment of the energy provided by the treatment cause a decrease of the loading plateau stress (Figure 6.11 (left)) and a slight increase of the mechanical hysteresis (Figure 6.11 (right)). As anticipated by the calorimetric analysis results, the influence of the applied load on the functional properties of the wire appears as almost negligible.

Again, for the comparison with furnace annealing, it is possible to consider just one of the stress levels used for the laser shape setting, 5 MPa, and obtain information valid also for the treatments performed at higher levels of applied load. With respect to the SA wire, all laser annealed samples present a higher elastic modulus in the first elastic region, due to the lack of martensitic phase inside the material at room temperature, as confirmed by the calorimetric curves. Indeed, the slope of the stress-strain curve is related to the phases present in the material at the test temperature, and in particular the elastic modulus of the austenite is greater than that of the martensite. This suggest a higher temperature of treatment for the unconventionally annealed samples, as indicated also by the longer plateau length. On the contrary, similar or even better performances than the SA wire are observed for the LA 65 W and the LA 75 W sample in terms of mechanical hysteresis and residual deformation.

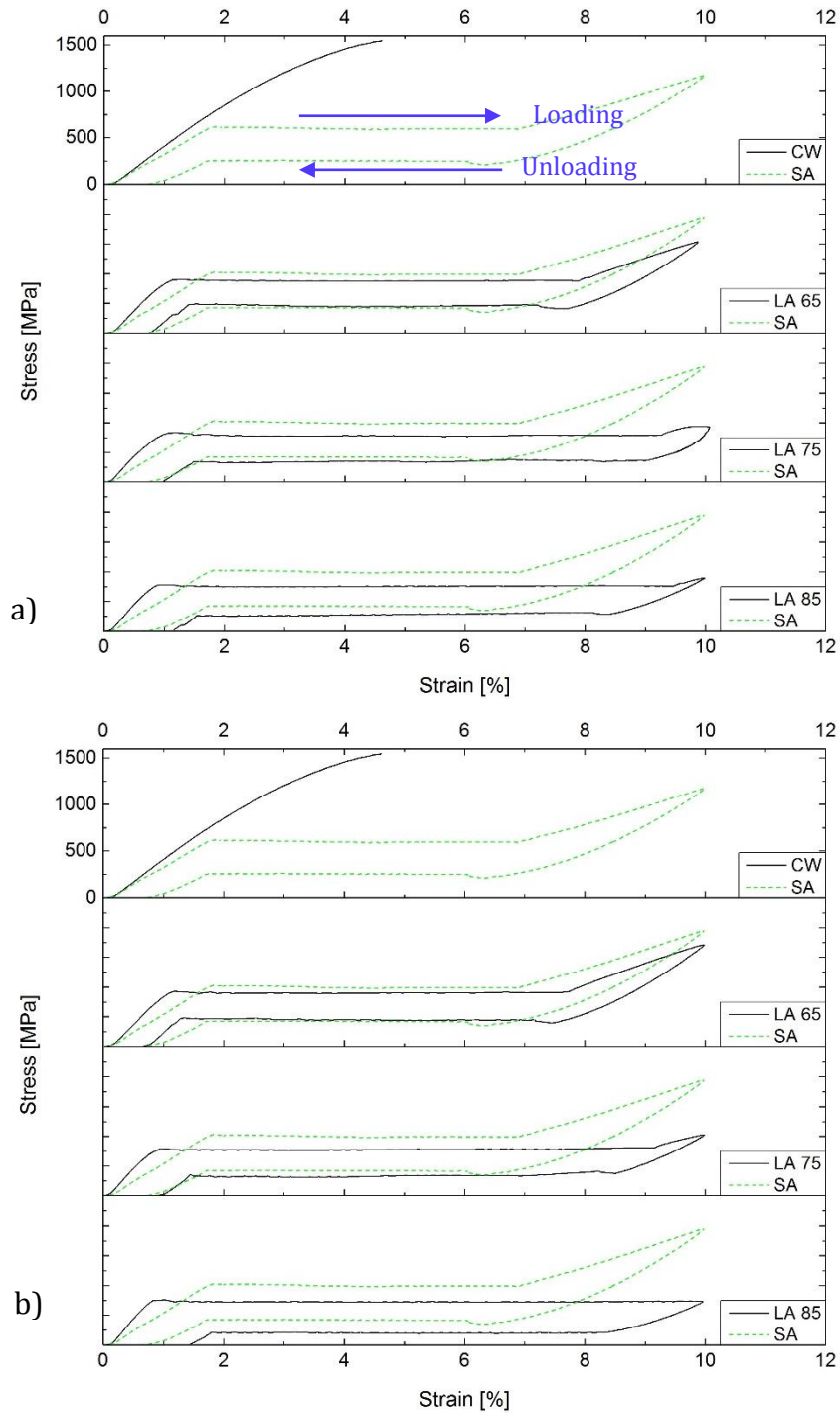


Figure 6.8 Evolution of the stress-strain response for the laser annealing with load 5 MPa (a) and 50 MPa (b), starting from the cold worked condition to the laser annealed material, treated with incident power 65, 75 and 85 W.

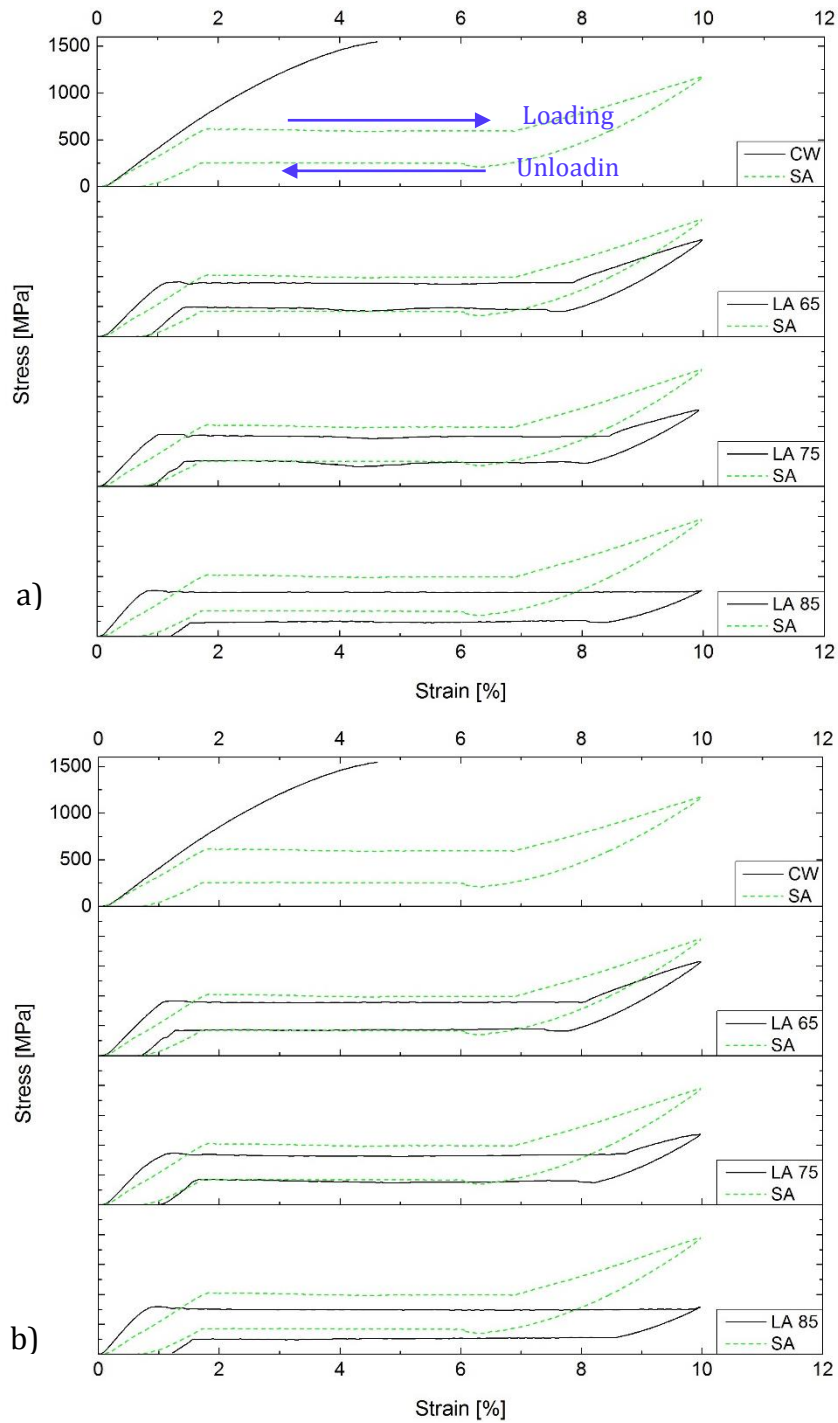


Figure 6.9 Evolution of the stress-strain response for the laser annealing with load 150 MPa (a) and 300 MPa (b), starting from the cold worked condition to the laser annealed material, treated with incident power 65, 75 and 85 W.

More in general, the associations between the three power levels of laser annealing and the temperatures of the furnace treatment based on the calorimetric analysis are supported in the mechanical analysis only by the onset and length of the loading superelastic plateau. The other analyzed properties are instead not in agreement with what expected, but place LA 65 W, LA 75 W and LA 85 W samples in the range of furnace annealing between 400 and 500 °C, where the optimal conditions are found. Indeed, for all laser annealed samples, the mechanical hysteresis and the residual deformation are lower than the corresponding furnace annealing conditions, indicating that a good trade-off between the functional properties is obtained.

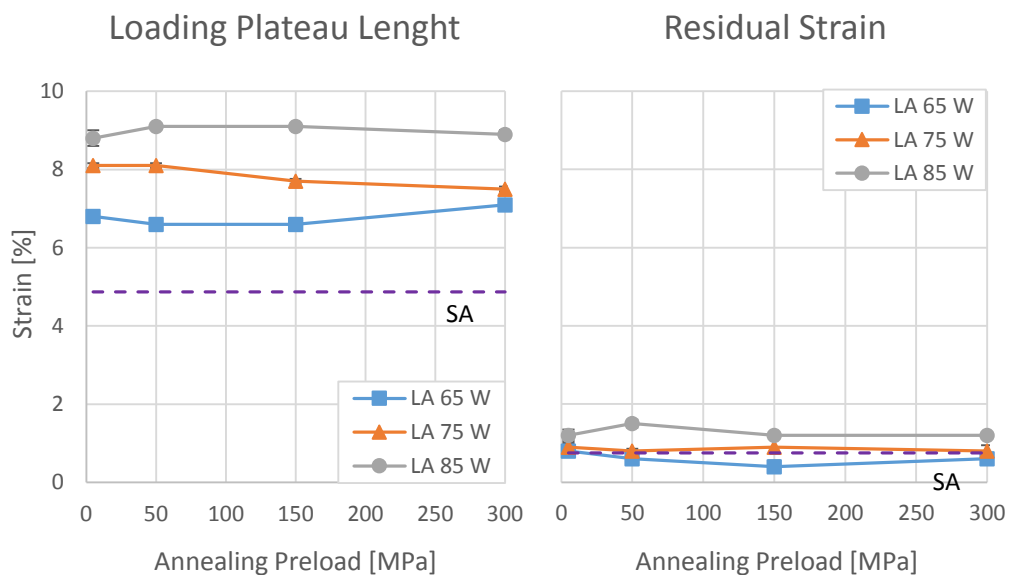


Figure 6.10 Length of the superelastic plateau upon loading phase (left) and residual strain after the first loading/unloading cycle (right). The dashed lines correspond to the strains measured for the 100 μ m straight annealed wire.

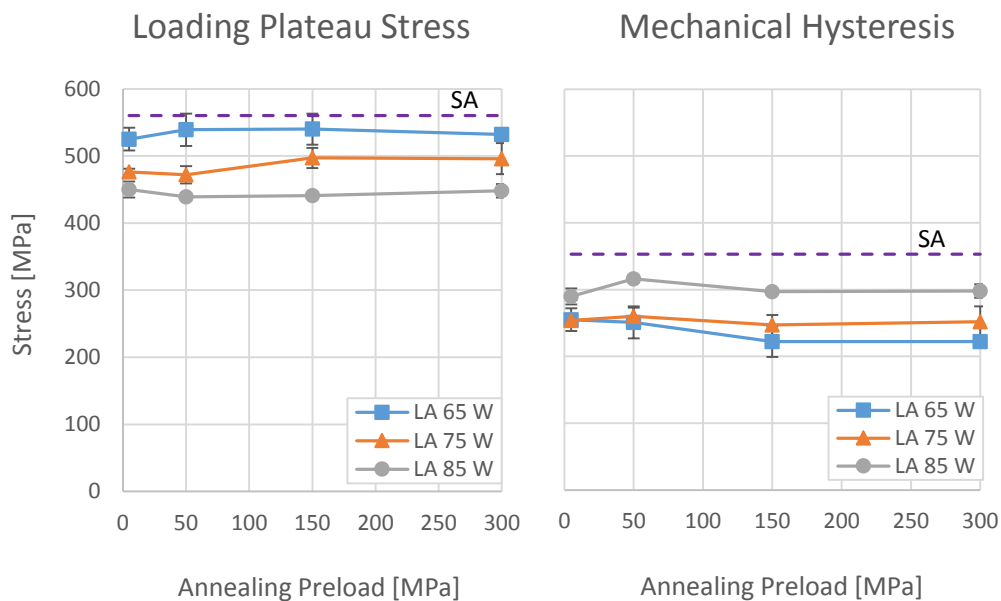


Figure 6.11 Stress value of the superelastic plateau upon loading phase (left) and mechanical hysteresis of the first loading/unloading cycle (right) measured at 3% strain. The dashed lines correspond to the stresses measured for the straight annealed wire.

6.3 Mechanical cycling

The mechanical cycling stability of the laser annealed wires is investigated through loading/unloading repeated cycles. Cycling test are performed on all combinations of process conditions, i.e. three power levels and four load levels. Figure 6.12 (from (b) to (d)) presents the stress-strain curves acquired at cycle 1, 10, 20, 30, 40 and 50 for the wire treated at power 65 W, 75 W and 85 W and with the minimum load value, 5 MPa. In Figure 6.12 (a), the corresponding curves are shown for the SA wire. All the samples are loaded up to 4% strain and unloaded until the minimum amount of residual deformation is reached. Mechanical cycling gradually changes the shape of the superelasticity loop in the stress-strain curve, until the mechanical stability of the component is achieved.

Despite comparable performances in the first cycle, the samples treated at the three power levels exhibit strong differences in terms of mechanical response stability. Indeed, a shape variation for the stabilized curve can be observed comparing the analyzed samples.

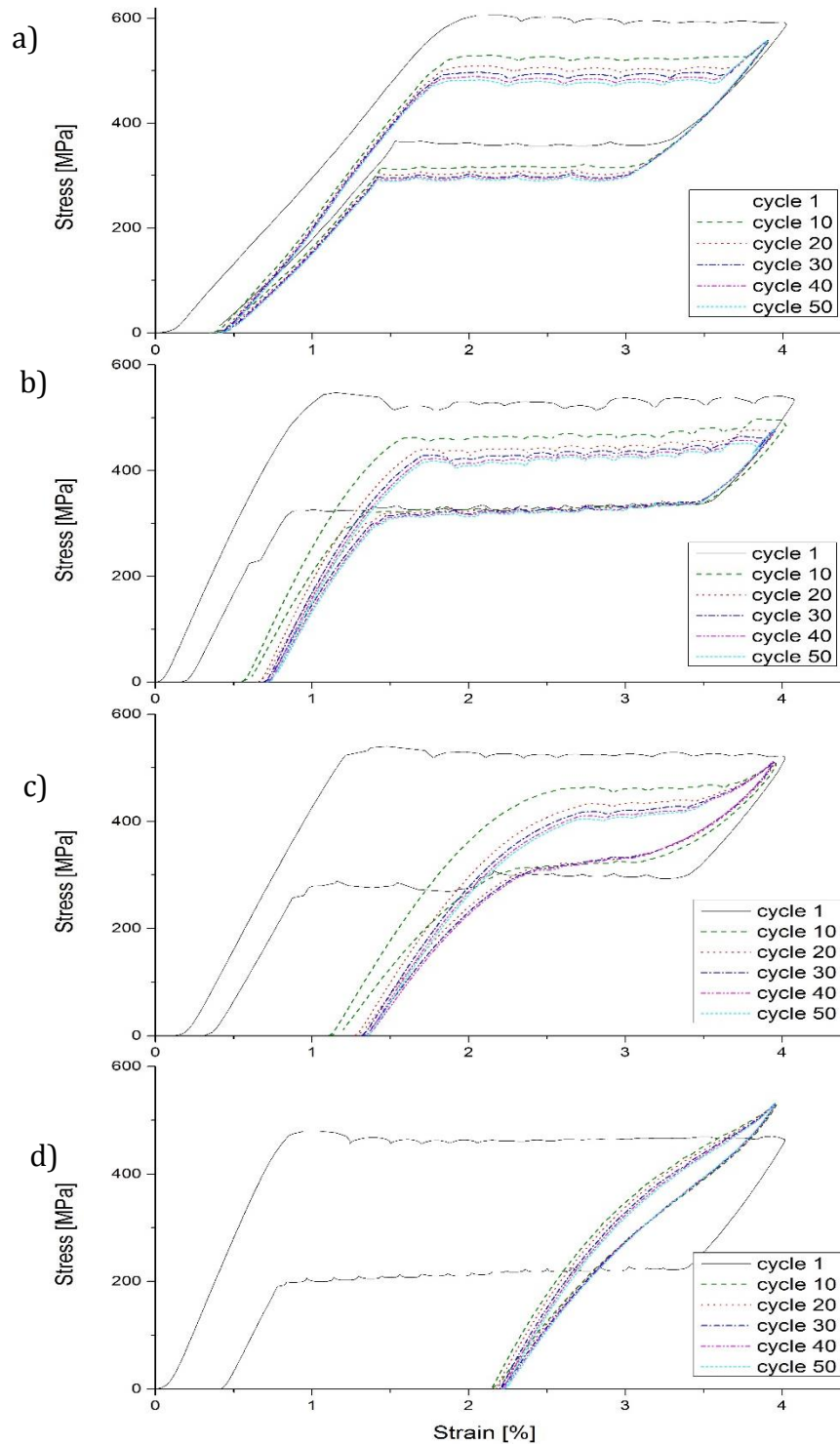


Figure 6.12 Stress-strain curves acquired at cycle 1, 10, 20, 30, 40 and 50 for the SA wire (a) and the laser annealed wires treated at power 65 W and load 5 MPa (b), power 75 W and load 5 MPa (c), power 85 W and load 5 MPa (d) loaded up to 4% strain.

The LA 65 W wire maintains the characteristic superelastic shape of the stress-strain curve during the cycling, gradually increasing the residual deformation and decreasing the mechanical hysteresis between loading and unloading plateaus. In this condition, the minimum amount of the residual deformation after the imposed 50 cycles can be found, thus proving that good functional properties of the alloy are guaranteed also during the component utilization. In the LA 75 W, the superelastic flag is still present, but the transition from the elastic regions to the transformation plateau regions are less sharp and the transformations occurs across a larger range of stress, as evinced by the loss of horizontality of the plateaus. The annealing performed at the maximum power level give as output the worst performances in terms of mechanical stability. Indeed, from the earlier cycles the amount of residual deformation exceeds the 2 %, and the superelastic plateaus are not detectable anymore. Figure 6.13 and 6.14 confirms the previous qualitative observations concerning incident power influence and add the contribution of the applied load to the discussion. However, also this characterization highlights that neither improvements nor worsening of the material properties are produced by the variation of the applied stress in the range analyzed in this work.

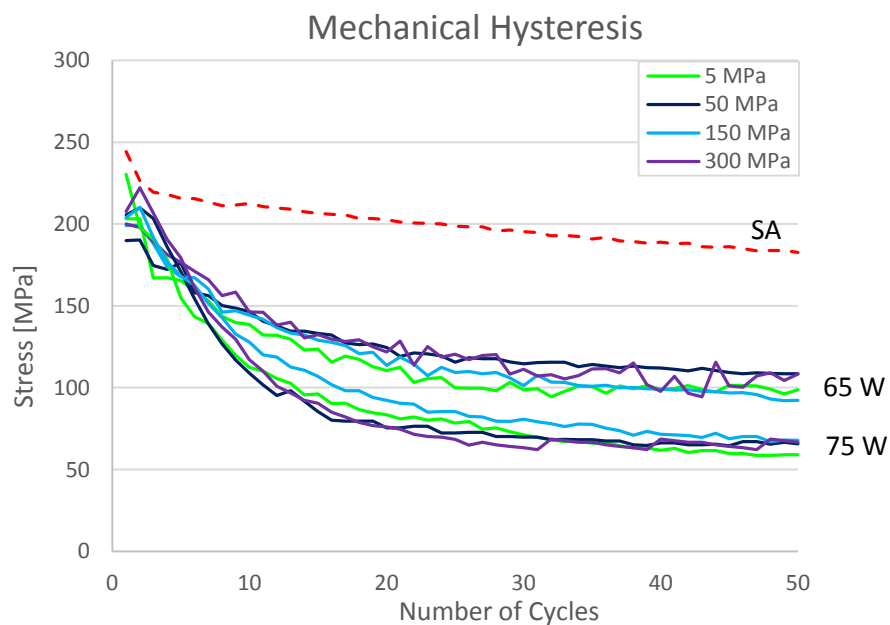


Figure 6.13 Evolution of the mechanical hysteresis measured at 3% strain as a function of the number of cycles for the samples laser annealed at 65 W and 75 W with different levels of load. The dashed line represents the corresponding trend for the straight annealed wire.

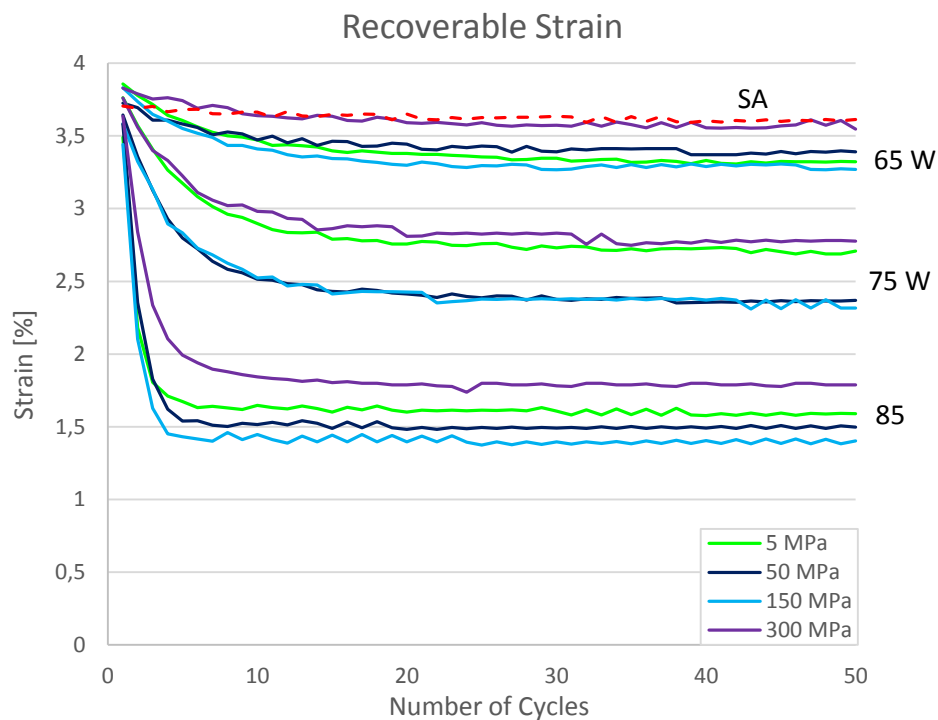


Figure 6.14 Evolution of the recoverable strain as a function of the number of cycles for the samples laser annealed at 65 W, 75 W and 85 W with different levels of applied load. The dashed line represents the corresponding trend for the straight annealed wire.

The mechanical cycling confirms the associations between laser and furnace annealing also from the point of view of the response stability. Moreover, trends observed concerning the influence of energy of the treatment and load amount are in agreement with the results detected in the mechanical cycling analysis carried out in the previous chapter. With respect to the furnace treated samples, a unique mechanical behavior is observed in the laser annealed wires: the lower plateau stress level tends to remain constant during cycling, thus causing a consistent drop in the mechanical hysteresis. For this reason, excellent properties can be achieved, as visible for the LA 65 W sample, which own the highest value of recoverable strain in stabilized conditions, around 3,5%, and a mechanical hysteresis considerably lower than the one found for the optimized furnace annealed sample, the SA wire.

As for the furnace annealed samples, again the mechanical cycling reveals to be a valid method to discriminate among similar material behaviors,

allowing a better understanding of the Nitinol wires performances during the component life time and highlighting the strengths of the laser technology applied to the shape setting of SMA.

6.4 Metallographic analysis

During laser annealing, a relative speed is imposed between the laser beam and the surface, generating rapid heating and cooling of the material, thus this type of process can result in thermomechanical properties of the alloy different from those of conventional annealed samples. For these reasons, characterization of the microstructure is of primary importance in understanding the phenomenology of the laser annealed superelastic Nitinol wires. A full microstructural analysis is beyond the scope of this work, but the present experiments aims to the recognition of common aspects and main difference between the microstructure of laser annealed and furnace annealed samples in terms of grain dimension and morphology.

In Figure 6.15, the micrographs obtained for the wires subjected to laser annealing at power 65 W are shown. The microstructure of these samples presents fine grains typical of a low degree of annealing of the alloy. The morphology observed for the wires sections recalls the appearance of the samples annealed by furnace in the range of temperatures between 400 and 450 °C, where the recovery process has been started but the microstructural characteristics are still very similar to the dislocation-hardened microstructure of the CW wire. Indeed, LA 65 W samples are characterize by a high amount of precipitates inside the austenitic matrix: their presence make dislocations movement difficult, thus they are important in achieving desired superelastic properties [McNaney, 2002]. Material orientation has a profound effect on the mechanical response of the Nitinol alloys. Looking at the micrographs, it can be noticed that the precipitates are aligned with the longitudinal axis of the wires. This type of texture is typically produced during cold-drawing along the longitudinal axis [Gall, 1999].

The micrographs obtained for the lower power level can be compared to the samples treated at the intermediate power level (Figure 6.16) and maximum power level (Figure 6.17). As observed in the furnace annealed samples, the presence of precipitates progressively diminish increasing the annealing degree, i.e. the incident power level used for the treatment.

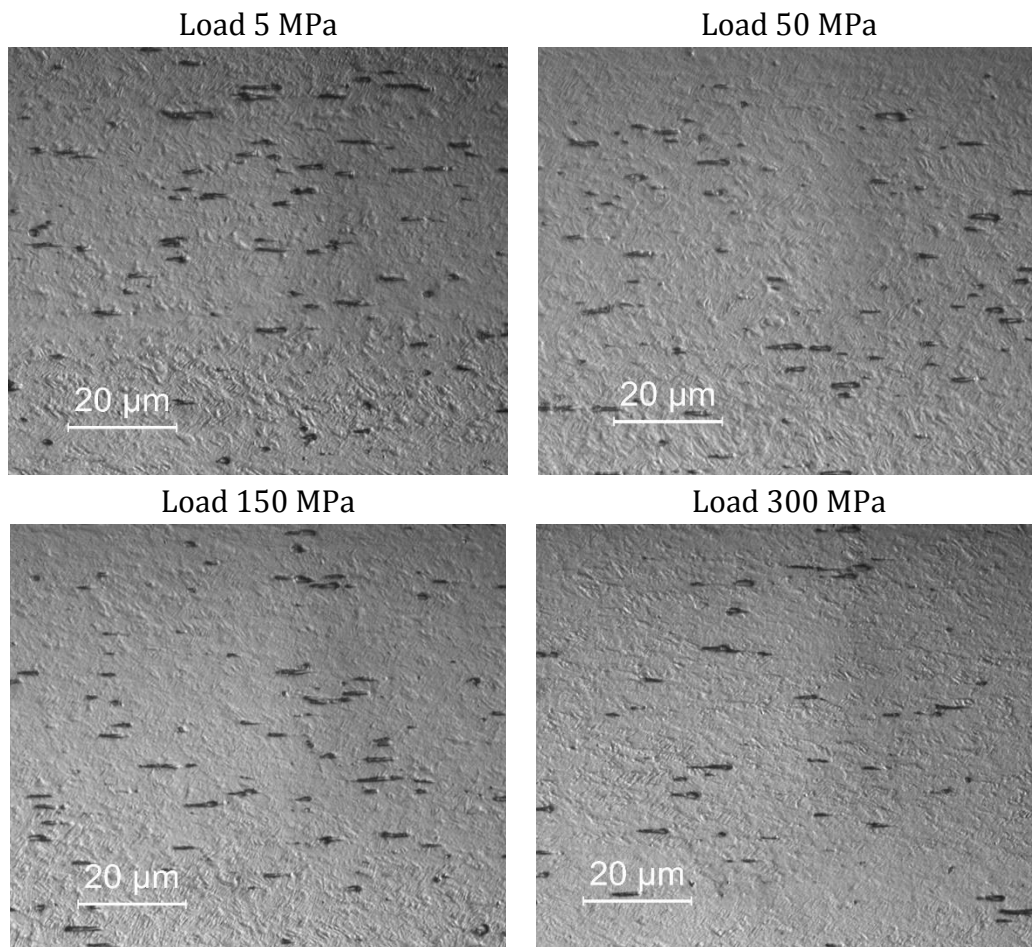


Figure 6.15 Optical micrographs of 100 μm wires laser annealed at power 65 W for the different levels of applied load analyzed.

On the contrary, their size is maintained constant for all the conditions. Results show also that the gradual increase of the incident power of the laser beam leads to the coarsening of the austenitic grains from a nanometric size to a diameter of some microns for the maximum level of power investigated. LA 75 W samples presents small and hardly visible

grains, but a more equiaxial shape with respect to the lower power structure can be noticed. This condition is probably attributable to the start of the recrystallization of the alloy, located around 600 °C. Coarse equiaxial grains are observed in the micrographs of LA 85 W wires, as the effects of this treatment correspond to high temperature furnace annealing. Comparing the grain size, the microstructure presents great similarity with the 100 μm wire treated at 650 °C, characterized by an higher degree of recrystallization of the alloy.

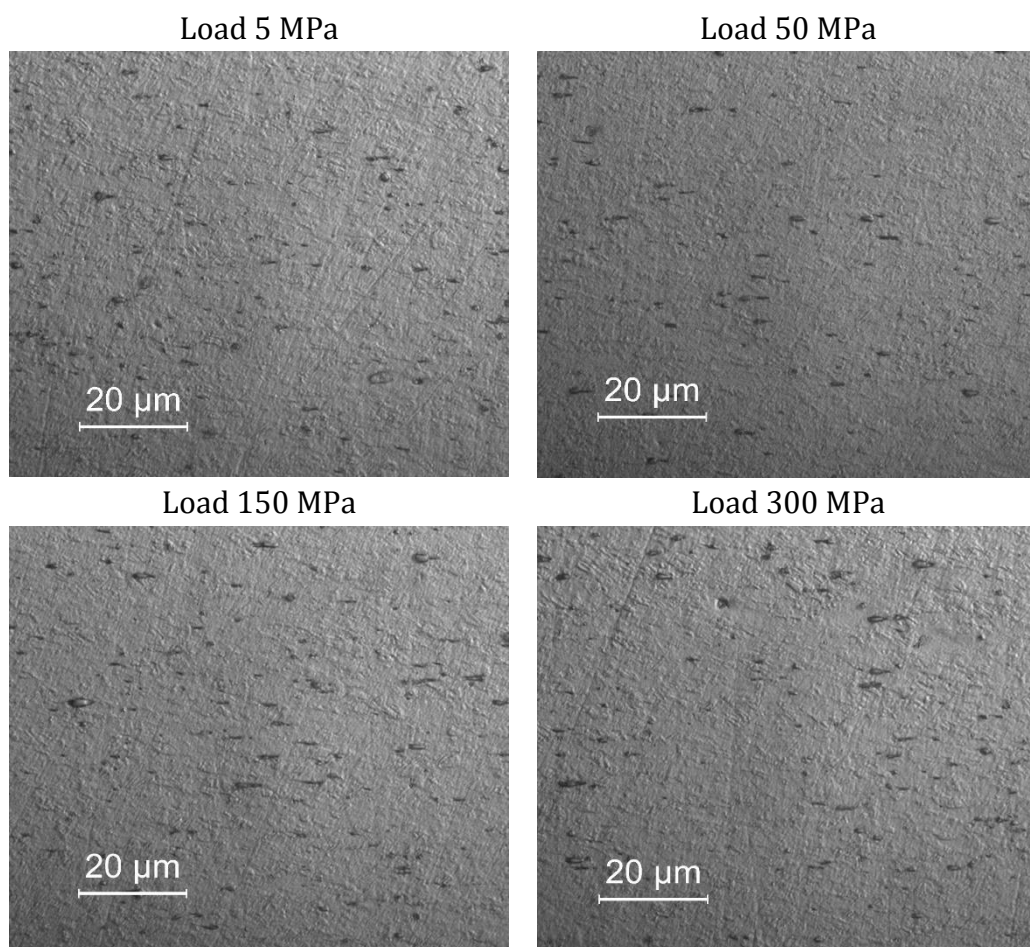


Figure 6.16 Optical micrographs of 100 μm wires laser annealed at power 75 W for the different levels of applied load analyzed.

For each incident power value, different applied stress levels are investigated, showing the absence of visible microstructural modifications related to the load amount. This explain and confirms the lack of significant effects of the load on the functional properties of the superelastic wires found in the previous calorimetric and mechanical characterizations.

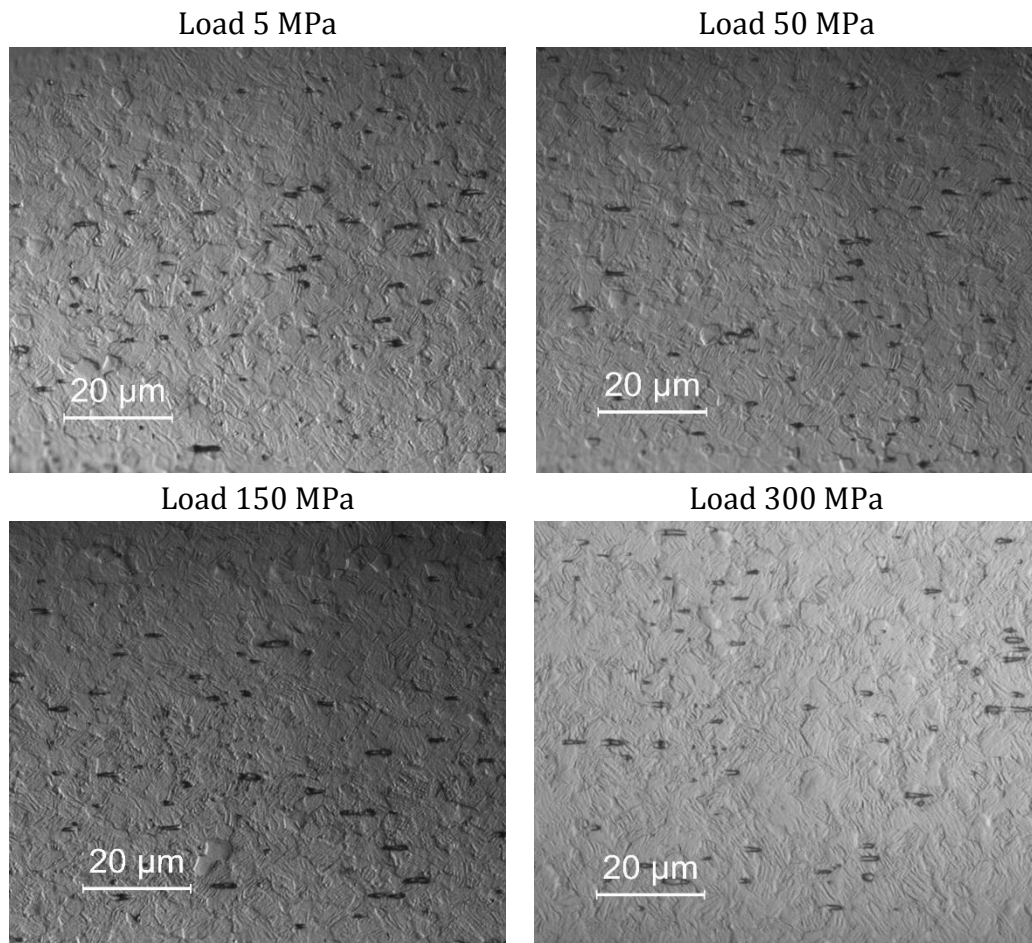


Figure 6.17 Optical micrographs of 100 μm wires laser annealed at power 85 W for the different levels of applied load analyzed.

CHAPTER 7:

7 Conclusions

In this thesis work, laser annealing has been investigated as an unconventional technique to perform straight shape setting on superelastic Nitinol wires with diameter equal to 100 μm . The aim is to deepen the current understanding of the effects of incident power and imposed load on the final properties of the Nitinol wire. The treatment modalities were firstly defined and then a new arrangement of the laser system configuration was required to enable the application and the control of a tensional stress. Preliminary tests and repeatability investigations gave a positive outcome, proving the reliability of the system and allowing the beginning of the experimental campaign. After the execution of the annealing on the Nitinol wires and the thermomechanical and microstructural characterization of the conditions obtained for the material, it was possible to proceed with the last phase of the work, i.e. the analysis and comparison of the samples behavior.

The following conclusions can be drawn:

- all laser power and applied load levels investigated are able to induce superelastic properties in the Nitinol wire through the restoration of the martensitic transformation;
- the variation of the tension load, applied before the treatment and needed to impose the straight shape on the wire, seems to not influence the functional properties of the alloy;
- an increase of the annealing degree is attained increasing the amount of energy transferred to the material by the laser beam, therefore with the use of progressively higher levels of power, inducing an evolution of the material properties analogous to the one observed for the furnace conventional treatment;

- increasing the incident power, the characteristic temperatures of the material transformations raise along with the related latent heat, while the peaks width decreases;
- increasing the incident power, the length of the superelastic plateau increases, but also the residual deformation and the mechanical hysteresis of the martensitic transformation grow, worsening the material performances;
- the results of mechanical cycling showed that low power processing has little effect on the mechanical stability of the wire, whereas high power processing decreases the possible recovered strain in a consistent way;
- the comparison between laser annealed and furnace annealed wires allow the establishment of a correlation between process parameters, but highlight the discrepancies due to the different nature of the two techniques;
- an optimal condition is selected to be the lower power level treatment ($v=50$ mm/s and $P=65$ W), which provide the material with great and stable thermomechanical properties, developing comparable or even better performances than the commercially available furnace annealed wire.

In conclusion, it is possible to state the potentiality of the laser technology applied to the annealing of thin superelastic Nitinol wires as a valid alternative to conventional techniques. This is due to the combination of powerful advantages of the laser annealing process, above all the high speed and productivity of the treatment, and excellent thermomechanical properties developed by the material, as high recoverable strain and low mechanical hysteresis at a stabilized condition.

This study can be a starting point for many possible future investigations and developments, such as:

- a detailed modeling of the power density profile of the power beam, in order to fully understand the interaction between the laser and the wire surface;

- the introduction of further characterization techniques for investigating the microstructural modifications;
- the extension of the experimental campaign:
 - adding an investigation on laser annealing of 200 μm diameter wire to study the homogeneity of the imposed properties;
 - reducing the step between consecutive incident power levels in the proximity of the optimal condition found in this work, in order to tailor the process parameters in a more precise way;
- the implementation of a continuous laser annealing system that allow the valorization of the laser process advantages and which provides a valid alternative to the conventional annealing at an industrial level.

Bibliography

- Bastin G. F. and Rieck G. D.**, *Occurrence and Growth of the Various Intermetallic Compounds*, Metallurgical Transactions Vol.5 (1974) p.1817-1826
- Beauchamps C. H., Nadolink R. H., Dickinson S. C. and Dean L. M.**, *Shape memory alloy adjustable chamber (SMAAC) control surfaces*, Proceedings I European Conference on Smart Structures and Materials, Vol.1777 (1992) p.189
- Bellouard Y., Lehnert T., Clavel R., Sidler T. and Gotthardt R.**, Laser annealing of shape memory alloys: A versatile tool for developing smart micro-devices, *Journal of Physics IV* (2001) p.571-576
- Biffi C. A., Casati R. and Tuissi A.**, *Laser Shape Setting of NiTi Shape Memory Alloy Wires for Actuation Devices* (2014)
- Biffi C. A., Casati R. and Tuissi A.**, *Laser shape setting of thin NiTi wires*, Smart Materials and Structures 25 (2016)
- Bram M., Ahmad-Khanloua A., Heckmannb A., Fuchsa B., Buchkremera H. P. and Stovera D.**, *Powder metallurgical fabrication processes for NiTi shape memory alloy parts*, Material Science and Engineering A (2002)
- Braz Fernandes F. M., Mahesh K. K. and Dos Santos Paula A.**, *Thermomechanical Treatments for Ni-Ti Alloys* (2013)
- Brownell B.**, *Shape transforming lighting fixture*, Transmaterial 2: A Catalog of Materials That Redefine Our Physical Environment (2008) p.47
- Carroll M.C., Somsen C. and Eggeler G.**, *Multiple-step martensitic transformations in Ni-rich NiTi shape memory alloys*, Scripta Materialia, Vol.50 (2004) p.187-192
- Casati R., Vedani M., Gialanella S. and Tuissi A.**, *Electrical Pulse Shape Setting of Thin Ni₄₉Ti₅₁ Wires for Shape Memory Actuators*, Journal of Materials Engineering and Performance, Vol.23 (2014) p.2487-2490
- Chang C. Y., Vokoun D. and Hu C. T.**, *Two-Way Shape Memory Effect of NiTi Alloy Induced by Constraint Aging Treatment at Room Temperature*, Metallurgical and Materials Transactions A, Vol.32a (2001) p.1629-1634
- Daly M., Pequegnat A., Zhou Y. N. and Khan M. I.**, *Fabrication of a novel laser-processed NiTi shape memory microgripper with enhanced*

thermomechanical Functionality, Journal of Intelligent Material Systems and Structures (2012)

Delobelle V., Chagnon G., Favier D. and Alonso T., *Study of electropulse heat treatment of cold worked NiTi wire: From uniform to localised tensile behaviour*, Journal of Materials Processing Technology, Vol.227 (2016) p.244–250

Dolce M., Cardone D. and Marnetto R., *SMA re-centering devices for seismic isolation of civil structures*, Proceedings of SPIE, Vol.4330 (2001)

Duerig T. W. and Melton K. N., *Applications of Shape Memory in the USA*, New Materials and Processes for the Future (1989) p.195-200

Duerig T., Pelton A. and Stockel D., *An overview of nitinol medical applications*, Materials Science and Engineering A273–275 (1999) p.149–160

Fumagalli L., Butera F. and Coda A., *SmartFlex NiTi Wires for Shape Memory Actuators*, Journal of Materials Engineering and Performance, Vol.18 (2009) p.691–695

Gall K. and Sehitoglu H., *The role of texture in tension-compression asymmetry in polycrystalline NiTi*, International Journal of Plasticity, Vol.15 (1999) p.69-92

Hamilton R. F., Sehitoglu H., Chumlyakov Y. and Maier H. J., *Stress Dependence of the Hysteresis in Single Crystal Niti Alloys*, Acta Mater. Vol.52 (2004) p.3383-3402

Herkes B., *The Quiet Technology Demonstrator 2 Flight Test*, The Aviation Noise & Air Quality Symposium (2006)

Hodgson D. E., Wu M. H. and Biermann R. J., *Shape Memory Alloys*, ASM Handbook Vol.2 (1990) p.897-902

Hosoda Y., Fujie M. and Kojima Y., *Three fingered robot hand by using SMA*, Proceedings of the First Annual Conference of Robotic Society of Japan (1983)

Huang X. and Liu Y., *Effect of annealing on the transformation behavior and superelasticity of NiTi shape memory alloy*, Scripta Materialia, Vol.45 (2001) p.153-160

Humbeeck J. V., *Non-medical applications of shape memory alloys*, Materials Science and Engineering A273–275 (1999) p.134–148

- Ishida A., Sato M., Takei A., Nomura K. and Miyazaki S.,** *Effect of Aging on Shape Memory Behavior of Ti-51.3 At. Pct Ni Thin Films*, Metallurgical and Materials Transactions Vol.27A (1996)
- Jani J. M., Leary M., Subic A. and Gibson A. M.,** *A review of shape memory alloy research, applications and opportunities*, Materials and Design Vol.56 (2014) p.1078–1113
- Kajiwara S., Kikuchi T., Ogawa K., Matsunaga T. and Miyazaki S.,** *Strengthening of Ti-Ni Shape-Memory Films by Coherent Subnanometric Plate Precipitates*, Philosophical Magazine Letters Vol.74 (1996) p.137–144
- Khalil-Allafia J. and Amin-Ahmadi B.,** *The effect of chemical composition on enthalpy and entropy changes of martensitic transformations in binary NiTi shape memory alloys*, Journal of Alloys and Compounds 487 (2009) p.363–366
- Khalil Allafi J., Ren X. and Eggeler G.,** *The mechanism of multistage martensitic transformations in aged Ni-rich NiTi shape memory alloys*, Acta Materialia, Vol.50 (2002) p.793–803
- Khelifaoui F. and Guénin G.,** *Annealing of cold-worked equiatomic Ti-Ni alloy followed by DSC and TEP methods*, Journal De Physique IV, Vol.11 (2001)
- Kin I. W.,** *Continuous Annealing of NiTi Shape Memory Alloy and The Investigation of NiTi Shape Memory Alloy Composite*, Master of Science Thesis, City University of Hong Kong (2006)
- Kohl M.,** *Shape Memory Microactuators*, Microtechnology and Mems (2004) p.45-49
- Kumar P. K. and Lagoudas D. C.,** *Introduction to Shape Memory Alloys*, Shape Memory Alloys: Modeling and Engineering Applications (2008) p.1-43
- Li C. H., Chiang L. J., Hsu Y. F. and Wang W. H.,** *Cold Rolling-Induced Multistage Transformation in Ni-rich NiTi Shape Memory Alloys*, Materials Transactions, Vol.49 (2008) p.2136-2140
- Liu Y.,** *Detwinning Process and its Anisotropy in Shape Memory Alloys*, Smart Materials, Proceedings of SPIE, Vol.4234 (2001) p.82-93
- Malard B., Pilch J., Sittner P., Delville R. and Curfs C.,** *In situ investigation of the fast microstructure evolution during electropulse treatment of cold drawn NiTi wires*, Acta Materialia, Vol.59-4 (2011) p.1542–1556

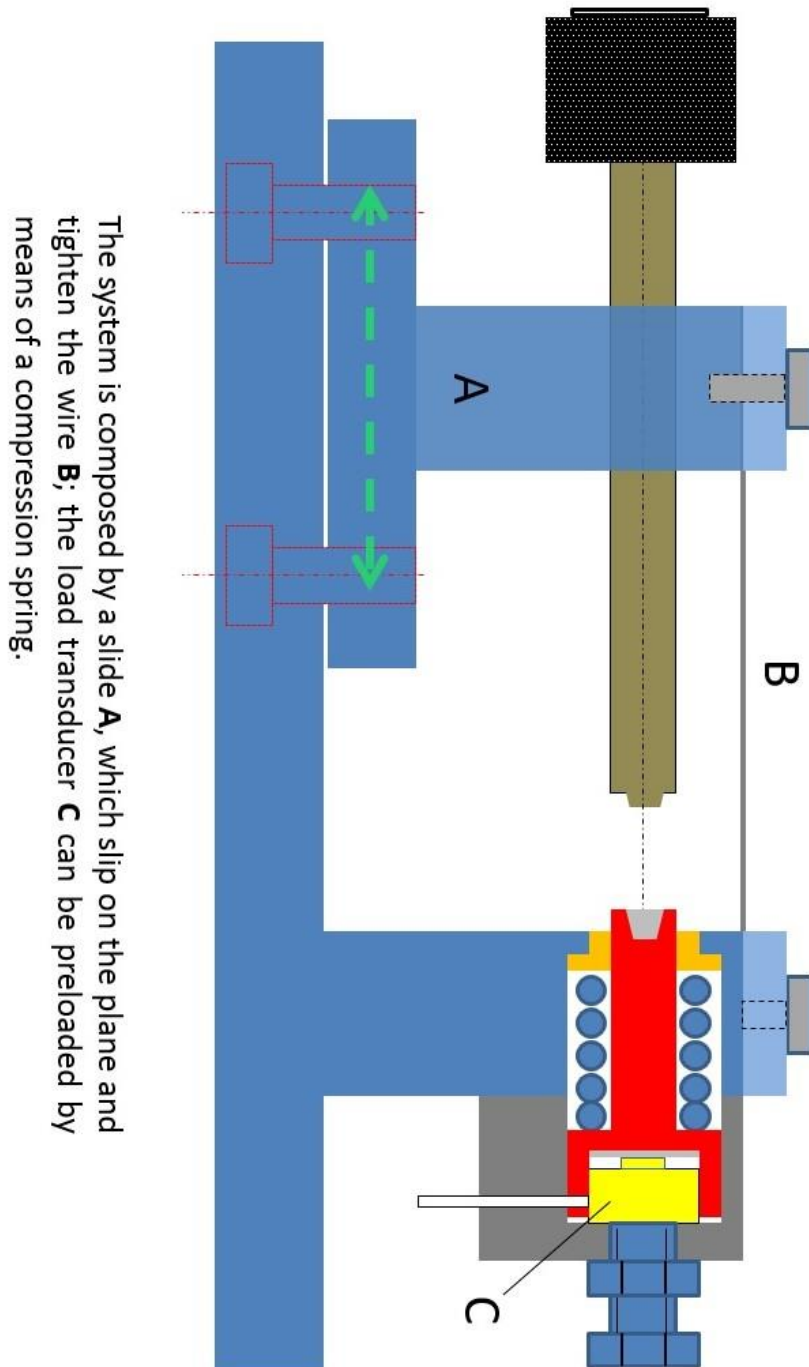
- Maletta C., Flavio A., Furgiuele F. and Reddy J. N.,** *A Phenomenological Model for Superelasticity in NiTi Alloys*, Smart Materials and Structures Vol.18 (2009)
- Maletta C. and Furgiuele F.,** *1D Phenomenological Modeling of Shape Memory and Pseudoelasticity in NiTi Alloys*, Smart Actuation and Sensing Systems - Recent Advances and Future Challenges (2012) p.122-144
- McNaney J. M., Imbeni V., Jung Y., Papadopoulos P. and Ritchie R.O.,** *An experimental study of the superelastic effect in a shape-memory Nitinol alloy under biaxial loading*, Mechanics of Materials, Vol.35 (2003) p.969-986
- Melton K. N.,** *Ni-Ti based Shape Memory Alloys*, Engineering Aspects of Shape Memory Alloys (1990) p.21-35
- Meng Q., Liu Y., Yang H. and Nam T.,** Laser annealing of functionally graded NiTi thin plate, Scripta Materialia, Vol.65 (2011) p.1109-1112
- Meng Q., Liu Y., Yang H., Shariat B. S. and Nam T.,** Functionally graded NiTi strips prepared by laser surface anneal, Acta Materialia, Vol.60 (2012) p.1658-1668
- Miller D. A. and Lagoudas D. C.,** *Influence of cold work and heat treatment on the shape memory effect and plastic strain development of NiTi*, Materials Science and Engineering A308 (2001) p.161-175
- Mitwally M. E. and Farag M.,** *Effect of cold work and annealing on the structure and characteristics of NiTi alloy*, Materials Science and Engineering, Vol.A519 (2009) p.155-166
- Miyara K., Yahata Y., Hayashi Y., Tsutsumi Y., Ebihara A., Hanawa T. and Suda H.,** *The influence of heat treatment on the mechanical properties of Ni-Ti file materials*, Dental Materials Journal (2014) p.27-31
- Miyazaki S., Igot Y. and Otsuka K.,** *Effect of thermal cycling on the transformation temperatures of Ti-Ni alloys*, Acta Metall. Vol.34 (1986) p.2045-2051
- Morgan N. B. and Broadley M.,** *Taking the art out of smart! - Forming processes and durability issues for the application of NiTi shape memory alloys in medical devices*, Proceedings from the Materials & Processes for Medical Devices Conference, ASM International (2004)
- Morgan N. B.,** *Medical shape memory alloy applications—the market and its products*, Materials Science and Engineering A378 (2004) p.16-23
- Otsuka K. and Kakeshita T.,** *Science and Technology of Shape-Memory Alloys: New Developments*, Mrs Bulletin (2002)

- Otsuka K. and Ren X.**, *Physical Metallurgy of Ti-Ni-Based Shape Memory Alloys*, Progress in Materials Science 50 (2005) p.511-678
- Otsuka K. and Wayman C. M.**, *Shape Memory Materials*, Cambridge University Press (1999)
- Petrini L. and Migliavacca F.**, *Biomedical Application of Shape Memory Alloys*, Journal of Metallurgy (2011)
- Pilch J., Heller L. and Sittner P.**, *Heat treatment of thin NiTi filaments by electric current*, SMSTe-Elastic newsletter (2010)
- Potapova A. A. and Stolyarov V. V.**, *Deformability and structural features of shape memory TiNi alloys processed by rolling with current*, Materials Science & Engineering A, Vol.579 (2013) p.114-117
- Russell S. M.**, *Nitinol Melting and Fabrication*, SMST-2000: Proceedings of the International Conference on Shape Memory and Superelastic Technologies (2000) p.1-10
- Sadrnezhaad S. K., Rezvani E., Sanjabi S. and Ziaei Moayed A. A.**, Pulsed-Laser Annealing of NiTi Shape Memory Alloy Thin Film, J. Mater. Sci. Technol., Vol.25 No.1 (2009) p.135-140
- Sadrnezhaad S. K., Yasavol N., Ganjali M. and Sanjabi S.**, Property change during nanosecond pulse laser annealing of amorphous NiTi thin film, Bulletin of Materials Science, Vol.35 No.3 (2012) p.357-364
- Satoh G., Birnbaum A. and Yao Y. L.**, *Annealing Effect on the Shape Memory Properties of Amorphous NiTi Thin Films*, Journal of Manufacturing Science and Engineering Vol.132 (2010)
- Smith S. A. and Hodgson D. E.**, *Shape Setting Nitinol*, Medical Device Materials: Proceedings from the Materials & Processes for Medical Devices Conference, (2014) p.266-270
- Song G., Ma N. and Li H.-N.**, *Applications of shape memory alloys in civil structures*, Engineering Structures, Vol.28 (2006) p.1266-1274
- Spini T. S., Valarelli F. P., Cançado R. H., De Freitas K. M. S. and Villarinho D. J.**, Transition temperature range of thermally activated nickel-titanium *archwires*, Journal of Applied Oral Science, Vol.22 (2014) p.109-117
- Stachowiak G. B. and McCormick P. G.**, *Shape memory behaviour associated with the R and martensitic transformations in a NiTi alloy*, Acta Metall., Vol.36 (1988) p.291-297

- Stockel D.**, *The shape memory effect. Phenomenon, Alloys, Applications* (2000)
- Stolyarov V. V.**, *Deformability and nanostructuring of TiNi shape memory alloys during electroplastic rolling*, *Materials Science and Engineering A*, Vol.503 (2009) p.18–20
- Stolyarov V. V.**, *Influence of pulse current on deformation behavior during rolling and tension of Ti–Ni alloys*, *Journal of Alloys and Compounds*, Vol.577S (2013) p.S274–S276
- Wang X., Bellouard Y. and Vlassak J.J.**, *Laser annealing of amorphous NiTi shape memory alloy thin films to locally induce shape memory properties*, *Acta Materialia*, Vol.53 (2005) p.4955–4961
- Wang X., Li C., Verlinden B. and Van Humbeeck J.**, *Effect of grain size on aging microstructure as reflected in the transformation behavior of a low-temperature aged Ti–50.8 at.% Ni alloy*, *Scripta Materialia*, Vol.69 (2013) p.545–548
- Wayman C. M. and Duerig T. W.**, *An Introduction to Martensite and Shape Memory*, *Engineering Aspects of Shape Memory Alloys* (1990) p.3-20
- Wilde K., Gardoni P. and Fujino Y.**, *Base isolation system with shape memory alloy device for elevated highway bridges*, *Engineering Structures*, Vol.22 (2000)
- Yoneyama T., Doi H., Kobaiashi E. and Hamanaka H.**, *Effect of heat treatment with the mould on the super-elastic property of Ti-Ni alloy castings for dental application*, *Journal of Materials Science: Materials in Medicine* 13 (2002) p.947-951
- Zhu R. F., Tang G.Y., Shi S.Q. and Fu M. W.**, *Effect of electroplastic rolling on the ductility and superelasticity of TiNi shape memory alloy*, *Materials and Design*, Vol.44 (2013) p.606–611
- Zhu R. F., Tang G. Y., Shi S. Q., Fu M. W. and Gromov V. E.**, *Effect of electropulsing treatment on the microstructure and superelasticity of TiNi alloy*, *Applied Physics A* (2013) p.1195–1201
- Zimmermann H.**, *Irreversible strains in an Ni–Ti alloy after thermal cycling*, *Journal of Materials Science Letters* Vol.16 (1997) p.460–461
- Zohari T.**, *Functional Characterization of Laser Annealed Nitinol Wires*, M. Sc. Thesis in Mechanical Engineering, Politecnico di Milano

Appendix A

Schematic of the system used for the application of the tension load on the wire before the laser shape setting.



Appendix B

Data used for the evaluation of the calibration curve of the load cell Burster 8416-5020. Five repetitions of the calibration procedure are carried out.

MASS	LOAD	Rep. 1	Rep. 2	Rep. 3	Rep. 4	Rep. 5
[g]	[N]	[V]	[V]	[V]	[V]	[V]
0	0	0	0	0	0	0
118	1,15758	0,47	0,47	0,46	0,47	0,47
200,3	1,964943	0,8	0,79	0,79	0,79	0,8
313	3,07053	1,24	1,23	1,24	1,24	1,24
407,6	3,998556	1,61	1,6	1,61	1,6	1,59
506,5	4,968765	2,02	2	2	2	2,01
611,3	5,996853	2,43	2,41	2,42	2,41	2,41
698,7	6,854247	2,79	2,77	2,76	2,79	2,8
821	8,05401	3,26	3,24	3,25	3,24	3,25
907,1	8,898651	3,61	3,59	3,58	3,59	3,62
1011,9	9,926739	4,03	4,01	3,99	4,01	4
1118,4	10,971504	4,44	4,41	4,44	4,42	4,41
1218,5	11,953485	4,83	4,75	4,81	4,8	4,79
1320,5	12,954105	5,27	5,24	5,22	5,29	5,24
1427	13,99887	5,68	5,65	5,65	5,63	5,63
1498,9	14,704209	5,98	5,95	5,94	5,99	5,97
1598,9	15,685209	6,4	6,32	6,33	6,33	6,31
1706,3	16,738803	6,81	6,75	6,73	6,78	6,75
1796	17,61876	7,15	7,12	7,1	7,16	7,14
1899,9	18,638019	7,545	7,51	7,52	7,57	7,54

Appendix C

Data measured for the characteristic temperatures [$^{\circ}\text{C}$] and latent heat of transformation [J/g] from the DSC curves of the furnace annealed samples.

In the following tables, M_s , M_f and M_p indicate the martensite start, finish and peak temperatures; R_{cs} , R_{cf} and R_{cp} indicate the R-phase transformation start, finish and peak temperatures on cooling; A_s , A_f and A_p indicate the start, finish and peak temperatures; R_{hs} , R_{hf} and R_{hp} indicate the R-phase transformation start, finish and peak temperatures on heating. The terms $\Delta H\text{-M}$, $\Delta H\text{-Rc}$, $\Delta H\text{-A}$ and $\Delta H\text{-Rh}$ refer to the latent heat of transformation of martensite, R-phase on cooling, austenite and R-phase upon heating, respectively. The empty spaces denote the lack of the corresponding transformation peak in the calorimetric curve.

- 100 μm wire

	Ms	Mf	Mp	Rcs	Rcf	Rcp
300°C/12min						
400°C/12min	-7,77	-129,96	-80,21	49,21	27,66	34,76
450°C/12min	-8,8	-109,92	-46,22	31,7	12,18	22,21
500°C/12min	-70,67	-100,35	-84,23	18,29	6,7	14,91
550°C/12min	-58,73	-83,42	-69,18	-7,57	-28,18	-17,98
600°C/12min	-44,22	-56,81	-47,33			
650°C/12min	-40,22	-46,97	-41,63			
700°C/12min	-39,12	-45,46	-40,17			
800°C/12min	-36,09	-52,18	-37,71			

	As	Af	Ap	Rhs	Rhf	Rhp
300°C/12min						
400°C/12min	13,49	47,7	33,76	-15,43	13,49	4,02
450°C/12min	14,66	35,43	27,01	-20,71	14,66	-0,61
500°C/12min	12,41	21,27	17,24	-11,96	12,41	-0,63
550°C/12min	-20,18	-7,35	-12,96			
600°C/12min	-27,41	-15,47	-20,04			
650°C/12min	-24,85	-17,05	-19,38			
700°C/12min	-24,51	-16,97	-19			
800°C/12min	-23,46	-16,71	-17,86			

	$\Delta\text{H-M}$	$\Delta\text{H-Rc}$	$\Delta\text{H-A}$	$\Delta\text{H-Rh}$
300°C/12min				
400°C/12min	3,5	14	7,6	1,5
450°C/12min	2,8	4,79	8	2,3
500°C/12min	7,4	5,1	10	6,3
550°C/12min	9,2	3,9	13,5	
600°C/12min	20,9		14,8	
650°C/12min	17,7		16,1	
700°C/12min	16,7		14	
800°C/12min	12,8		9	

- 200 μm wire

	Ms	Mf	Mp	Rcs	Rcf	Rcp
300°C/12min						
400°C/12min	-25,19	-97,3	-46,96	49,2	13,77	34,82
450°C/12min	-10,62	-75,54	-20,22	31,06	9,51	22,36
500°C/12min	-65,3	-107,29	-79,22	19,78	10,81	15,67
550°C/12min	-53,3	-77,41	-64,82	-5,55	-18,43	-13,28
600°C/12min	-27,89	-52,18	-40,48			
650°C/12min	-34,3	-41,57	-35,57			
700°C/12min	-38,17	-47,93	-40			
800°C/12min	-32,8	-43,19	-35,31			

	As	Af	Ap	Rhs	Rhf	Rhp
300°C/12min						
400°C/12min	19,61	51,34	38,91	-13,85	19,61	3,59
450°C/12min	14,84	33,86	26,37	-15,28	14,84	-0,07
500°C/12min	13,05	20,38	17,37	-10,89	2,1	13,05
550°C/12min	-17,27	-2,54	-9,83			
600°C/12min	-22,34	0,14	-12,42			
650°C/12min	-18,56	-8,26	-12,38			
700°C/12min	-26,69	-16,52	-18,72			
800°C/12min	-22,86	-15,13	-16,37			

	$\Delta\text{H-M}$	$\Delta\text{H-Rc}$	$\Delta\text{H-A}$	$\Delta\text{H-Rh}$
300°C/12min				
400°C/12min	0,1	6	7,6	1,6
450°C/12min	3,6	8,1	7,8	2
500°C/12min	6,4	6,2	10,1	6,3
550°C/12min	8,9	3,1	17,8	
600°C/12min	18,2		18,2	
650°C/12min	18,3		18	
700°C/12min	16,4		16,3	
800°C/12min	12,4		12,9	

Appendix D

Data measured for the characteristic stresses [MPa] and strain [%] from the DMA curves of the furnace annealed samples.

In the following tables, σ_{loading} , $\sigma_{\text{unloading}}$ and $\Delta\sigma$ indicate the plateau stress on loading, plateau stress on unloading and mechanical hysteresis between them. The terms $\varepsilon_{\text{start}}$, $\varepsilon_{\text{finish}}$, $\Delta\varepsilon$ and $\varepsilon_{\text{residual}}$ indicate the plateau start strain, plateau finish strain, plateau total length and residual deformation, respectively. The empty spaces denote the lack of the superelastic properties in the stress-strain curve of the corresponding sample.

- 100 μm wire

	σ_{loading}	$\sigma_{\text{unloading}}$	$\Delta\sigma$
300°C/12min			
400°C/12min	577	242	335
450°C/12min	535	198	337
500°C/12min	435	81	354
550°C/12min	457	181	276
600°C/12min	422	72	350
650°C/12min	397	88	309
700°C/12min	368	35	333
800°C/12min	466	0	466

	$\varepsilon_{\text{start}}$	$\varepsilon_{\text{finish}}$	$\Delta\varepsilon$	$\varepsilon_{\text{residual}}$
300°C/12min				0,51
400°C/12min	2,09	5,54	3,45	0,76
450°C/12min	1,49	6,07	4,58	0,52
500°C/12min	1,24	5,94	4,7	0,43
550°C/12min	0,88	7,39	6,51	0,344
600°C/12min	0,84	9,61	8,77	1,66
650°C/12min	0,64	11,07	10,43	2,18
700°C/12min	0,52	11,82	11,3	3,97
800°C/12min	0,95	14,82	13,87	13,33

- 200 μm wire

	σ_{loading}	$\sigma_{\text{unloading}}$	$\Delta\sigma$
300°C/12min			
400°C/12min	534	290	244
450°C/12min	478	220	258
500°C/12min	418	123	295
550°C/12min	415	123	292
600°C/12min	366	55	311
650°C/12min	372	76	296
700°C/12min	350	66	284
800°C/12min	441	0	441

	ϵ_{start}	ϵ_{finish}	$\Delta\epsilon$	$\epsilon_{\text{residual}}$
300°C/12min				0,12
400°C/12min	1,91	5,54	3,63	0,26
450°C/12min	1,7	6,36	4,66	0,29
500°C/12min	1,47	6,52	5,05	0,39
550°C/12min	1,03	7,23	6,2	0,46
600°C/12min	0,78	9,23	8,45	0,86
650°C/12min	0,95	10,93	9,98	1,79
700°C/12min	0,8	11,99	11,19	2,8
800°C/12min	1,14	14,52	13,38	12,85

Appendix E

Data measured for the characteristic temperatures [$^{\circ}\text{C}$] and latent heat of transformation [J/g] from the DSC curves of the laser annealed samples.

In the following tables, M_s , M_f and M_p indicate the martensite start, finish and peak temperatures; R_{cs} , R_{cf} and R_{cp} indicate the R-phase transformation start, finish and peak temperatures on cooling; A_s , A_f and A_p indicate the start, finish and peak temperatures; R_{hs} , R_{hf} and R_{hp} indicate the R-phase transformation start, finish and peak temperatures on heating. The terms $\Delta H-M$, $\Delta H-R_c$, $\Delta H-A$ and $\Delta H-R_h$ refer to the latent heat of transformation of martensite, R-phase on cooling, austenite and R-phase upon heating, respectively. The empty spaces denote the lack of the corresponding transformation peak in the calorimetric curve.

- $v=50 \text{ mm/s}$ $P=65 \text{ W}$

	M_s	M_f	M_p	R_{cs}	R_{cf}	R_{cp}
5 MPa	-89,3	-117,6	-94,4	-0,5	-57,8	-29,2
	-101,4	-130,3	-110,1	-1,7	-44,9	-21,4
	-104,4	-128,2	-115	5,3	-57,7	-25,7
50 Mpa	-99,3	-127,5	-110,4	3,9	-77,5	-26,1
	-102,4	-131,3	-115,1	0,8	-79,9	-25,4
	-102,3	-128,4	-114,3	-2,4	-83,4	-25,8
150 Mpa	-89	-119,2	-99,1	-13,4	-53,2	-26,5
	-109	-128,4	-119,9	-4,8	-58,1	-21,7
	-108,5	-127,8	-117,9	-3,5	-72	-24,8
300 Mpa	-97,1	-123,7	-107,6	-0,3	-53,1	-26,1
	-99,7	-121,5	-108,8	-6	-64,2	-26,1
	-108,6	-132,4	-123,6	0,5	-63,5	-21,9

	As	Af	Ap	Rhs	Rhf	Rhp
5 MPa	-46,7	-20,6	-32,9			
	-48,3	-22	-33,9			
	-45,5	-21	-32,6			
50 Mpa	-45,3	-21,9	-32,8			
	-45,9	-21,8	-32,8			
	-46,9	-20,9	-32,8			
150 Mpa	-44,3	-21	-32,9			
	-44,6	-21,1	-32,9			
	-44,9	-22,1	-32,9			
300 Mpa	-48,2	-21,1	-32,5			
	-44,1	-20,1	-33,5			
	-21	-44,4	-32,4			

	$\Delta H-M$	$\Delta H-Rc$	$\Delta H-A$	$\Delta H-Rh$
5 MPa	3,3	5,2		12
	4,5	2,3		8,3
	7,1	2,6		10,5
50 Mpa	4,9	2,6		7,3
	6,8	2,3		8
	6	2,4		9
150 Mpa	3,3	2,4		9,8
	4,4	1		7,1
	4,2	0,9		6,3
300 Mpa	3,4	4		9,8
	4	3,7		8,6
	6,6	0,7		8,4

- $v=50 \text{ mm/s}$ $P=75 \text{ W}$

	Ms	Mf	Mp	Rcs	Rcf	Rcp
5 MPa	-74,28	-93,91	-80,31	-19,1	-66,76	-38,03
	-72,7	-90,5	-79,7	-17,2	-65,97	-36,6
	-63,96	-85,4	-66,7	-18,2	-58,6	-36,5
50 Mpa	-59,3	-80,36	-70,2	-20,41	-56,57	-37,59
	-70,24	-89,02	-78,31	-16,71	-57,8	-34,39
	-68,92	-86,8	-75,72	-15,33	-59,02	-35,7
150 Mpa	-68,07	-95,45	-71,65	-14,75	-58,83	-34,93
	-67,18	-89,64	-79,89	-11,74	-56,26	-35,7
	-67,23	-89,48	-77,35	-13,36	-53,91	-34,02
300 Mpa	-70,6	-93,4	-82,9	-16,1	-63,7	-37,3
	-72,9	-93,6	-79,7	-18,9	-63,8	-37
	-72,1	-92,1	-79,7	-15,6	-65	-37,8

	As	Af	Ap	Rhs	Rhf	Rhp
5 MPa	-40,54	-19,6	-29,5			
	-43,5	-18,3	-29,1			
	-42,7	-18,4	-26,2			
50 Mpa	-38,4	-16,82	-26,18			
	-42,84	-19,32	-28,63			
	-41,51	-18,25	-28,15			
150 Mpa	-42,27	-17,85	-28,21			
	-41,83	-19,05	-28,02			
	-43,11	-18,42	-28,33			
300 Mpa	-41,5	-18,1	-29,4			
	-41,6	-18,8	-29,1			
	-41,5	-19	-28,6			

	$\Delta H-M$	$\Delta H-Rc$	$\Delta H-A$	$\Delta H-Rh$
5 MPa	1,7	7,6		11,3
	2,9	8,8		12,8
	1,3	10,7		13
50 Mpa	0,5	9,2		12,5
	2	7,6		12,2
	2,3	9,1		13,3
150 Mpa	2,8	8		12,9
	1,9	7,7		12,3
	1,9	8,9		13,4
300 Mpa	1,5	6,4		10
	2,5	8,5		12,9
	2,2	8,5		12,8

- $v=50$ mm/s P=85 W

	Ms	Mf	Mp	Rcs	Rcf	Rcp
5 MPa	-49,3	-69,4	-50,4			
	-50,2	-69,3	-53,8			
	-48,1	-64,5	-52,4			
50 Mpa	-46	-60,1	-49,4			
	-43,8	-62	-48,1			
	-44,5	-62,5	-48,1			
150 Mpa	-47,4	-65,8	-50,1			
	-48,5	-63,9	-50,8			
	-47,4	-64	-52,5			
300 Mpa	-44,6	-60,9	-49			
	-45,8	-58,1	-47,4			
	-48,8	-61,4	-53,9			

	As	Af	Ap	Rhs	Rhf	Rhp
5 MPa	-33,8	-15,9	-20,8			
	-34,9	-15,4	-20,6			
	-32,3	-15,02	-19,9			
50 Mpa	-31,7	-14,9	-19,1			
	-32,7	-14,2	-18,8			
	-38,7	-13,9	-19,9			
150 Mpa	-30,6	-14,8	-19,5			
	-31,4	-15,4	-19,9			
	-31,1	-15,3	-19,8			
300 Mpa	-29,9	-14,1	-18,3			
	-30	-14,9	-18,8			
	-31,8	-13,7	-20			

	$\Delta H-M$	$\Delta H-Rc$	$\Delta H-A$	$\Delta H-Rh$
5 MPa		14,9		17
		13,8		15,8
		12,3		14
50 Mpa		12,5		13,5
		14,9		14,7
		11		15,8
150 Mpa		16,3		12,5
		17,9		14,6
		14,2		13,7
300 Mpa		15,9		15,2
		18,2		16,7
		15,1		16,4

Appendix F

Data measured for the characteristic stresses [MPa] and strain [%] from the DMA curves of the laser annealed samples.

In the following tables, σ_{loading} , $\sigma_{\text{unloading}}$ and $\Delta\sigma$ indicate the plateau stress on loading, plateau stress on unloading and mechanical hysteresis between them. The terms ϵ_{start} , ϵ_{finish} , $\Delta\epsilon$ and $\epsilon_{\text{residual}}$ indicate the plateau start strain, plateau finish strain, plateau total length and residual deformation, respectively. The empty spaces denote the lack of the superelastic properties in the stress-strain curve of the corresponding sample.

- $v=50 \text{ mm/s}$ $P=65 \text{ W}$

	σ_{loading}	$\sigma_{\text{unloading}}$	$\Delta\sigma$
5 MPa	528	290	238
	527	271	256
	519	247	272
50 MPa	541	273	268
	538	314	224
	539	278	261
150 MPa	543	336	207
	542	332	210
	534	285	249
300 MPa	526	307	219
	533	305	228
	537	319	218

	ϵ_{start}	ϵ_{finish}	$\Delta\epsilon$	$\epsilon_{\text{residual}}$
5 MPa	1,3	8,1	0,8	6,8
	1,2	7,9	0,7	6,7
	1	8	0,8	7
50 MPa	1,1	7,6	0,6	6,5
	1,2	7,9	0,5	6,7
	1,1	7,6	0,6	6,5
150 MPa	1,3	7,8	0,4	6,5
	1,2	7,9	0,3	6,7
	1,1	7,7	0,6	6,6
300 MPa	1,4	8,6	0,6	7,2
	1,3	8,3	0,6	7
	1,4	8,4	0,5	7

- $v=50 \text{ mm/s}$ $P=75 \text{ W}$

	σ_{loading}	$\sigma_{\text{unloading}}$	$\Delta\sigma$
5 MPa	469	210	259
	480	231	249
	478	224	254
50 MPa	468	201	267
	471	202	269
	478	233	245
150 MPa	511	281	230
	479	224	255
	501	244	257
300 MPa	504	236	268
	492	266	226
	492	229	263

	ϵ_{start}	ϵ_{finish}	$\Delta\epsilon$	$\epsilon_{\text{residual}}$
5 MPa	1,1	8,9	1	7,8
	1,1	9	0,9	7,9
	1	9,5	0,8	8,5
50 MPa	1	9,2	0,8	8,2
	1,1	9	0,8	7,9
	1,1	9,4	0,7	8,3
150 MPa	1,1	8,5	0,9	7,4
	1,1	9,4	0,9	8,3
	1,1	8,5	0,9	7,4
300 MPa	1,1	8,6	0,8	7,5
	1,5	9	0,7	7,5
	1,3	8,7	1	7,4

- $v=50 \text{ mm/s}$ $P=85 \text{ W}$

	σ_{loading}	$\sigma_{\text{unloading}}$	$\Delta\sigma$
5 MPa	453	167	286
	457	176	281
	440	137	303
50 MPa	441	129	312
	440	119	321
	436	120	316
150 MPa	441	144	297
	441	147	294
	442	141	301
300 MPa	446	158	288
	451	143	308
	447	150	297

	ϵ_{start}	ϵ_{finish}	$\Delta\epsilon$	$\epsilon_{\text{residual}}$
5 MPa	0,9	9,5	1,2	8,6
	1,0	9,7	1,1	8,7
	1,0	10	1,4	9,0
50 MPa	0,9	10	1,4	9,1
	0,9	10	1,6	9,1
	0,9	10	1,5	9,1
150 MPa	0,9	9,9	1,2	9,0
	0,9	10	1,2	9,1
	0,9	10	1,3	9,1
300 MPa	0,9	9,9	1,2	9,0
	0,9	9,7	1,2	8,8
	1,0	10	1,3	9,0